NASA Contractor Report 3560

A FORTRAN Program for Calculating Three-Dimensional, Inviscid, Rotational Flows With Shock Waves in Axial Compressor Blade Rows

User's Manual

William T. Thompkins, Jr.

GRANT NSG-3234
JUNE 1982

NASA

NASA Contractor Report 3560

A FORTRAN Program for Calculating Three-Dimensional, Inviscid, Rotational Flows With Shock Waves in Axial Compressor Blade Rows

User's Manual

William T. Thompkins, Jr.
Massachusetts Institute of Technology
Cambridge, Massachusetts

Prepared for
Lewis Research Center
under Grant NSG-3234

NASA
National Aeronautics
and Space Administration

Scientific and Technical
Information Office

1982

TABLE OF CONTENTS

SYMBOL TABLE

UPPER CASE

A_R, A_Θ	Coefficient matrices in L_R and L_Θ finite difference operators
C_1	Placement constant for part-span shroud
C_2	Relaxation factor on radial grid lines
D	Differential operator
E_t	Total internal energy
F,G,G^*,H	Flux vectors in radial, tangential and axial direction
J	Jacobian
J^+	Downstream running characteristic value
J^-	Upstream running characteristic value
K	Right-hand side of conservation law equations due to cylindrical coordinates
K_x	Axial grid stretching factor
L	Reference length
L_R,L_X,L_Θ	Finite difference operators in radial, axial and tangential directions
M	Mach number
R	Transformed radial direction
R_1	Radius of part-span shroud lower surface
R_2	Radius of part-span shroud upper surface
$\tilde{R}$	Working fluid gas constant
R_s, R_T	Surface radius of curvature
T	Temperature
U	Solution state vector
U_R,U_X,U_Θ	Contra-variant velocities normal to radial, axial and tangential planes

$\overrightarrow{V}$	Velocity vector
$\overrightarrow{V}_m$	Meridional velocity vector
X	Transformed axial coordinate
Z	Finite difference damping operator

LOWER CASE

a	Speed of sound
a_o	Reference velocity
a_{up}	Far upstream speed of sound
c_p	Specific heat at constant pressure
c_v	Specific heat at constant volume
e	Internal energy
f	General fluid property
h	Enthalpy
h_m, h_n, h_θ	Coordinate arc length scale factor in meridional, normal directions
$\hat{i}_r$	Unit vector in radial direction
$\hat{i}_\theta$	Unit vector in tangential direction
j,k,ℓ,n	Finite difference grid numbers in axial, tangential, radial and time direction
m	Finite difference operation repeat factor
$\bar{n}$	Unit normal vector
p	Static pressure or finite difference operation time step factor
r,θ,z	Cylindrical coordinate system directions
r_{tip}	Tip casing radius

s	Entropy
t	Time
u,v	General cartesian velocities
u_m, u_n	Meridional, normal velocity
u_r, u_θ, u_z	Radial, tangential, axial velocities
u_s	Parallel velocity

GREEK

γ	Ratio of specific heats
$\gamma_r, \gamma_\theta, \gamma_z$	Direction cosine of surface normal vectors
δt	Time step increment value
$\delta t_R, \delta t_X, \delta t_\Theta$	Maximum time step value in transformed radial axial and tangential directions
$\delta n, \delta x, \delta y$	Spatial step increment in normal or cartesian directions
θ	Cylindrical coordinate system tangential direction
Θ	Transformed θ coordinate
ξ	First transformed axial direction
κ	Artificial damping constant
ρ	Fluid density
ρ_o	Reference fluid density
ω	Blade row angular rotation speed

SUBSCRIPTS

h	Hub
ℓe	Leading edge
lower	Damper lower surface
m	Meridional direction
o	Reference conditions
ps	Pressure surface
ss	Suction surface
T	Stagnation condition
tip	Tip radius
te	Trailing edge
upper	Damper upper surface
w	Wall value

A FORTRAN PROGRAM FOR CALCULATING THREE-DIMENSIONAL, INVISCID, ROTATIONAL FLOWS WITH SHOCK WAVES IN AXIAL COMPRESSOR BLADE ROWS - USER'S MANUAL

by

William T. Thompkins, Jr.

Gas Turbine and Plasma Dynamics Laboratory
Department of Aeronautics and Astronautics
Massachusetts Institute of Technology
Cambridge, Massachusetts

SUMMARY

A FORTRAN-IV computer program has been developed for the calculation of the inviscid transonic/supersonic flow field in a fully three-dimensional blade passage of an axial compressor rotor or stator. Rotors may have dampers (part-span shrouds). MacCormack's explicit time-marching method is used to solve the unsteady Euler equations on a finite difference mesh. This technique captures shocks and smears them over several grid points. Input quantities are blade row geometry, operating conditions and thermodynamic quantities. Output quantities are three velocity components, density and internal energy at each mesh point. Other flow quantities are calculated from these variables. A short graphics package is included with the code, and may be used to display the finite difference grid, blade geometry and static pressure contour plots on blade-to-blade calculation surfaces or blade suction and pressure surfaces.

Flows in four transonic compressor rotors have been analyzed and compared with exit flow field measurements and intra-blade static density

measurements obtained with a gas fluorescence technique. These comparisons have generally shown that the computed flow fields accurately model the experimentally determined passage shock positions and overall aerodynamic performance.

The computer code was developed and generally run on a large minicomputer system, a Digital Equipment Corporation PDP-11/70, with run times of two to three days. The code has also been run on several main-frame computers (IBM 3033, IBM 360/678, UNIVAC 1110, CDC 7600 and a CRAY-1). Typical run times on an IBM 3033 have been found to be 5-10 hours.

INTRODUCTION

For many analysis problems in turbomachinery, an assumption of inviscid flow provides sufficiently accurate results for design or development tasks. This situation often arises in calculation of design point performances for high speed axial compressor blade rows, even though these flows may exhibit complex interactions of inviscid and viscous phenomena. An accurate inviscid calculation is of great benefit for compressor design since viscous and shock losses can both be reduced if the inviscid flow can be predicted. The design point performance of high speed axial compressors could be greatly improved through the use of an accurate inviscid flow solution, without requiring a fully viscous flow solution.

Classical analytical solutions for these flows have not developed either because of the flow character--mixed subsonic-supersonic flow with strong shock waves--or because of the intrinsic nonlinear, three-dimensional features of transonic flows. For such flows pure numerical procedures can usually provide quick, accurate solutions with reasonable cost. The numerical procedures and techniques to be described have been specialized for solutions of inviscid flow in high pressure ratio, high tip-speed axial compressor rotors, even though the techniques employed are of much wider generality.

The compressor rotors to be studied are assumed to be isolated blade rows which are completely enclosed by hub and tip casings. Since the fluid is assumed to be inviscid and each blade in a row is assumed to be identical, the flow field about each blade may reasonably be considered to be identical. This assumption allows the physical domain of interest to be reduced to that bounded by a pair of blades and the extension of their mean camber lines upstream and downstream, as illustrated in Figure 1. This region is assumed to extend to upstream and downstream infinity, and the flow is assumed to be periodic blade-to-blade. The blade rows of interest have several common features: their internal flows have mixed subsonic-transonic-supersonic relative Mach numbers, a range of 0.5 to as high as 2.0, and they attempt to use moderately strong shock waves as an efficient method to transfer energy from the rotating machinery to the fluid flow; their internal flow passages are complex three-dimensional shapes in which natural bounding surfaces rarely join orthogonally. These characteristics rather severely restrict the present choice of numerical solution schemes to time-accurate, finite difference solutions of the three-dimensional Euler Equations (continuity, inviscid momentum and inviscid energy equation with no heat conduction).

The numerical scheme selected to integrate the equations of motion is MacCormack's method.[1,2] This scheme is an explicit, time-accurate, conditionally stable method of second order accuracy with good shock capturing properties. Shock waves are resolved as regions of high gradients spread over about 5 mesh points in the streamwise direction. In a complex flow the existence and location of shock waves need not be anticipated but develop naturally as the solution proceeds. The penalty paid for this convenience is a loss in spatial resolution of shock waves and some inaccuracy in shock jump conditions. Although shock-fitting schemes are an area of current research,[3,4] methods suitable for three-dimensional flows are not yet available.

In most situations, the time accurate nature of MacCormack's method is of little importance since only the steady state solution is of interest. Here the integration method is only a convenient iteration scheme to move from a rather arbitrary initial condition to the final steady state solution. Commonly used initial conditions are an old steady state solution or a quasi-meridional start-up procedure provided with the code.

Finite difference methods are useful for complex equation sets such as the Euler or Navier-Stokes equations, but can be effectively used only in simple geometric regions. Using finite difference methods for complex geometries requires adopting coordinate systems or coordinate mappings which transform the physical domain into a computational domain of simple shape. In this report, a set of simple analytical stretching functions is used to map the bounding surfaces into a square computational domain. These transforms accommodate any hub or tip casing shape and almost any blade shape. Best results are obtained for thin leading and trailing edges as are most often encountered in compressor blade rows. Further work is continuing on more general coordinate mappings to provide more accurate solutions for any blade geometry.

The computer codes described in this report represent a radical departure in philosophy of large-scale computational projects in the choice of computer systems. These codes were developed and production runs made on a dedicated minicomputer, a Digital Equipment Corporation PDP-11/70, rather than a large main frame computer. These codes have also been run on an IBM 360/67, an IBM 3033, a UNIVAC 1110, a CDC 7600, and a CRAY-1. It was found during development that, at least in the author's opinion, the dedicated minicomputer was a superior code development machine to any main frame computer. The cost of production code running was also lower than on any available main frame computer, with a total cost of about 300 dollars per solution.

METHOD OF ANALYSIS

Flow Equations

For flow calculations in turbomachinery blade passages, a cylindrical coordinate system is a natural choice since considerable cylindrical symmetry exists, and was selected as a base coordinate system. This system is a right-handed one (r, θ, z) which has the positive z coordinate pointing in the axial flow direction. Blade rows will be assumed to rotate in the positive θ direction, clockwise when looking downstream.

A convenient set of three-dimensional inviscid flow equations expressed in cylindrical coordinates is found in MacCormack.[1] These equations are in weak conservation law form and may be easily expressed in matrix form as:

$$\frac{\partial U}{\partial t} + \frac{\partial F}{\partial r} + \frac{\partial G^*}{\partial \theta} + \frac{\partial H}{\partial z} = K \qquad (1)$$

where

$$U = \begin{bmatrix} r\rho \\ r\rho u_r \\ r\rho u_\theta \\ r\rho u_z \\ rE_t \end{bmatrix} \qquad F = \begin{bmatrix} r\rho u_r \\ r(\rho u_r^2+P) \\ r\rho u_\theta u_r \\ r\rho u_r u_z \\ ru_r(E_t+P) \end{bmatrix}$$

$$G^* = \begin{bmatrix} \rho u_\theta \\ \rho u_r u_\theta \\ \rho u_\theta^2 + P \\ \rho u_z u_\theta \\ u_\theta (E_t + P) \end{bmatrix} \quad H = \begin{bmatrix} r\rho u_z \\ r\rho u_r u_z \\ r\rho u_\theta u_z \\ r(\rho u_z^2 + P) \\ r u_z (E_t + P) \end{bmatrix} \quad K = \begin{bmatrix} 0 \\ \rho u_\theta^2 + P \\ -\rho u_\theta u_r \\ 0 \\ 0 \end{bmatrix}$$

$E_t = \rho(e + u^2/2)$, and $u^2 = u_r^2 + u_\theta^2 + u_z^2$. In addition the working fluid will be assumed to be a perfect gas with constant thermodynamic properties, γ, $\tilde{R}$, C_p and C_v. The equation of state may be written as

$$p = \rho e(\gamma - 1) \tag{2}$$

In order to apply the boundary condition of no flow through the blade surface at a constant spatial location a common independent variable transformation is introduced.

$$\theta' = \theta - \omega t \tag{3}$$

The new independent variable is θ', and ω is the rotational speed of the blade row. Using this transform the flow equations become:

$$\frac{\partial U}{\partial t'} - \omega \frac{\partial U}{\partial \theta'} + \frac{\partial F}{\partial r'} + \frac{\partial G^*}{\partial \theta'} + \frac{\partial H}{\partial z'} = K \tag{4}$$

or

$$\frac{\partial U}{\partial t} + \frac{\partial F}{\partial r} + \frac{\partial G}{\partial \theta} + \frac{\partial H}{\partial z} = K \tag{5}$$

where $G = G^* - \omega U = \begin{bmatrix} \rho u_\theta - \omega r \rho \\ \rho u_r u_\theta - \omega r \rho u_r \\ \rho u_\theta^2 + P - \omega r \rho u_\theta \\ \rho u_z u_\theta - \omega r \rho u_z \\ u_\theta (E_t + P) - \omega r E_t \end{bmatrix}$

and the prime superscripts have been dropped for convenience.

These equations are non-dimensionalized using a reference length, L, a reference velocity, a_0, and a reference density, ρ_0. The reference quantities are in principle arbitrary, but the reference velocity and density have been selected to be the stagnation speed of sound and density on the inlet tip casing streamline. The reference length remains arbitrary but is conventionally selected as the inlet tip casing radius. The new non-dimensional variables (primes indicate dimensionless quantities) are:

length $r' = r/L$, $z' = z/L$ (6)

velocity $u' = u/a_0$ (7)

density $\rho' = \rho/\rho_0$ (8)

pressure $p' = p/\rho_0 a_0^2$ (9)

energy $e' = e/a_0^2$ (10)

rotational speed $\omega' = \omega L/a_0$ (11)

The reference quantities T_0 and p_0 are not independent and are determined from:

$$T_0 = a_0^2/\ \gamma R \tag{12}$$

$$P_0 = 1/\gamma \tag{13}$$

When these quantities are selected, the flow equations in terms of nondimensional variables are identical in form to those in terms of dimensional variables, equation (5). The prime superscripts may then be dropped without confusion and only nondimensional quantities will be referred to in the remaining sections of this report. The Euler flow equations become

$$\frac{\partial U'}{\partial t'} + \frac{\partial F'}{\partial r'} + \frac{\partial G'}{\partial \theta} + \frac{\partial H'}{\partial z'} = K \tag{14}$$

$$U' = \begin{bmatrix} r'\rho' \\ r'\rho'u_r' \\ r'\rho'u_\theta \\ r'\rho'u_z' \\ r'E_t \end{bmatrix} \qquad F' = \begin{bmatrix} r'\rho'u_r' \\ r'(\rho'u_r'^2 + P') \\ r'\rho'u_\theta'u_r' \\ r'\rho'u_r'u_z' \\ r'u_r'(E_t'+P) \end{bmatrix}$$

$$G' = \begin{bmatrix} \rho'u_\theta' - \omega'r'\rho' \\ \rho'u_r'u_\theta' - \omega r'\rho'u_r' \\ \rho'u'{}_\theta^2 + P - \omega'r'\rho'u_\theta' \\ \rho'u_z u_\theta' - \omega'r'\rho'u_z' \\ u_\theta'(E_t'+P) - \omega'r'E_t' \end{bmatrix} \quad H = \begin{bmatrix} r'\rho'u_z' \\ r'\rho'u_r'u_z' \\ r'\rho'u_\theta'u_z' \\ r(\rho'u_z'^2+P) \\ r'u_z'(E_t+P') \end{bmatrix} \quad K = \begin{bmatrix} 0 \\ \rho'u_\theta'^2+P' \\ -\rho'u_\theta'u_r' \\ 0 \\ 0 \end{bmatrix}$$

Transformed Equations

As is typical in three-dimensional flow solutions, the geometric domain in physical space is sufficiently complex to render a direct finite difference solution in physical space impractical. The approach adopted here to solve the finite difference grid allocation problem is to introduce a set of independent variable transformations or coordinate stretchings which map a single compressor blade passage into a rectangular parallelepiped. A generalized mapping is indicated by

$$(r,\ \theta,\ z) \rightarrow (R,\ \Theta,\ X) \tag{15}$$

with

$$R = R(r,\ \theta,\ z), \quad \Theta = \Theta(r,\ \theta,\ z), \text{ and } \quad X = X(r,\ \theta,\ z)\ .$$

Introducing a coordinate transform modifies the original partial differential equations. Using the chain rule for derivatives Equation (14) becomes

$$\begin{aligned} &\frac{\partial U}{\partial t} + \frac{\partial F}{\partial R}\frac{\partial R}{\partial r} + \frac{\partial F}{\partial \Theta}\frac{\partial \Theta}{\partial r} + \frac{\partial F}{\partial X}\frac{\partial X}{\partial z} + \frac{\partial G}{\partial R}\frac{\partial R}{\partial \Theta} + \frac{\partial G}{\partial \Theta}\frac{\partial \Theta}{\partial \theta} + \frac{\partial G}{\partial X}\frac{\partial X}{\partial \theta} \\ &\quad + \frac{\partial H}{\partial R}\frac{\partial R}{\partial z} + \frac{\partial H}{\partial \Theta}\frac{\partial \Theta}{\partial z} + \frac{\partial H}{\partial X}\frac{\partial X}{\partial z} = K \end{aligned} \tag{16}$$

This equation may be rearranged as:

$$\frac{\partial U}{\partial t} + \left[\frac{\partial F}{\partial R}\frac{\partial R}{\partial r} + \frac{\partial G}{\partial R}\frac{\partial R}{\partial \theta} + \frac{\partial H}{\partial R}\frac{\partial R}{\partial z}\right] + \left[\frac{\partial F}{\partial \Theta}\frac{\partial \Theta}{\partial r} + \frac{\partial G}{\partial \Theta}\frac{\partial \Theta}{\partial \theta} + \frac{\partial H}{\partial \Theta}\frac{\partial \Theta}{\partial z}\right]$$

$$+ \left[\frac{\partial F}{\partial X}\frac{\partial X}{\partial r} + \frac{\partial G}{\partial X}\frac{\partial X}{\partial \theta} + \frac{\partial H}{\partial X}\frac{\partial X}{\partial z}\right] = K \qquad (17)$$

Equation (14) is in weak conservation law form, while equation (17) is in non-conservation law form after the coordinate transforms have been introduced. The weak conservation law form may be retained, reference 5 and 6, as:

$$\frac{\partial \overline{U}}{\partial t} + \frac{\partial \overline{F}}{\partial R} + \frac{\partial \overline{G}}{\partial \Theta} + \frac{\partial \overline{H}}{\partial X} = \overline{K} \qquad (18)$$

where

$$\overline{U} = U/J; \ \overline{F} = \left[F\frac{\partial R}{\partial r} + \frac{G}{r}\frac{\partial R}{\partial \theta} + H\frac{\partial R}{\partial z}\right] \Big/ J , \qquad (19)$$

$$\overline{G} = \left[F\frac{\partial \Theta}{\partial r} + \frac{G}{r}\frac{\partial \Theta}{\partial \theta} + H\frac{\partial \Theta}{\partial z}\right] \Big/ J , \qquad (20)$$

$$\overline{H} = \left[F\frac{\partial X}{\partial r} + \frac{G}{r}\frac{\partial R}{\partial \theta} + H\frac{\partial X}{\partial z}\right] \Big/ J \qquad (21)$$

$$\overline{K} = K/J \qquad (22)$$

J is the transform Jacobian.

$$J = \det \begin{pmatrix} \frac{\partial R}{\partial r} & \frac{\partial R}{\partial \theta} & \frac{\partial R}{\partial z} \\ \frac{\partial \Theta}{\partial r} & \frac{\partial \Theta}{\partial \theta} & \frac{\partial \Theta}{\partial z} \\ \frac{\partial X}{\partial r} & \frac{\partial X}{\partial \theta} & \frac{\partial X}{\partial z} \end{pmatrix} \tag{23}$$

These equations may be rewritten in the following form in which the contravariant velocity components appear directly.

$$\overline{F} = \frac{1}{J} \begin{pmatrix} r \rho U_R \\ r\rho u_r U_R + rP(\partial R/\partial r) \\ r \rho u_\theta U_R \\ r \rho u_z U_R + rP(\partial R/\partial X) \\ r \rho U_R(E + P/\rho) \end{pmatrix} \tag{24}$$

$$\overline{H} = \frac{1}{J} \begin{pmatrix} r \rho U_X \\ r \rho u_r U_X + rP(\partial X/\partial r) \\ r \rho u_\theta U_X \\ r \rho u_z U_X + rP(\partial X/\partial z) \\ r \rho U_X(E + P/\rho) \end{pmatrix} \tag{25}$$

$$\overline{G} = \frac{1}{J} \begin{pmatrix} r \rho U_\Theta \\ r \rho u_r U_\Theta + rP(\partial \Theta/\partial r) \\ r \rho u_\theta U_\Theta + rP[(\partial \Theta/\partial \theta)/r] \\ r \rho u_z U_\Theta + rP(\partial \Theta/\partial z) \\ r \rho U_\Theta(E + P/\rho) + (\omega r)(rP)[(\partial \Theta/\partial \theta)/r] \end{pmatrix} \tag{26}$$

where

$$U_R = u_r \left[\frac{\partial R}{\partial r}\right] + \frac{u_\theta}{r} \frac{\partial R}{\partial \theta} + u_z \left[\frac{\partial R}{\partial z}\right] \tag{27}$$

$$U_X = u_r \left[\frac{\partial X}{\partial r}\right] + \frac{u_\theta}{r} \frac{\partial X}{\partial \theta} + u_z \left[\frac{\partial X}{\partial z}\right] \tag{28}$$

$$U_\Theta = u_r \left[\frac{\partial \Theta}{\partial r}\right] + \frac{(u_\theta - \omega r)}{r} \frac{\partial \Theta}{\partial \theta} + u_z \left[\frac{\partial \Theta}{\partial z}\right] \tag{29}$$

As described in reference 6, U_R, U_θ and U_X are the contravariant velocities perpendicular to the R, Θ and X coordinate surfaces. If these coordinate surfaces are chosen to coincide with physical boundaries in the problem, the no flow through solid surface boundary condition becomes:

$U_R = 0$ on constant R surfaces (30)

$U_\Theta = 0$ on constant Θ surfaces (31)

$U_X = 0$ on constant X surfaces (32)

Full conservation law forms (CLF) are generally to be preferred over non-conservation law forms (NCLF) on a theoretical basis. CLF contain the correct shock jump conditions while NCLF may not. The CLF, when used with appropriate spatial differencing, should have superior mass, energy and momentum conservation properties. When a CLF finite difference solution is summed over a large volume of several mesh cells, the inter-cell flux of energy mass, and momentum cancel, thus satisfying the integral conservation law properties for the large volume. For flow regions without shock waves, CLF solutions and NCLF solutions approach each other as the grid spacing decreases, but incorrect shock jump conditions may be predicted by NCLF solutions even in the limit of infinite grid resolution.

For simple flow problems where shock waves may be aligned with cell boundaries, the theoretical advantages of the CLF are easily demonstrated. For practical flow problems where shock waves may cross cell boundaries, the CLF advantages are more difficult to demonstrate. In fact, NCLF solutions often appear to give superior results. For this reason, the computer code described in this report has the capability to use either the NCLF of equation (17) or the weak conservation law form of equation (18).

Coordinate Transforms for Compressor Blade Rows

As was previously discussed, the analysis will be limited to calculations for the flow through a single blade passage. The physical flow domain is illustrated in Figure 1 and consists of the space bounded by a pair of blades and the extension of their mean camber lines upstream and downstream of the blade row. The extension region is assumed to extend to upstream and downstream infinity, and the flow is assumed to be periodic, blade-to-blade, in this region. This physical domain is mapped onto a computational domain which is a rectangular parallelopiped. The computational domain is usually truncated 3 to 5 chords upstream and downstream of the blade row.

Domain Regularizing Functions

Two mapping functions were chosen: first, one which regularizes the physical domain; and second, one which locally increases mesh density near the blade leading and trailing edges. The domain regularizing functions are given by:

$$R = \frac{r - r_{hub}(z)}{r_{tip}(z) - r_{hub}(z)} \tag{33}$$

$$\Theta = \frac{\theta - \theta_{ps}(r,z)}{\theta_{ss}(r,z) - \theta_{ps}(r,z)} \tag{34}$$

and

$$\xi = \left(\frac{z - z_{\ell e}(r)}{z_{te}(r) - z_{\ell e}(r)}\right) - 0.5 \tag{35}$$

Here r_{hub} is the radial position of the hub casing

r_{tip} is the radial position of the tip casing

θ_{ps} is the theta position of the blade pressure surface

θ_{ss} is the theta position of the blade suction surface

$z_{\ell e}$ is the plan view projection of the blade row leading edge

z_{te} is the plan view projection of the blade row trailing edge

A plan view for a typical compressor blade row in both physical space and computational space is shown in Figure 2. The hub and tip casings and the blade leading and trailing edge lines are mapped to straight lines. These mappings are adequate for nearly any compressor flow path.

Similar views of the physical and computational space for blade to blade sections are shown in Figure 3. Here the curved blade shapes are mapped to untwisted planes. This mapping appears adequate for thin compressor blades but may not be adequate for thick blades with blunt trailing edges, as might be encountered in turbine blade rows.

The effect of an axisymmetric part-span vibration damper or shroud can be included by modifying only the coordinate stretching in the r direction, Equation (33). A plan view of a typical flow path which includes a part-span shroud is shown in Figure 4. This geometry can be treated by defining two mapping functions; one function for the physical space below the damper ($r < r_{lower}$), and a second function for the physical space above the damper ($r > r_{upper}$).

$$R_1 = C_1 \left[\frac{r - r_{hub}}{r_{lower} - r_{hub}} \right] \qquad \text{for } r \leq r_{lower} \tag{36}$$

$$R_2 = (1-C_1) \left[\frac{r - r_{upper}}{r_{tip} - r_{upper}} \right] + C_1 \qquad \text{for } r \geq r_{upper}$$

Here, r_{upper} is a function of (r,z) specifying geometry of upper surface of damper, r_{lower} is a function of (r,z) specifying geometry of lower surface of damper, and C_1 is a constant determining placement of damper in computational space. The best value of C_1 is dependent on boundary condition formulations and will be discussed in a later section. This transform maps the damper into a slit in R-ξ computational space as shown in Figure 5.

If the blade leading and trailing edges are not constant z lines then near the upstream and downstream edges of the computational domain, the grid lines produced by these mappings are skewed with respect to either the local streamlines or a constant z line. This skewness may be eliminated by using the following transform, applied outside the blade row only, which allows a constant ξ line to approach a constant z line as $z \to \pm\infty$.

$$\xi = \left[\frac{(z - z_{\ell e_0}) + \left[z_{\ell e_0} - z_{\ell e} \right] e^{C_2 z*}}{(z_{te_0} - z_{\ell e_0}) + [(z_{te} - z_{te_0}) + (z_{\ell e_0} - z_{\ell e})]e^{C_2 z}} \right] - 0.5 \tag{38}$$

where $z_{\ell e_0}$ and z_{te_0} are the axial locations of the blade leading and trailing edge at the hub radius

C_2 is a relaxation factor typically equal to 3.0

$z^* = z - z_{\ell e}$ upstream of the blade row, and

$z^* = z_{te} - z$ downstream of the blade row.

Mesh Packing Function

A grid distributed uniformly in the (R,Θ,ξ) space may be computationally inefficient since a fine mesh is often desired near the blade leading and trailing edges and a coarse mesh is desired near the upstream and downstream boundaries. A mesh packing function which satisfies both of the requirements is:

$$\xi = A_x \sinh (K_x X) + B_x \tan^{-1}[\sinh (K_x X)] \tag{39}$$

where

$$A_x = A_x^* / \left[2 \left(A_x^* \sinh (K_x) + B_x^* \tan^{-1} \left\{ \sinh (K_x) \right\} \right) \right]$$

$$A_x^* = \operatorname{sech} (K_x)/2K_x$$

$$B_x^* = \sinh (K_x) \tanh (K_x)/2K_x$$

$$B_x = B_x^* / \left[2 \left(A_x^* \sinh (K_x) + B_x^* \tan^{-1} \left(\sinh (K_x) \right) \right) \right]$$

and K_x is a free parameter which controls the mesh packing. Details on this transform are given by Merrington[7].

This transformation from (R,Θ,ξ) space to (R,Θ,X) symmetrically packs points near the leading and trailing edges and stretches the domain away from the blade row. A typical grid structure having uniform distribution in the (R,Θ,X) space is shown in the physical space in Figure 6 (plan view) and Figure 7 (blade-to-blade view). As shown in these two figures, the grid system adopted is an offset one in which boundaries are located midway between grid lines. This arrangement has certain advantages in implementing both hard wall and periodic boundary conditions. These advantages will be discussed in a later section. These two figures also show that the blade-to-blade grid planes, R-ξ or R-X planes, are not curved in the theta direction which means that the blade-to-blade lines are not normal to blade surfaces. In addition, $\partial R/\partial \theta$ and $\partial X/\partial \theta$ are zero as may be seen from Equations (33) and (35).

Numerical Integration Scheme

Equation (17) or (18) is solved using MacCormack's[2] split operator finite difference scheme. This is a two step, explicit, second order accurate, conditionally stable scheme. The difference equations for the non-conservation law forms are:

R-direction

$$U^*_{j,k,\ell} = U^n_{j,k,\ell} - \frac{\delta t}{\delta R}\left[\left(F^n_{j,k,\ell+1} - F^n_{j,k,\ell}\right)\frac{\partial R}{\partial r} + \left(H^n_{j,k,\ell+1} - H^n_{j,k,\ell}\right)\frac{\partial R}{\partial z}\right] + \delta t\, A_R K^n_{j,k,\ell} \qquad (40)$$

$$U^{n+1}_{j,k,\ell} = \frac{1}{2}\left\{U^n_{j,k,\ell} + U^*_{j,k,\ell} - \frac{\delta t}{\delta R}\left[\left(F^*_{j,k,\ell} - F^*_{j,k,\ell-1}\right)\frac{\partial R}{\partial r} + \left(H^*_{j,k,\ell} - H^*_{j,k,\ell-1}\right)\frac{\partial R}{\partial z}\right] + \delta t\, A_R K^*_{j,k,\ell} + Z^n_{j,k,\ell}\right\} \qquad (41)$$

Θ-direction

$$\begin{aligned} U^{n} = U^{n}_{j,k,\ell} - \frac{\delta t}{\delta \Theta} \Bigg[& \left(F^{n}_{j,k+1,\ell} - F^{n}_{j,k,\ell}\right) \frac{\partial \Theta}{\partial r} \\ & + \left(G^{n}_{j,k+1,\ell} - G^{n}_{j,k,\ell}\right) \frac{\partial \Theta}{\partial \theta} + \left(H^{n}_{j,k+1,\ell} - H^{n}_{j,k,\ell}\right) \frac{\partial \Theta}{\partial z} \Bigg] \qquad (42) \\ & + \delta t \; A_{\Theta} \; K^{n}_{j,k,\ell} \end{aligned}$$

$$\begin{aligned} U^{n+1} = \frac{1}{2} \Bigg\{ & U^{*}_{j,k,\ell} + U^{n}_{j,k,\ell} - \frac{\delta t}{\delta \Theta} \Bigg[\left(F^{*}_{j,k,\ell} - F^{*}_{j,k-1,\ell}\right) \frac{\partial \Theta}{\partial r} + \\ & + \left(G^{*}_{j,k,\ell} - G^{*}_{j,k-1,\ell}\right) \frac{\partial \Theta}{\partial \theta} + \left(H^{*}_{j,k,\ell} - H^{*}_{j,k-1,\ell}\right) \frac{\partial \Theta}{\partial z} \Bigg] \qquad (43) \\ & + \delta t \; A_{\Theta} \; K^{*}_{j,k,\ell} + Z^{n}_{j,k,\ell} \Bigg\} \end{aligned}$$

X-direction

$$U^{*} = U^{n} - \frac{\delta t}{\delta X} \left[\left(F^{n}_{j+1,k,\ell} - F^{n}_{j,k,\ell}\right) \frac{\partial X}{\partial r} + \left(H^{n}_{j+1,k,\ell} - H^{n}_{j,k,\ell}\right) \frac{\partial X}{\partial z} \right] \qquad (44)$$

$$U^{n+1} = \frac{1}{2} \left\{ U^{n} + U^{*} - \frac{\delta t}{\partial X} \left[\left(F^{*}_{j,k,\ell} - F^{*}_{j-1,k,\ell}\right) \frac{\partial X}{\partial r} + \left(H^{*}_{j,k,\ell} - H^{*}_{j-1,k,\ell}\right) \frac{\partial X}{\partial z} \right] \right\} \qquad (45)$$

where j, k, and ℓ respectively identify the axial, circumferential and radial coordinate of a grid point, n indicates the time step, and * indicates an intermediate time step. Also

$$F^* = F(U^*) \tag{46}$$

$$H^* = H(U^*) \tag{47}$$

$$K^* = K(U^*) \tag{48}$$

$$A_R = [0\ 1\ 0\ 0\ 0] \tag{49}$$

$$A_\Theta = [0\ 0\ 1\ 0\ 0] \tag{50}$$

Equations (40, 42 and 44) are the predictor steps, and equations (41, 43 and 45) are the corrector steps. The forward and backward space differences appearing in the predictor and corrector steps are permuted each operator execution as suggested by MacCormack.[2] Similar operators are used for the conservation law forms.

For this type of time splitting, the three MacCormack operators must be combined in symmetric sequences in order to maintain second order accuracy.[2,8] Denoting equations (41 and 42) as the $L_R(\delta t)$ operator, equations (43 and 44) as the $L_\Theta(\delta t)$ operator and equations (45 and 46) as the $L_X(\delta t)$ operator, a sequence may be written as:

$$U^{n+2} = [L_X(\delta t)\ L_\Theta(\delta t)\ L_R(2\delta t)\ L_\Theta(\delta t)\ L_X(\delta t)]\ U^n \tag{51}$$

This simple but non-unique sequence advances the solution from time level $n\delta t$ to time level $(n+2)\delta t$.

In order to stabilize the solution along steep gradients of the flow quantities, such as across shock waves and near the leading and trailing edges, artificial viscosity terms were introduced, that add to the numerical damping of the scheme. The Lapidus[9] form of these terms was used and for L_R operator they are:

$$Z^n_{j,k,\ell} = \kappa \left\{ \left| u^n_{r_{j,k,\ell}} - u^n_{r_{j,k,\ell-1}} \right| \left(U^n_{j,k,\ell+1} - U^n_{j,k,\ell} \right) - \left| u^n_{r_{j,k,\ell+1}} - u^n_{r_{j,k,\ell}} \right| \left(U^n_{j,k,\ell} - U^n_{j,k,\ell-1} \right) \right\} \tag{52}$$

where κ is a parameter of order 1 that controls the strength of the artificial viscosity terms. Low values of κ produce sharp shocks, but result in unacceptable oscillations downstream of the shock. High values of κ yield smooth solutions, but also very wide shocks and strong distortions to the inviscid field. A typical value of κ is 0.4.

Each one-dimensional operator is explicit and in the absence of artificial damping ($Z^n_{j,k,\ell}=0$) have the stability conditions:

for L_X

$$\delta t_X \le \delta X \Big/ \left\{ \left[M_Z \left(\frac{\partial X}{\partial Z}\right) + M_r \left(\frac{\partial X}{\partial r}\right) \right] + \left(\left[\frac{\partial X}{\partial z}\right] + \left[\frac{\partial X}{\partial r}\right] \right) \right\} \tag{53}$$

for L_R

$$\delta t_R = \delta R \Big/ \left\{ \left[M_r \left(\frac{\partial R}{\partial r}\right) + M_Z \left(\frac{\partial R}{\partial Z}\right) \right] + \left(\left[\frac{\partial R}{\partial r}\right] + \left[\frac{\partial R}{\partial z}\right] \right) \right\} \tag{54}$$

for L_Θ

$$\delta t_\Theta = \delta \Theta \Big/ \left\{ \left[M_r \left(\frac{\partial \Theta}{\partial r}\right) + M_\Theta \left(\frac{\partial \Theta}{\partial \theta}\right) \right] + M_Z \left(\frac{\partial \Theta}{\partial Z}\right) + \left(\left[\frac{\partial \Theta}{\partial r}\right] + \left[\frac{\partial \Theta}{\partial \theta}\right] \Big/ r + \left[\frac{\partial \Theta}{\partial z}\right] \right) \right\} \tag{55}$$

For calculations with strong shocks, these maximum time steps must be reduced by up to 40 per cent to maintain stability.

For a given calculation δt_X, δt_R and δt_Θ may differ by over an order of magnitude, and the optimum value of δt is selected using the principle that the δt used with each operator be as close as possible to its maximum allowed value while maintaining a symmetric sequence. Typical values for transonic compressor blade rows are:

$$\delta t_R = 10\ \delta t_\Theta = 20\ \delta t_X \tag{56}$$

A suitable, symmetric sequence in this case would be

$$U^{n+20}_{j,k,\ell} = [(L_X(\delta t))^{10}\ (L_\Theta(2\delta t))^5\ L_R(20\ \delta t)(L_\Theta(2\delta t))^5\ (L_X(\delta t))^{10}\ ]\ U^n_{j,k,\ell} \tag{57}$$

where the notation $(L_\Theta(p\delta t))^m$ means m successive applications of the L_Θ operator with a time step of p times δt.

BOUNDARY CONDITIONS AND SPECIAL TOPICS

The computational domain illustrated in Figure 8 is bounded by open surfaces (flow may cross surfaces), solid walls and inflow-outflow boundaries. Formulations and implementation of boundary conditions at each surface and Kutta condition are discussed in this section.

Solid Wall Boundary Conditions

The solid wall boundary condition appropriate for inviscid flow computations is that of zero mass flux through the surface. This condition is difficult to impose with uniform numerical accuracy in Euler equation simulations because of difficulties in evaluating derivatives of fluid properties and velocities at the wall. In potential flow calculations this difficulty does not appear since this boundary condition reduces simply to derivative of potential in direction normal to wall, being identically zero.

A concise illustration of the problem is given by considering the integration of the continuity equation in two dimensions, as illustrated in Figure 9. The continuity equation is:

$$\frac{\partial \rho}{\partial t} + \frac{\partial}{\partial x}(\rho u) + \frac{\partial}{\partial y}\cdot(\rho v) = 0 \qquad (58)$$

or since $v \equiv 0$ at wall

$$\frac{\partial \rho}{\partial t} + \frac{\partial}{\partial x}(\rho u)\bigg|_0 + \rho\left(\frac{\partial v}{\partial y}\right)\bigg|_0 = 0 \qquad (59)$$

If the continuity equation is to be numerically integrated using an explicit technique, the term $\left.\frac{\partial}{\partial x}(\rho u)\right|_0$ provides no difficulties but the term $\left.\rho\left[\frac{\partial v}{\partial y}\right]\right|_0$ is difficult to evaluate with more than first order accuracy. Using Taylor series:

$$v_{i,1} = v_{i,0} + \left.\left(\frac{\partial v}{\partial y}\right)\right|_0 \delta y + \left.\left(\frac{\partial^2 v}{\partial y^2}\right)\right|_0 \frac{\delta y^2}{2} + \mathcal{O}(\delta y^3) \tag{60}$$

$$\left.\left(\frac{\partial v}{\partial y}\right)\right|_0 = \frac{v_{i,1}}{\delta y} - \left.\left(\frac{\delta^2 v}{\delta y^2}\right)\right|_0 \frac{\delta y}{2} + \mathcal{O}(\delta y^2) \tag{61}$$

No information about the second derivative of v is available to enable evaluation to second order accuracy.

It is important to remember that this difficulty occurs for both the conservation and non-conservation law forms of the continuity and energy equations. In more complex flow geometries, where some type of body fitted coordinate system like that introduced in the previous section is used, this problem is not solved, only disguised.

Several numerical flow solutions have been published using this reflection formulation with apparent good results (see references 10 and 11). In addition Kreiss[12] has demonstrated that for linear hyperbolic equations it is sufficient for global n^{th} order accuracy to maintain $n-1^{th}$ order accuracy at the boundaries. The relevance of this statement for the Euler equations which are hyperbolic but nonlinear has not been established, but published solutions indicate that it may be at least a good guide for boundary conditions formulation.

For simple flows or two-dimensional supersonic flows, the method of characteristics may be used to compute flow solutions. Abbett[13] has published a comparison of several boundary condition approximations coupled with second order accurate solution schemes, MacCormack's method in particular, with method of characteristic solutions. Abbett found that indeed the simple first order accurate scheme for $\left[\frac{\partial v}{\partial y}\right]\Big|_0$ usually provided more accurate answers than more complicated schemes to calculate $\left[\frac{\partial v}{\partial y}\right]\Big|_0$ with second order accuracy. Another important result was that second order accurate approximations using one-sided difference expressions often gave very poor results.

It is important to recognize that these problems with specifying the solid wall boundary conditions exist only for integrating the fluid equations on the solid boundary. To integrate the fluid equations for interior points only the pressure on the solid boundary must be known. Solid boundaries, hub and tip casings or blade surfaces are mapped to coincide with coordinate surfaces which means that the contravariant velocity components U_R, U_Θ, U_X (equations 30, 31, and 32) will be identically zero on these surfaces. MacCormack's method or any scheme using centered spatial differencing will require either $\overline{F}$ or $\overline{G}$, equation 24 or 26, on the boundary but not both. If $U_R = 0$, $\overline{F}$ is determined only by the wall pressure and known coordinate derivatives. If $U_\Theta = 0$, $\overline{G}$ is also determined by the wall pressure and known coordinate derivatives.

Fortunately the wall pressure can be calculated using the momentum equation in the direction normal to the solid surface. Following reference 10, the normal momentum equation may be expressed as:

$$\left(\frac{\partial P}{\partial n}\right)_{j,k,0} = \left\{ (\rho) \left(\frac{u_s^2}{R_s} + \frac{u_\tau^2}{R_t}\right) - \bar{n} \cdot \left[2\,\Omega\,(\hat{i}_z \times \bar{V}_{rel}) - \Omega^2 r\, \hat{i}_r\right]\right\}_{j,k,0} \tag{62}$$

where $\bar{n}$ is the surface normal, Ω is the blade row rotation speed, u_s and u_τ are streamwise velocity components in the orthogonal boundary layer like coordinate shown in Figure 10, R_s and R_τ are surface radii of curvature in this coordinate system, and $(\hat{i}_r, \hat{i}_r)$ are unit vectors of the base (r,θ,z) coordinate system.

To be consistent with MacCormack's second order accurate scheme, $(\partial P/\partial n)_{j,k,0}$ should be evaluated with second order accuracy. This can be done even though $(\rho)_{j,k,0}$, $(u_s)_{j,k,0}$ and $(u_\tau)_{j,k,0}$ are unknown, by using:

$$(\rho)_{j,k,0} = (\rho)_{j,k,1} + \left(\frac{\partial \rho}{\partial n}\right)_{j,k,1} \delta n + \mathcal{O}(\delta n)^2 \tag{63}$$

$$(u_s)_{j,k,0} = (u_s)_{j,k,1} + \left(\frac{\partial u_s}{\partial n}\right)_{j,k,1} \delta n + \mathcal{O}(\delta n)^2 \tag{64}$$

$$(u_\tau)_{j,k,0} = (u_\tau)_{j,k,1} + \left(\frac{\partial u_\tau}{\partial n}\right)_{j,k,1} \delta n + \mathcal{O}(\delta n\ )^2 \tag{65}$$

The term $(\rho u_s^2/R_s)$ can be approximated by

$$\frac{\left\{(\rho)_{j,k,1} + \left(\frac{\partial \rho}{\partial n}\right)_{j,k,1} \delta n + \mathcal{O}(\delta n^2)\right\}\left\{(u_s^2)_{j,k,1} + 2\,u_s\left(\frac{\partial u_s}{\partial n}\right)_{j,k,1} \delta n + \mathcal{O}(\delta n^2)\right\}}{R_s}$$

$$= \frac{1}{R_s}\left\{(\rho u_s^2)_{j,k,1} + \left[(u_s^2)\left(\frac{\partial \rho}{\partial n}\right)\delta n\right]_{j,k,1} + 2\left(\rho\, u_s\, \frac{\partial u_s}{\partial n}\delta n\right)_{j,k,1}\right\} + \mathcal{O}(\partial n^2) \tag{66}$$

and so be evaluated with accuracy $\mathcal{O}(\delta n^2)$ if $(\partial\rho/\partial n)_{j,k,1}$ and $(\partial u_s/\partial n)_{j,k,1}$ are evaluated with accuracy $\mathcal{O}(\delta n)$. These derivatives can be evaluated with this accuracy by a number of schemes; simple extrapolation, or the first step of MacCormack's method are two examples. The remaining two terms $\rho(u_\tau^2/R_t)$ and $\Omega(\hat{i}_z x\overline{V}_{rel})$ may be expressed similarly.

An important aside at this point is that there is some theoretical basis, Kreiss reference 12, for the assumption that $(\partial P/\partial n)$ need be evaluated with only accuracy $\mathcal{O}(\delta n)$. This evaluation, using (66) as a guide, requires only that we use $(\rho)_{j,k,0} = (\rho)_{j,k,1}$, $(u_s)_{j,k,0} = (u_s)_{j,k,1}$ and $(u_\tau)_{j,k,0} = (u_\tau)_{j,k,1}$.

A comparative study conducted with reference 14 has shown this particular scheme, with first order accurate $(\partial P/\partial n)$ evaluation, to be the best available scheme for mixed supersonic and subsonic flows. For purely supersonic two-dimensional flows, the method of characteristic type boundary formulations proved best. For purely subsonic irrotational flows, all schemes tested were adequate. The scheme proposed here performed well in both flow regimes, and for these two-dimensional flow tests almost never required artificial damping for stability.

While $(\partial P/\partial n)$ is easily calculated numerically, the determination of the wall pressure requires that this pressure gradient be expressed in the stretched coordinate system (R,Θ,X). The normal pressure gradient is simply the dot product of gradient P and the unit normal vector.

$$\left(\frac{\partial P}{\partial n}\right) = (\nabla P) \cdot \bar{n} \tag{67}$$

The components of $\bar{n}$, in physical space, are $[\gamma_r, \gamma_\Theta, \gamma_z]$. For simplicity the pressure calculation on the hub or tip casing will be discussed, which means that $\gamma_\Theta \equiv 0$. The expanded form of equation (67) is

$$\left(\frac{\partial P}{\partial n}\right) = \left[\left(\frac{\partial P}{\partial r}\right) \hat{i}_r + \frac{1}{r}\left(\frac{\partial P}{\partial \theta}\right) \hat{i}_\theta + \left(\frac{\partial P}{\partial z}\right) \hat{i}_z\right] \cdot \left[(\gamma_r, 0, \gamma_z)\right] \tag{68}$$

or

$$\frac{\partial P}{\partial n} = \gamma_r\left[\left(\frac{\partial P}{\partial R}\right)\frac{\partial R}{\partial r} + \frac{\partial P}{\partial X}\frac{\partial x}{\partial r}\right] + \gamma_z\left[\left(\frac{\partial P}{\partial R}\right)\frac{\partial R}{\partial Z} + \left(\frac{\partial P}{\partial X}\right)\frac{\partial X}{\partial Z}\right] \tag{69}$$

Finally the pressure gradient may be expressed as:

$$\left(\frac{\partial P}{\partial n}\right) = \left[\left(\gamma_r \frac{\partial R}{\partial r}\right) + \left(\gamma_z \frac{\partial R}{\partial Z}\right)\right]\frac{\partial P}{\partial R} + \left[\left(\gamma_r \frac{\partial X}{\partial r}\right) + \left(\gamma_Z \frac{\partial X}{\partial Z}\right)\right]\frac{\partial P}{\partial X} \tag{70}$$

This expression for $(\partial P/\partial n)$ may be considered as defining the components of $\bar{n}$ in the computational space.

$$\bar{n}_{comp} = \left[\left(\gamma_r \frac{\partial R}{\partial r} + \gamma_Z \frac{\partial R}{\partial Z}\right), 0, \left(\gamma_r \frac{\partial X}{\partial r} + \gamma_Z \frac{\partial X}{\partial Z}\right)\right] \tag{71}$$

Equation (70) expresses the pressure gradient along one grid line, $(\partial P/\partial R)$, in terms of the normal pressure gradient, $(\partial P/\partial n)$, and the pressure gradient along a second grid line, $(\partial P/\partial X)$. The pressure gradient $(\partial P/\partial R)$ may be used to find the wall pressure.

Using the notation of Figure 9, the wall pressure, $P_{j,k,0}$, may be found as:

$$P_{j,k,0} = P_{j,k,1} - \left(\frac{\partial P}{\partial R}\right)_{j,k,0} \delta R \quad \text{if } \left(\frac{\partial P}{\partial n}\right) \text{ is known to } \mathcal{O}(\delta n) \tag{72}$$

or

$$P_{j,k,0} = \frac{1}{3}\left[4\,P_{j,k,1} - P_{j,k,2} - 3\left(\frac{\partial P}{\partial R}\right)_{j,k,0} \delta R\right] \quad \text{if } \left(\frac{\partial P}{\partial n}\right) \text{ is} \tag{73}$$

known to $\mathcal{O}(\delta n^2)$. Similar relations for the blade surface pressure may be derived.

Problem Areas within the Standard Boundary Formulation

The standard boundary formulation of equations (62), (70) and (72) or (73) while complete suffers from several practical problems which have limited its full application. The difficulties are that all boundary points are now "linked" and must be solved for simultaneously, that pressure is ill-defined at corner points, and that surface radii of curvature, R_s and R_τ, are difficult to calculate accurately.

The appearance of $(\partial P/\partial X)_{j,k,0}$ in equation (70) is responsible for linking the boundary points together since it must also be approximated by a finite difference expression:

$$\left(\frac{\partial P}{\partial X}\right)_{j,k,0} = \left[P_{j+1,k,0} - P_{j-1,k,0}\right] \Big/ 2\,\Delta X \tag{74}$$

for example. This linking problem is quite vexing for a purely explicit calculation and has been dealt with by the expedient of lagging the calculation one time step so that $(\partial P/\partial X)_{j,k,0}$ at time level n is approximated by $(\partial P/\partial X)_{j,k,0}$ at time level (n-1). This approximation is quite good for the steady state or quasi-steady state problems generally encountered, and has also been used with good results in references 10 and 15.

Corner points in a three-dimensional calculation present a difficult problem in these calculations since multiple definition of pressure at these points can occur. The standard formulation provides little guidance on the proper choice since the bounding surfaces are not orthogonal. The importance of proper definitions is illustrated by the disparity in reported solutions for external flow corner problems in references 16 and 17. The corner point problem has, in spite of its importance, been superceded by the problem of accurate calculation of surface radii of curvature R_S and R_T. An illustration of this problem is shown in Figure 11, which shows a typical supersonic blade section and the surface radius of curvature calculated from manufacturing coordinates using both spline fit procedures and finite difference procedures. Curvatures are seen to be quite irregular and even discontinuous at $x/C = 0.7$. These specific problem areas plus general difficulty in calculating second derivatives from manufacturing coordinates implies that the surface radii of curvature are known to first order accuracy at best.

Since the curvatures are known, with present coordinate specifications, to only first order, the first order accurate equations for $(\partial P/\partial n)$ and wall pressure are sufficient. The radii of curvature variations do of course cause oscillations in the wall pressure, but more importantly oscillations in $(\partial P/\partial X)_{j,k,0}$ which is an important term in equation (70). In blade tip sections these errors usually produce unacceptable variations in wall pressure and in extreme cases instability. When accurate curvatures are available (for example in the calculations presented in references 10 and 18, these problems do not exist; but in order to proceed with calculations for less accurately known blade shapes, some further assumption is needed.

The best practical assumption appears to be evaluating $(\partial P/\partial X)$ at location $\ell = 1$ and not $\ell = 0$. This assumption, coupled with first order accurate evaluation of $(\partial P/\partial n)$, is equivalent to evaluating $(\partial P/\partial n)$ on grid line $\ell = 1$ with the assumption that the streamline radii of curvature are equal to R_s and R_τ.

Boundary Conditions in a Staggered Grid System

The flux preserving boundary formulations discussed above have been used with the weak conservation law form, equations (18), but a more natural grid system for the non-conservation law forms, equations (17) was suggested by Roache.[11] This system retains most of the advantages of the flux preserving boundary conditions while making the imposition of periodic boundary conditions of the blade row and the Kutta condition much easier. This mesh system and the equations (17) are included in the associated computer codes as well as the weak conservation law forms and consistently give good results. This mesh system illustrated in Figure 12 has no grid lines on the solid boundary, but maintains the solid boundary midway between an interior grid line and a dummy grid line. Meaningful fluid quantities are calculated only for points interior to the flow and the exterior points are defined only to implement the flux preserving boundary conditions. Wall quantities are defined as having average values of

$$f_{i,w} = \frac{1}{2}\left[f_{i,1} + f_{i,2}\right] \qquad (75)$$

For the two dimensional example illustrated in Figure 12, dummy values of density, velocities and energy are found from reflection:

$$\rho_{i,2} = \rho_{i,1} \qquad u_{i,2} = u_{i,1} \qquad e_{i,2} = e_{i,1} \qquad v_{i,2} = -v_{i,1} \tag{76}$$

The pressure is found as in the first mesh systems from equation (70). Following Roache,[11] these relations may be seen to be nearly equivalent to the flux preserving conditions.

First, $v_w = \frac{1}{2}\,(v_{i,2} + v_{i,1}) = 0$ as desired. Then wall mass flow

$$(\rho v)_w = \left(\frac{\rho_{i,1} v_{i,1} + \rho_{i,2} v_{i,2}}{2}\right) = \rho_{i,1} v_w = 0 \quad \text{as desired.} \tag{77}$$

Next wall momentum flux

$$(\rho v^2)_w = \frac{1}{2}\left[\rho_{i,1} v_{i,1}^2 + \rho_{i,2} v_{i,2}^2\right] = \rho_{i,1} v_{i,1}^2 \neq 0 \tag{78}$$

Thus this formulation does not directly conserve normal momentum flux. As Roache[11] points out, this flux term is still consistent with the original equation in the limit of $(\delta x, \delta y) \to 0$. Evaluating the momentum flux term as would occur in any centered explicit scheme yields:

$$\begin{aligned}
\frac{\partial}{\partial y}(\rho v^2)\Big|_{w+1} &= \frac{1}{\delta y}\left[(\rho v^2)_{w+1\frac{1}{2}} - (\rho v^2)_{w+\frac{1}{2}}\right] = \frac{1}{\delta y}\left[(\rho v^2)_{w+1\frac{1}{2}} - (\rho v^2)_{w+1}\right] \\
&= \frac{1}{\delta y}\left[(\rho v^2)_{w+1\frac{1}{2}} - \rho_{w+1}\left[v_w + \frac{\delta y}{2}\frac{\partial v}{\partial y}\Big|_w + \mathcal{O}(\delta y)^2\right]\right] \\
&= \frac{(\rho v^2)_{w+1\frac{1}{2}}}{\delta y} - \left[\rho_{w+1}\left(\frac{\partial v}{\partial y}\right)\Big|_w^2 \frac{\delta y}{4} + \mathcal{O}(\delta y^2)\right]
\end{aligned} \tag{79}$$

as $(\delta y) \rightarrow 0$, $\frac{\partial}{\partial y}(\rho v^2)_{i,1} \rightarrow \frac{\rho v^2{}_{w+1\frac{1}{2}}}{\delta y}$ as desired, so that system is consistent.

Periodic Boundaries

One advantage of the staggered grid system is the logical simplification it brings to periodic boundaries as well as to leading and trailing edge conditions. This grid system is illustrated in Figure 13 for the blade-to-blade plane. Since no grid points are on the blade boundary, there are no stagnation streamline like grid lines which divide and go around a blade. Since the X and R grid stretchings are independent of θ, the blade-to-blade running grid lines remain at constant (r,z) positions. The periodicity conditions are implemented simply by using the fact that the conditions at k=1 are those of k=NTH-1 and conditions at k=NTH are those of k=2 as shown in Figure 13.

For the nonstaggered grid illustrated in Figure 9, periodicity may be maintained by:

$$\hat{U}^{*}_{j,NTH,\ell} = \hat{U}^{n}_{j,NTH,\ell} - \frac{\delta t}{\delta\Theta}\left(\hat{G}^{n}_{j,NTH,\ell} - \hat{G}^{n}_{j,NTH-1,\ell}\right)$$

$$\hat{U}^{*}_{j,1,\ell} = \hat{U}^{n}_{j,1,\ell} - \frac{\delta t}{\delta\Theta}\left(\hat{G}^{n}_{j,1,\ell} - \hat{G}^{n}_{j,NTH-1,\ell}\right) \qquad (80)$$

and

$$\hat{U}^{n+1}_{j,NTH,\ell} = 0.5*\left(\hat{U}^{n}_{j,NTH,\ell} + \hat{U}^{*}_{j,NTH,\ell} - \frac{\delta t}{\delta\Theta}\left(\hat{G}^{*}_{j,N\ 2,\ell} - \hat{G}^{*}_{j,NTH,\ell}\right)\right) \qquad (81)$$

$$\hat{U}^{n+1}_{j,1,\ell} = 0.5*\left(\hat{U}^{n}_{j,1,\ell} + \hat{U}^{*}_{j,1,\ell} - \frac{\delta t}{\partial\Theta}\left(\hat{G}^{*}_{j,2,\ell} - \hat{G}^{*}_{j,1\ \ell}\right)\right)$$

If $U^n_{j,1,\ell} = U^n_{j,NTH,\ell}$, the periodicity condition, then $U^{n+1}_{j,1,\ell} = U^{n+1}_{j,NTH,\ell}$.

Upstream or Inflow Boundary Conditions

Work described in this report has concentrated on isolated transonic compressor rotors for which it is difficult to establish proper inflow upstream boundary conditions. It is well known that the bow shock system of such rotors produces an upstream disturbance that, while small, propagates far upstream as an acoustic disturbance. Two different studies have concentrated on this problem, reference 19 for small disturbance theories and reference 20 for full Euler equation simulations. These studies adopted a common model, that of an isolated rotor operating in an infinite duct. The flow upstream is assumed to obey linear potential equations with the near field and the far-field potentials matched on a surface several chords upstream of the rotor. The upstream potential is expressed as the sum of three components: a uniform axial flow, a two dimensional axisymmetric perturbation and a three dimensional perturbation.

$$\phi_{up} = \phi_{uniform} + \phi_{axi}(r,Z) + \phi_{3D}(r,\theta,Z) \tag{82}$$

Extensive simulations for one rotor geometry in reference 19 using non-reflecting boundary conditions showed that if the matching plane was located three or more axial chords upstream then setting $\phi_{3D}(r,\theta,Z)\equiv 0$ was an adequate approximation for the near-field solution. These same simulations also demonstrated that the axisymmetric disturbance remained important even three chords upstream. Nearly the same conclusions were reached in reference 20 for two different configurations.

These potential flow results suggest that if computational domains extend at least 4 to 5 chords upstream of an isolated rotor then it is not necessary to model either the three-dimensional or axisymmetric disturbances. Computational domains of this extent greatly increase computation times and domains extending no more than 2 to 3 chords upstream are desired for reasonable computation times. Computational domains of this extent require that the axisymmetric disturbances be modeled with reasonable accuracy.

A simple upstream flow model which can be used to simulate either potential or axisymmetric rotational upstream flows was proposed in reference 10. This model represents the upstream flow as an unsteady axisymmetric base flow plus a more general but small disturbance. For the boundary conditions adopted for this report, the small disturbance will be neglected; in the potential flow case this is equivalent to neglecting $\phi_{3D}(r,\theta,Z)$. The unsteady base flow is assumed to evolve from a steady axisymmetric "far-upstream" base flow, which is partially specified and partially computed from the interior solution. These boundary conditions are derived by representing the velocity as:

$$\bar{V} = \bar{V}(t,r,z) \tag{83}$$

the pressure as:

$$P = P(t,r,z) \tag{84}$$

and the density as:

$$\rho = \rho(t,r,z) \tag{85}$$

Note that this definition will include both ϕ_{uniform} and ϕ_{axi} from reference 19 in the base flow $\bar{V}_o$ and P_o.

The equations describing the base flow are continuity and the three momentum equations and continuity:

$$\frac{D\bar{V}}{Dt} = -\frac{\nabla p}{\rho} \tag{86}$$

and

$$\frac{D\rho}{Dt} + (\rho\bar{V}) = 0 \tag{87}$$

The base flow is also assumed to be isentropic.

Using as a coordinate system the modified cylindrical coordinate system shown below, the equation of motion may be written in terms of the tangential velocity and the meridional velocity,

$$\bar{V}_m = V_r \hat{i}_r + V_z \hat{i}_z$$

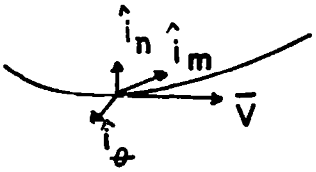

The equations of motion written in a general orthogonal curvilinear coordinate system are

$$\frac{\partial\rho}{\partial t} + \frac{1}{h_m h_n h_\theta}\left[\frac{\partial}{\partial n}(h_m h_\theta \rho u_n) + \frac{\partial}{\partial m}(h_n h_\theta \rho u_m) + \frac{\partial}{\partial\theta}(h_n h_m \rho u_\theta)\right] = 0$$

$$\frac{\partial u_n}{\partial t} + \frac{u_n}{h_n}\frac{\partial u_n}{\partial n} + \frac{u_m}{h_m}\frac{\partial u_n}{\partial m} + \frac{u_\theta}{h_\theta}\frac{\partial u_n}{\partial\theta} + \frac{u_n u_m}{h_n h_m}\frac{\partial h_n}{\partial m} + \frac{u_n u_\theta}{h_n h_\theta}\frac{\partial h_n}{\partial\theta} \tag{88}$$

$$-\frac{u_m^2}{h_n h_m}\frac{\partial h_m}{\partial n} - \frac{u_\theta^2}{h_n h_\theta}\frac{\partial h_\theta}{\partial n} = -\frac{1}{\rho h_n}\frac{\partial p}{\partial n}$$

$$\frac{\partial u_\theta}{\partial t} + \frac{u_n}{h_n}\frac{\partial u_\theta}{\partial n} + \frac{u_m}{h_m}\frac{\partial u_\theta}{\partial m} + \frac{u_\theta}{h_\theta}\frac{\partial u_\theta}{\partial \theta} + \frac{u_\theta u_m}{h_\theta h_m}\frac{\partial h_\theta}{\partial m} + \frac{u_\theta u_n}{h_\theta h_n}\frac{\partial h_\theta}{\partial n} \tag{89}$$

$$-\frac{u_m^2}{h_m h_\theta}\frac{\partial h_m}{\partial \theta} - \frac{u_n^2}{h_n h_\theta}\frac{\partial h_n}{\partial \theta} = -\frac{1}{\rho h_\theta}\frac{\partial p}{\partial \theta}$$

$$\frac{\partial u_m}{\partial t} + \frac{u_n}{h_n}\frac{\partial u_m}{\partial n} + \frac{u_m}{h_m}\frac{\partial u_m}{\partial m} + \frac{u_\theta}{h_\theta}\frac{\partial u_m}{\partial \theta} + \frac{u_m u_n}{h_m h_n}\frac{\partial h_m}{\partial n} + \frac{u_m u_\theta}{h_m h_\theta}\frac{\partial h_m}{\partial \theta} \tag{90}$$

$$-\frac{u_\theta^2}{h_m h_\theta}\frac{\partial h_\theta}{\partial m} - \frac{u_n^2}{h_n h_\theta}\frac{\partial h_n}{\partial m} = -\frac{1}{\rho h_m}\frac{\partial p}{\partial m}$$

Since $u_n = 0$, by definition and $\frac{\partial}{\partial \theta} = 0$ by assumption, these equations reduce for the base flow to,

$$\frac{\partial u_m}{\partial t} + \frac{u_m}{h_m}\frac{\partial h_m}{\partial m} - \frac{u_\theta^2}{h_m h_\theta}\frac{\partial h_\theta}{\partial m} = -\frac{1}{\rho h_m}\frac{\partial p}{\partial m} \tag{91}$$

$$\frac{\partial \rho}{\partial t} + \frac{1}{h_m}\frac{\partial(\rho u_m)}{\partial m} + \rho u_m\left[\frac{1}{h_n h_m h_\theta}\frac{\partial(h_n h_\theta)}{\partial m}\right] = 0 \tag{92}$$

$$\frac{\partial u_\theta}{\partial t} + \frac{u_m}{h_m}\frac{\partial u_\theta}{\partial m} + \frac{u_\theta u_m}{h_m h_\theta}\frac{\partial h_\theta}{\partial m} = 0 \tag{93}$$

$$-\frac{u_m^2}{h_m h_n}\frac{\partial h_m}{\partial n} - \frac{u_\theta^2}{h_n h_\theta}\frac{\partial h_\theta}{\partial n} = -\frac{1}{\rho h_n}\frac{\partial p}{\partial n} \tag{94}$$

The first two equations may be rewritten in characteristic form using the isentropic relation, $dp = a^2 d\rho$, as

$$\frac{\partial u_m}{\partial t} + \frac{u_m}{h_m}\frac{\partial u_m}{\partial m} + \frac{1}{\rho h_m}\frac{\partial p}{\partial m} = \frac{u_\theta^2}{h_m h_\theta}\left(\frac{\partial h_\theta}{\partial m}\right) \tag{95}$$

and

$$\frac{1}{\rho a}\frac{\partial p}{\partial t} + \frac{u_m}{\rho a h_m}\frac{\partial p}{\partial m} + \frac{a}{h_m}\frac{\partial u_m}{\partial m} = -\frac{a u_m}{h_n h_m h_\theta}\frac{\partial(h_\theta h_n)}{\partial m} \tag{96}$$

Adding and subtracting these equations yields

$$\left[\frac{\partial u_m}{\partial t} \pm \frac{1}{\rho a} \frac{\partial p}{\partial t} \right] + \frac{1}{h_m} \left[(u_m \pm a) \frac{\partial u_m}{\partial m} + (u_m \pm a) \frac{1}{\rho a} \frac{\partial p}{\partial m} \right] = \frac{u_\theta^2}{h_m h_\theta} \frac{\partial h_\theta}{\partial m} \mp \frac{a u_m}{h_n h_m h_\theta} \frac{\partial (h_\theta h_n)}{\partial m} \qquad (97)$$

or

$$\frac{D^+ J^+}{Dt} = \frac{u_\theta^2}{h_m h_\theta} \frac{\partial h_\theta}{\partial m} - \frac{a u_m}{h_m h_\theta h_n} \frac{\partial}{\partial m} (h_\theta h_n) \qquad (98)$$

where

$$J^+ = u_m + \frac{2}{\gamma - 1} a$$

and

$$\frac{D^+}{Dt} = \frac{\partial}{\partial t} + \frac{u_m}{h_m} \frac{\partial}{\partial m}$$

$$\frac{D^- J^-}{Dt} = \frac{u_\theta^2}{h_m h_\theta} \frac{\partial h_\theta}{\partial m} + \frac{a u_m}{h_m h_\theta h_n} \frac{\partial}{\partial m} (h_\theta h_n) \qquad (99)$$

where

$$J^- = u_m - \frac{2}{\gamma - 1} a$$

and

$$\frac{D^-}{Dt} = \frac{\partial}{\partial t} - \frac{u_m}{h_m} \frac{\partial}{\partial m}$$

The third equation, (93), is already in characteristic form.

$$\frac{D u_\theta}{Dt} = - \frac{u_\theta u_m}{h_\theta h_m} \frac{\partial h_\theta}{\partial m} \qquad (100)$$

A fourth characteristic also exists and has been chosen to be

$$\frac{Ds}{Dt} = 0 \tag{101}$$

which implies that an isentropic flow exists along each streamline from the "far-upstream" condition to the computational domain inflow boundary.

At each point on the inflow boundary four pieces of information must be supplied in order to calculate the flow variables. For transonic compressor rotors, the upstream meridional Mach number is always less than one, and the J^- characteristic is an upstream running characteristic. The J^+ characteristic is always a downstream running characteristic. The characteristics associated with equations (100) and (101) are simply the convection path. Thus three pieces of information may be specified independently at the inflow boundary.

This situation is illustrated for a single spatial dimension in Figure 14. For this formulation the solution does not exist for $x < 0$ and is assumed to be known at time level $n\delta t$. At the node point $(n+1, 1)$ three characteristics are incident: a convection characteristic, an upstream running J^-_i characteristic, and a downstream running J^+_r characteristic. The value of the J^-_i characteristic is known, but the information carried along the remaining characteristics must be specified.

$$(J^+_r)^{n+1}_1 = \left(u_m\right)^{n+1}_1 + \frac{2}{\gamma-1} a^{n+1}_1 \tag{102}$$

$$(J^-_i) = \left(u^{n+1}_m\right)_1 - \frac{2}{\gamma-1} a^{n+1}_1 = \left(u^n_m\right)_2 - \frac{2}{\gamma-1} a^n_2 \tag{103}$$

At the open boundary $(j=1)$, $(u_m)^{n+1}_1$ or a^{n+1}_1 may be specified in order to determine the J^+_r characteristic value. When a^{n+1}_1 is specified, J^+_r takes the value:

$$J^+_r = J^-_i + \frac{4}{\gamma-1} a_1^{n+1} \qquad (104)$$

When $(u_{m_1})^{n+1}$ is specified, J^+_r takes the value

$$J^+_r = 2(u_{m_1})^{n+1} J^-_i \qquad (105)$$

For the computer codes described in the report, the inflow boundary is assumed to be located far enough upstream that the radius of curvature of streamlines is large enough that the curvature term $(1/h_m h_\theta)(\partial h_\theta/\partial m)$ may be neglected. The resulting equations describing the upstream flow are:

$$\frac{D^+J^+}{Dt} = 0 \qquad (106)$$

$$\frac{D^-J^-}{Dt} = 0 \qquad (107)$$

$$\frac{Du_\theta}{Dt} = 0 \qquad (108)$$

$$\frac{Ds}{Dt} = 0 \qquad (109)$$

The constraint equation, equation (94), is not used and the grid is constructed such that the hub and tip casing slope are zero at the inflow boundary so that u_r may be assumed to be zero.

Two input options are provided in the computer code for specifying the inflow boundary condition. The primary option uses the freedom to specify a_1^{n+1} to maintain constant values of total pressure and total temperature at the inflow boundary. The user may specify the values of total pressure and temperature as a function of radius but may not specify the inlet velocity. This option is the normal one and does not specify the inlet mass flow rate. With some initial conditions, this inflow boundary condition option can become unstable. A second option is provided for use with the unstable option 1 cases. In option 2, the value of the downstream running characteristic, J_r^+, is specified directly by specifying the desired value of the uniform far-upstream Mach number. The value of the J_r^+ characteristic is calculated as:

$$J_r^+ = (u_m)_{up} + \frac{2}{\gamma-1} a_{up} = \left(\frac{a_{up}}{a_o}\right) a_o \left(M_{up} + \frac{2}{\gamma-1}\right) \qquad (110)$$

Use of option 2 will usually lead to a small total pressure error at the inflow boundary.

For both options, once values for J_r^+ and J_i^- are known, the values of u_1^{n+1} and a_1^{n+1} are calculated using equations (102) and (103). The values of T_1^{n+1}, ρ_1^{n+1}, e_1^{n+1} are calculated using the input values of total temperature and the isentropic flow relations. The value of $(u_\theta)_1^{n+1}$ is specified by the user and the radial velocity $(u_r)_1^{n+1}$ is assumed to be zero. For option 2, the J_r^+ characteristic value is specified by the user, while, for option 1 the J_r^+ characteristic value is selected through iteration on the value of a_1^{n+1} to match the input value of total pressure.

Downstream or Outflow Boundary Conditions

Outflow boundary condition formulations closely follow the model for the inflow boundary conditions, equations (91) through (94). However, for subsonic flow, as shown in Figure 15, only one characteristic, J_r^-, brings information into the computation domain. For supersonic flow, no characteristics bring information into the computational domain. For subsonic flow, the information to be specified is the far-downstream static pressure, while, for supersonic flow, no downstream boundary condition may be imposed. The downstream boundary is assumed to be located far enough downstream that the streamline radius of curvature may be assumed to be zero and the radial velocity may be assumed to be zero. The equations to be solved are:

$$\frac{D^+J^+}{Dt} = 0 \tag{111}$$

$$\frac{Du_\theta}{Dt} = 0 \tag{112}$$

$$\frac{\partial P}{\partial r} = \frac{\rho u_\theta^2}{r} \tag{113}$$

and

$$\frac{Ds}{Dt} = 0 \tag{114}$$

Since the swirl velocity on the outflow boundary is determined by the interior solution, the exit static pressure may not be specified arbitrarily as a function of radius. To avoid this problem a static pressure on the inner casing is specified and the radial static pressure variation is calculated from equations (113) and (114). The exit static pressure variation is calculated by first extrapolating the theta-averaged values of J_i^+ and u_θ to the last computational plane (j=Nx) from the upstream computational planes (j=NX-1 and j=Nx-2). The resulting centrifugal force gradient at the outflow plane is balanced by the radial pressure gradient. The radial pressure gradient is calculated from equation (113), using the extrapolated values of u_θ and density, ρ, by trapezoidal rule integration. The final exit density and speed of sound, a, are then calculated using the isentropic flow assumption, equation (114). The exit velocity is then calculated from the value of the extrapolated J_1^+ characteristic. The radial velocity is also assumed to be zero.

These boundary conditions are equivalent to the physical constraints imposed when a compressor is tested. Inlet or reservoir conditions are specified, usually atmospheric stagnation conditions, and the inlet swirl velocity is specified, usually zero. Downstream of the compressor, some throttling device is used to determine the compressor operating point. A particular operating point is determined by the intersection of the compressor characteristic and the throttle characteristic. The operation of this device could be simulated by specifying either the compressor static pressure ratio or the mass flow. It is computationally somewhat easier to specify the rotor static pressure ratio.

No attempt was made to calculate the actual flow at the throttle or exit boundary, and hence account for the effect of disturbances there. Such a calculation, especially in the strongly rotating flow downstream of the rotor, is potentially as difficult as the through-flow calculation itself. This simplification does imply some inconsistencies at the boundaries, while at the upstream boundary the transmission of acoustic disturbances is falsified; at the downstream boundary vorticity convection is distorted. The acoustic disturbances carry very little energy and their falsification has been shown to have very little influence on the flow over the rotor. When the downstream perturbations are not calculated, the effective model of the flow beyond the downstream computational boundary is one which is axisymmetric and uniform in the streamwise direction. Such a flow can have no radial vorticity and is potentially inconsistent with the blade flow solution if that solution requires a significant amount of radial vorticity to be present at the computational boundary. For the present calculations, this inconsistency does not appear to be important even though some radial vorticity is shed by the rotor.

Kutta Condition

The Kutta condition, a uniqueness condition imposed on inviscid flow solutions in order to approximate the true viscous flow solution, is imposed quite simply for the compressor rotors studied. No attempt is made to model blunt or cusped trailing edges. Instead, the flow at the last axial grid points on the pressure and suction surfaces is assumed to be parallel to the blades and to have equal static pressures. This condition is adequate for compressor rotors designed to have subsonic outflow, but would require modification for turbine blade rows having supersonic outflow.

Spinners

Several attempts were made to model a spinner, including one that would smoothly merge with the centerline, but these attempts were unsuccessful. High radial velocities tended to build up at the points close to the centerline, resulting in mass flow defects of the order of 5%. Since $r=0$ is a singular point in a cylindrical coordinate system, the implementation of boundary conditions at the centerline can pose some problems. In addition, the centerline is a stagnation streamline, and stagnation points pose stability problems. In view of the above problems, the spinner was finally replaced by a cylindrical centerbody with a hub to tip ratio of 0.3. Several promising attempts to deal with centerline procedures in a cylindrical coordinate system have been published (see reference 21 for example), and the spinner problem should now be re-examined.

COMPUTER CODE DESCRIPTION

The numerical procedures previously described have been implemented in two computer programs. The first, MESH3D, generates the finite difference grids, interpolates blade geometry data from manufacturing coordinate sections to the finite difference grid, computes blade normal vectors and curvatures, and generates coordinate stretching derivatives $(\partial R/\partial r)$ etc. The second, BLADE3D, generates initial conditions if desired, integrates the appropriate equations of motion, and prints a solution matrix. A third program, GRAPH3D, produces two output files which may be used for user defined graphics and produces some rudimentary graphics output.

Grid Generation Program: MESH3D

The grid generation program has four important geometric inputs: 1) (r,z) coordinate pairs describing hub and tip casing shapes; 2) (r,z) coordinate pairs describing location of blade row leading and trailing edges; 3) (r,z) coordinate pairs describing damper geometry where applicable; and 4) (r,θ,z) coordinates describing the blade row geometry.

Operation of MESH3D on these geometric quantities is best described using Figure 16 (the axial grid numbering scheme) and Figure 17 (simplified MESH3D flow chart). The input to the main program is the grid numbering information, particularly the axial grid numbering scheme, which is necessary to size the finite difference grid and control its generation. Subroutine XRGRID controls the input of all axisymmetric geometric data and generates (r,z) coordinates of the finite difference grid and calculates some of the coordinate stretching derivatives $[(\partial X/\partial z), (\partial X/\partial r), (\partial R/\partial r), (\partial R/\partial z)]$. Subroutine CALT controls input of blade surface geometry, interpolates this data onto the finite difference grid, calculates blade normal vectors, and calculates blade radii of curvature. Subroutine BLDT calculates $[(\partial\Theta/\partial r)$, $(\partial\Theta/\partial\theta)$, and $(\partial\Theta/\partial z)]$ and creates an input file for BLADE3D containing all the required blade geometry information. Subroutine BUILD calculates hub and tip normal vectors as well as the radius of curvature along the axial direction, and subroutine SVGRID creates input files for BLADE3D containing all required information about grid coordinates.

Numerical Integration Program: BLADE3D

The numerical integration program is modular in operation, can be executed either on large mainframe computers or on minicomputers with a minimum of code changes, and is inherently restartable. A simplified flow chart of BLADE3D is shown in Figure 18. The main program input describes the axial grid numbering scheme (which is identical to that of MESH3D), describes the operator sequence to be executed, the integration time step, and the number of operator sequences to be executed. Subroutine OPEN begins the calculation setup process by reading two data files generated by MESH3D which describe the blade row geometry. Subroutine START completes the setup process either by reading a previous solution matrix (solution vector U at all grid points) or generating a new starting solution. Subroutine THREE controls printing of starting and final solutions as well as execution of the requested operator sequence. The finite difference operators equations (40-44) are implemented in subroutines BLOCKX, BLOCKT, and BLOCKR. Subroutine CLOSE outputs the final solution matrix. A lengthy calculation will usually be run in several sections, and this operation of START and CLOSE provides a needed restart capability since the intermediate results are available for backup.

Graphical Output Program: GRAPH3D

The graphics output program produces two solution matrix data files which contain all information needed for user defined graphics packages. The first file contains for each node point in the finite difference grid its physical space r,θ,z coordinates, the solution vector $[r\rho, r\rho u_r, r\rho u_\theta, r\rho u_z, rE_t]$ and a modified solution vector $[P_t, M_r, M_\theta, M_z, T_t]$. The second file contains the computed streamline positions inside the blade row volume. The starting point for each streamline calculation is a finite difference grid node at the rotor leading edge. This second file contains the (r,θ,z) coordinates of a streamline position and the solution vector at that point, $[r\rho, r\rho u_r, r\rho u_\theta, r\rho u_z, rE_t, P_t, M_r, M_\theta, M_z, T_t]$. The computed streamline positions thus correspond to the traditional S1 and S2 streamsurface definitions.

In addition to these data files, GRAPH3D also produces printer/plotter plots of blade surface pressure and Mach number for each radial grid plane and each S2 surface.

For user convenience, a subroutine, called USERREAD, is included with GRAPH3D which may be used to read the two solution matrix data files.

INPUT DICTIONARY FOR MESH3D

Input variables may be described in any consistent set of units since the MESH3D and BLADE3D programs contain only non-dimensional units. The length scale selected is usually the tip casing radius at the farthest point upstream; the velocity scale selected is the stagnation temperature speed of sound at this same point. Each time geometric quantities are input, a scaling factor is required which converts any dimensional geometric quantity into a nondimensional quantity. In this way, the most convenient set of units may be input for each geometric quantity, which is then nondimensionalized by the code. In addition when axial coordinates are input, a coordinate system origin adjustment factor is also required. This additive factor corrects possible coordinate origin differences between sets of geometric input. The input variables for MESH3D in the order they appear in Table 4.1, are the following:

Main Program Input

TITLE Title for problem identification, any information may appear in the first 70 columns.

NBL	Number of blades in row, must be ≥ 1.
NX	Number of axial grid planes, must be $3 \leq NX \leq 100$
NTH	Number of theta grid planes, must be $3 \leq NTH \leq 17$
NR	Number of radial grid planes' must be $3 \leq NR \leq 18$
*N1	Axial plane containing the blade row leading edge
*N2	Axial plane containing the blade row trailing edge

*Note: N2-N1 must be an even integer ≤ 50.

KUTTA	Axial plane at which Kutta condition is to be applied. KUTTA = N2 normally.
ILE	Axial plane containing the damper leading edge. A value of 0 indicates no damper.
ITE	Axial plane containing the damper trailing edge. A value of 0 indicates no damper.
SPHALF	Mesh type parameter. If = 0, then first mesh system is generated. If = 0.5 the second or staggered mesh system is generated. Only the staggered mesh may be used with the current version of BLADE3D, so SPHALF = 0.5 should be used.
IAN	Type of transform derivative calculation. If IAN = 0 then metric calculation done by finite difference method using node (r,θ,z) positions and if = 1 metric calculation is done by analytic functions. IAN = 1 is recommended.
IWR	FORTRAN unit number for MESH3D bulk output, may be equal to 6 or greater than 9.
IDMP	MESH3D debug output flag, allowable values are 0 => none (recommended value) 1 => SUBROUTINE GRID output 2 => SUBROUTINE INTER output 3 => SUBROUTINE GETTHA output 4 => SUBROUTINE CALDR output 5,6 => SUBROUTINE CALDER output -1 => All subroutines (not recommended)
KX	Axial coordinate packing factor. KX = 0.1 corresponds to non-packed grids. KX = 3.0 corresponds to highly packed grids. See special instruction number 1 for aid in selecting KX.
A1	Radial Grid line relaxation factor, used to make computational space grid lines approximate Z = constant lines near inflow and outflow boundary. A value of 3.0 appears to be best. See special instruction number 1 for aid in selecting A1.
TOL	Convergence tolerance on axial grid plane positions. A value of 0.0001 is a tight tolerance and a value of 0.001 is recommended.

IAB	Convergence choice parameter. A value of 0 will cause axial plane position calculation to abort after 10 iterations. Nonconvergence is usually caused by input errors in either tip and hub casing positions or leading and trailing edge positions. A value of 1 allows unconverged plane positions to be accepted. IAB = 0 is recommended.

Subroutine GRID Input

HUB Coordinates

NRH	Number of coordinate pairs describing hub casing contour. $2 \leq NRH \leq 50$.
SCALE1	Input hub coordinates will be scaled as: XH = (XH + ADJ1)/SCALE1 and RH = RH/SCALE1
ADJ1	
XH and RH	Coordinate Pairs describing hub casing contour.

TIP Coordinates

NRT	Number of coordinate pairs describing tip casing contours. $2 \leq NRT \leq 50$.
SCALE2	Input tip coordinates will be scaled as: XT = (XT + ADJ2)/SCALE2 and RT = RT/SCALE2
ADJ2	
XT and RT	Coordinate pairs describing tip casing contour.

Leading Edge Coordinates - See Also Special Instruction Number 2

NZLE	Number of coordinate pairs describing leading blade edge location. $2 \leq NZLE \leq 20$
SCALE3	Input leading edge variables scaled as: ZLE = (ZLE + ADJ3)/SCALE3 and RLE = RLE/SCALE3
ADJ3	
ZLE and RLE	Coordinate pairs describing blade leading edge contour.

Trailing Edge Coordinates

NZTE	Number of coordinate pairs describing blade trailing edge contour. $2 \leq NZTE \leq 20$
SCALE4	Input trailing edge variables scaled as: $ZTE = (ZTE + ADJ4)/SCALE4$ and $RTE = RTE/SCALE4$
ADJ4	

DAMPER COORDINATES - SKIP IF BLADE ROW HAS NO DAMPER

Damper Lower Surface

XTE, ZTE	Coordinate pairs describing blade trailing edge contour.
NZL	Number of coordinate pairs describing damper lower surface. $2 \leq NZL \leq 20$
SCALE5	Input damper lower surface variables will be scaled as: $ZLL = (ZLL + ADJ5)/SCALE5$ and $RL = RL/SCALE5$
ADJ5	
ZLL; RL	Coordinate pairs describing damper lower surface.

Damper Upper Surface

NZU	Number of coordinate pairs describing damper upper surface. $2 \leq NZU \leq 20$
SCALE6	Input variables will be scaled as: $ZU = (ZU + ADJ6)/SCALE6$ and $RU = RU/SCALE6$
ADJ6	
ZU, RU	Coordinate pairs describing damper upper surface contour.
C1	Location of damper in computational space. $0 < C1 < 1.0$; C1 may take only certain values, see special instruction number 3.

Subroutine CALT Input

TITLE2	Title Card for blade geometry input set.
NPTS	Number of points on a specification line, see Figure 19 and special instructions. Maximum value is 25.

NL	Number of stacked blade sections, see Figure 19. Maximum value is 15.
SCALE7	Input blade data scaled as: Z = (Z + ADJ7)/SCALE7 R = R/SCALE7
IM	Blade geometry input flag, either 0 or 1. See discussion below for option forms.
NBL	Number of blades in blade row.
ADJ7	Coordinate origin adjustment factor.
MID(I,J,K)	Three dimensional coordinate array of blade pressure and suction surface positions. First index varies from 1 to NL, while second index varies from 1 to NPTS. For the third index a value of 1 is used to store radial coordinate; a value of 2 is used to store axial coordinate; a value of 3 is used to store theta coordinate of pressure surface; a value of 4 is used to store theta coordinate of suction surface. See also special instruction number 4.

Variable	Comments
MID(1,J,1)	NPTS Z coordinate values for blade section #1
MID(NL,J,1)	NPTS Z coordinate values for blade section #NL
MID(1,J,2)	NPTS R coordinate values for blade section #1
MID(NL,J,2)	NPTS R coordinate values for blade section #NL
MID(1,J,3)	NPTS values of either θ_{MCL} or θ_{ps} for blade section #1
MID(NL,J,3)	NPTS values of either θ_{MCL} or θ_{ps} for blade section #NL
MID(1,J,4)	NPTS values of either θ_{t} or θ_{ss} for blade section #1
MID(NL,J,4)	NPTS values of either θ_{t} or θ_{ss} for blade section #NL

Special Notes and Restrictions on Input Variables for MESH3D

1. The best values of KX and A1 can only be determined by trial and error. A small value of KX (0.01) leads to nearly unpacked X-R grids, see figure 20. Larger values of KX progressively pack X-R grid planes near the blade leading and trailing edges while increasing the grid spacing in the far field, see figures 20 and 21. The best value of A1 depends on KX and should be selected after KX is selected, see figure 22.

2. Due to the placement of X-Θ grid planes outside the normal hub and tip casings, it is imperative that definitions of blade leading edge and trailing edge geometry be continued at least 10 percent of blade span outside the hub and tip casings.

3. The constant C_1 determines the part-span shroud placement in computational space. The restriction on shroud placement is that it must lie midway between two X-Θ grid planes. Thus the values of C_1 are restricted to FLOAT[(IDL-1)/(NR-2)]. IDL is the number of the X-Θ grid plane immediately below the damper. It is suggested that to generate a grid containing a part-span shroud that first a grid without a part-span shroud be generated. The values of ILE, ITE, and IDL may then be determined by inspection.

4. Blade geometry is given by four two-dimensional arrays, each row of which describes a blade section. Blade sections are numbered from 1 to NL. The first blade section at the hub and the last one at the tip shall not necessarily conform to the hub or tip casing profile, but may be given within the flow region, crossing the boundary, or completely outside of the boundary. Column 1 and column 2 are used to describe the axial and radial

positions of the blade section, while column 3 and column 4 will describe either the angular position of the mean camber line (in radians) and the tangential thickness (in radians) of the blade section or the angular position (in radians) of the blade pressure surface and the angular position of the suction surface of same blade. Option flag IM = 0 requires mean camber line and thickness while IM = 1 requires positions of pressure and suction surfaces. See Figure 23 for definition of tangential thickness. These blade coordinates are stored in the single three-dimensional array MID(I,J,K).

5. All variables allocated 5 columns in Table 4.1 are integer variables and must be right justified. All variables allocated 10 columns are real variables which should have decimal point included.

Table 4.1. Input Card Format for MESH3D

1	6	11	16	21	26	31	36	41	46	51	56	61	66	71	76
TITLE															
NBL															
NX	NTH	NR													
N1	N2	KUTTA	ILE	ITE											
SPHALF															
IAN															
IWR	IDMP														
KX		A1		TOL		IAB									
NRH	SCALE1		ADJ1												
XH(1)		RH(1)													
⋮		⋮							Hub Casing Coordinates						
XH(NRH)		RH(NRH)													
NRT	SCALE2		ADJ2												
XT(1)		RT(1)													
⋮		⋮							Tip Casing Coordinates						
XT(NRT)		XT(NRT)													
NZLE	SCALE3		ADJ3												
ZLE(1)		RLE(1)													
⋮		⋮							Leading Edge Coordinates						
ZLE(NZLE)		RLE(NZLE)													

1	6	11	16	21	26	31	36	41	46	51	56	61	66	71	76
NZTE	SCALE4		ADJ4												
XTE(1)		RTE(1)													
⋮		⋮													
XTE(NZTE)		RTE(NZTE)													

Trailing Edge Coordinates

*** NOTE NEXT SET OF DESCRIPTOR CARDS ***

*** ARE PRESENT ONLY IF A DAMPER IS ***

*** INCLUDED IN THE SOLUTION ***

1	6	11	16	21
NZL	SCALE5		ADJ5	
ZLL(1)		RL(1)		
⋮		⋮		
ZLL(NZL)		RL(NZL)		

Damper Lower Surface Coordinates

1	6	11	16	21
NZU	SCALE6		ADJ6	
ZU(1)		RU(1)		
⋮		⋮		
ZU(NZU)		RU(NZU)		
C1				

Damper Upper Surface Coordinates

*** NOTE INPUT SEQUENCE RESUMES HERE ***

*** IF NO DAMPER IS SELECTED ***

1	6	11	16	21	26	31	36
TITLE2							
NPTS	NL	SCALE7		IM	NBL	ADJ7	

1	11	21	31	41	51	61	71
MID(1,1,1) to MID(NPTS,1,1) NL SETS OF NPTS POINTS. BLADE Z COORDINATES.							
MID(1,2,1) to MID(NPTS,2,1)							
	⋮						
MID(1,NL,1) to MID(NPTS,NL,1)							
MID(1,1,2) to MID(NPTS,1,2) NL SETS OF NPTS POINTS. BLADE R COORDINATES.							
	⋮						
MID(1,NL,2) to MID(NPTS,NL,2)							
MID(1,1,3) to MID(NPTS,1,3) NL SETS OF NPTS POINTS. BLADE Θ_{MCL} OR Θ_{PS} COORDINATES							
	⋮						
MID(1,NL,3) to MID(NPTS,NL,3)							
MID(1,1,4) to MID(NPTS,1,4) NL SETS OF NPTS POINTS. BLADE t or Θ_{SS} COORDINATES.							
	⋮						
MID(1,NL,4) to MID(NPTS,NL,4)							

INPUT DICTIONARY FOR BLADE3D

The input variables for BLADE3D, in the order they appear in Table 4.2, are the following:

TITLE	Title for problem identification, any information may appear in the first 70 columns
NBL	Number of blades in row, must be ≥ 1
NX	Number of axial grid planes, must be $3 \leq NX \leq 100$
NTH	Number of theta grid planes, must be $3 \leq NTH \leq 17$
NR	Number of radial grid planes, must be $3 \leq NR \leq 18$
N1	Axial plane containing the blade row leading edge
N2	Axial plane containing the blade row trailing edge
KUTTA	Axial plane at which Kutta condition is to be applied. KUTTA = N2 normally.
ILE	Axial plane containing the damper leading edge. A value of 0 indicates no damper.
ITE	Axial plane containing the damper trailing edge. A value of 0 indicates no damper.
IDL	Radial grid line below damper, see Figure 16. If no damper then IDL = 1.
IDH	Radial grid line above damper, see Figure 16. If no damper then IDH = NR.
IFCL	IFCL=0 gives non-conservation law form equations, see equation 17. IFCF=1 gives full conservation law form, see equation 18.
IROT	If IROT=0 the fully unsteady equation sets, equation 17 or 18, are used. When IROT=1 a pseudo-unsteady equation set is used in which the energy equation is replaced with a constant rothalpy assumption.
GAMMA	Ratio of gas specific heats, usually 1.4.

W	Blade row angular rotation speed parameter equal to (Wr_{tip}/a_o). is rotation speed in radians per second, r_{tip} is for upstream tip radius (reference length for nondimensional lengths), a_o is far upstream stagnation speed of sound on tip streamline (reference velocity for nondimensional velocities).
CAPPA	Artificial viscosity parameter, usually equal to 0.5. A value of 0.1 would be very low damping while a value of 1.0 would be high damping.
PDOWN	The static pressure to be set on the last axial grid point at the hub radius. This pressure, $(P/\rho_o a_o{}^2)$, controls the blade row pressure ratio.
INOPT	INOPT=1 corresponds to inflow boundary condition option 1 in which the user specifies the upstream total pressure and temperature. INOPT=2 corresponds to inflow boundary condition option 2 in which the user specifies upstream total temperature and the values of the J_r^+ characteristic (see inlet B.C. discussion).
NUTH	Number of radial positions and absolute tangential velocity pairs which specify inlet tangential velocity as a function of radius. If NUTH=1, a constant value of UTHIN is produced and the input value of RUTH is ignored. NUTH must be ≤ 20.
RUTH, UTHIN	Radial position and absolute tangential velocity theta averaged. UTHIN = U_Θ/a_o and RUTU is the scaled radius, RUTH = R/R_{ref}.
NTT	Number of radial positions and total temperature pairs which specify inlet absolute total temperature as a function of radius. If NTT=1, a constant value of TTIN is produced and the input value of RTT is ignored. NTT must be $\leq$ 20.
RTT, TTIN	Radial position and absolute total temperature, theta averaged. TTIN is the ratio between the local total temperature and the reference temperature. The reference temperature is defined by $a_o = \sqrt{\gamma RT_o}$ and RTT is the scaled radius, RTT = R/R_{ref}.
NPT	Number of radial position and total pressure pairs which specify inlet absolute total pressure as a function of radius. If NPT=1, constant value of PTIN(J_r^+) is produced and the input value of RPT is ignored. NPT must be $\leq$20.

RPT, PTIN or RPT, JRIN	Radial position and absolute total pressure, theta averaged. PTIN is the ratio between the local total pressure and the reference stagnation pressure. $P_{t\,ref} = 1/\gamma$ and RPT = R/R_{ref}. When INOPT = 2, J_r^+ values are input instead of PTIN.
UPMACH	Far upstream uniform absolute meridional Mach number. Used only when initial conditions are generated by BLADE3D.
DT	Scaled time step to be used. If DT = 0.0 then time step is selected by program. See special instruction for rules for selecting DT.
NSTEP	Number of split operator cycles to be run. Several hundred operator cycles are usually required for a solution. Each cycle advances the solution several time steps. Solution is usually run only a few hundred cycles at a time to provide a restart capability.
IBEG	If IBEG = 1, a starting solution is generated.
NOR(I,J)	The MacCormack operator sequence to be run is stored in a two-dimensional array, NOR(10,3). Each row specifies an operator (X direction, Θ direction or R direction), the number of times each operation is to be executed and the time step multiple to be used. The entire operator sequence is executed NSTEP times.
IOP J = 1	The individual codes associated with each row are: Operator Code 1→X operator, 2→Θ operator and 3→R operator
IML J = 2	Time step multiple
IEX J = 3	Execution time multiple
	See special instructions and input card format sheet for more information about operator sequence.
NP1	Number of different sets of solution matrix information to be printed before operator sequence is begun.
CODE(NP1)	Determines type of printed solution variables. See special instructions for definition of allowed values.
JST(NP1)	First axial station to be included in printed information.
JEND(NP1)	Last axial station to be included in printed information.

LST(NP1)	First radial station to be included in printed information.
LEND(NP1)	Last radial station to be included in printed information.
NP2	Number of different sets of solution matrix information to be printed during operator sequence. If NP2 = 0, no intermediate results are printed.
NTIMES	Solution matrix is printed before the first operator sequence, after NSTEP sequences, and after every NTIMES sequence during the solution integration. NTIMES = 0 gives no intermediate printed results.
CODE(NP2)	Determines type of printed solution variables. See special instructions for definition of allowed values.
NST(NP2)	First axial station to be included in printed information.
JEND(NP2)	Last axial station to be included in printed information.
LST(NP2)	First radial station to be included in printed information.
LEND(NP2)	Last radial station to be included in printed information.
NP 3	Number of different sets of solution matrix information to be printed after operator sequence is completed.
CODE(NP3)	Determines type of printed solution variables. See special instructions for definition of allowed values.
JST(NP3)	First axial station to be included in printed information.
JEND(NP3)	Last axial station to be included in printed information.
LST(NP3)	First radial station to be included in printed information.
LEND(NP3)	Last radial station to be included in printed information.

Special Instructions for BLADE3D Input

1. DT is the non-dimensional integration time step. DT = $[(\delta ta_o)/(r_{ref})]$. The maximum DT in the absence of artificial damping or shock waves is given by equations 53, 54 and 55 and is printed out with each execution of matrix print routine. This maximum value must be reduced by approximately 40% for calculations with strong shocks. The suggested maximum value of DT is printed at the end of each code run.

2. The sequence of MacCormack split operators to be run must be determined for each case using the principle that $(DT)_x$, $(DT)_R$ and $(DT)_\Theta$ should be as close to the maximum allowed value while maintaining a symmetric sequence, as described by MacCormack.[2] See also equation 51.

Denoting the operators as $L_x(DT_x)$, $L_\Theta\ (DT_\Theta)$, $L_R(DT_R)$, then a simple sequence may be written as:

$$\bar{U}_j^{n+2} = [L_x(DT_x)L_\Theta(DT_\Theta)L_R(DT_R)L_\Theta(DT_\Theta)L_x(DT_x)]\bar{U}_j^n$$

which advances the solution from time level n to level n + 2. This sequence assumes $(DT_x)_{max} \approx (DT_\Theta)_{max}$ and $(DT_x)_{max} \approx 0.5(DT_R)_{max}$. A more typical sequence for transonic compressors arises when

$$(DT_R)_{max} \approx 10\ (DT_\Theta)_{max} \approx 20(DT_x)_{max}\ .$$

A suitable, but non-unique, sequence for this case would be:

$$\bar{U}_j^{n+20} = [10\ L_x(DT_x),\ 5L_\Theta(2DT_\Theta),\ L_R(20DT_R),\ 5L_\Theta(2DT_\Theta),\ 10L_x(DT_x)]\bar{U}_j^n$$

In general an operator is described by three parameters: the base time step (DT), a time step multiple (1, 2 or 20 above), and an execution multiple (10, 5 or 1 above).

The full operator sequence is stored in NOR(I,J) which for above example would appear as:

Operator Number	I = 1 Operator Key	I = 2 Time Step Multiplier	I = 3 Execution Multiple
J = 1	1	1	10
J = 2	2	2	5
J = 3	3	20	1
J = 4	2	2	5
J = 5	1	1	10

The operator keys are $1 \rightarrow L_x$, $2 \rightarrow L_\Theta$, $3 \rightarrow L_R$ and the maximum number of operators in a sequence is 10.

4. The value of CODE(I) determines the solution variable to be printed. The allowed values are:

Value	Printed Variables
1	Conservation variables ($r\rho$, $r\rho u_r$, $r\rho u_\theta$, $r\rho u_z$, $r\rho E_t$)
2	Physical variables (ρ, u_r, u_θ, u_z, E_t)
3	Physical variables in coordinate system rotating with blade row (ρ, M_r, $M_{\theta_{rel}}$, M_z, P)
4	Physical variables in coordinate system rotating with blade row (P_t, M_r, $M_{\theta_{rel}}$, M_z, T_t)
5	Physical variables in laboratory coordinate system (P_t, M_r, M_θ, M_z, T_t)

In addition, when codes 4 and 5 are selected, a summary of mass-flow-weighted axisymmetric variables is presented.

5. All variables allocated 5 columns in Table 4.2 are integer variables and must be right justified. All variables allocated 10 columns are real variables and should have decimal point included.

Table 4.2. Input Card Format for BLADE3D

1	6	11	16	21	26	31	36	41	46	51	56	61	66	71	76
TITLE															
NBL															
NX	NTH	NR													
N1	N2	KUTTA	ILE	ITE											
IDL	IDH	IFCL	IROT												
GAMMA		W		CAPPA		PDOWN									
INOPT															
NUTH						Inlet Swirl Velocity									
RUTH(1)		UTHIN(1)													
⋮		⋮													
RUTH(NUTH)		UTHIN(NUTH)													
NTT						Inlet Stagnation Temperature									
RTT(1)		TTIN(1)													
⋮		⋮													
RTT(NTT)		TTIN(NTT)													
NPT						Inlet Stagnation Pressure or J_r^+ characteristic values									
RPT(1)		PTIN(1)													
⋮		⋮													
RPT(NPT)		PTIN(NPT)													
UPMACH															

DT	NSTEP	IBEG

*** UP TO 10 CARDS DESCRIBING

*** OPERATOR SEQUENCE ARE NEXT.

*** SEQUENCE IS TERMINATED BY A BLANK

*** CARD. SEQUENCE IS STORED IN NOR(I,J)

IOP	IML	IEX

UP TO 9 MORE DESCRIPTOR CARDS

BLANK CARD

NP1

CODE	JST	JEND	LST	LEND

***NP1-1 MORE CARDS DESCRIBING TYPE

*** OF PRINTED OUTPUT DESIRED BEFORE THE OPERATOR SEQUENCE

NP2	NTIMES

CODE	JST	JEND	LST	LEND

*** NP2-1 MORE CARDS DESCRIBING TYPE

*** OF PRINTED OUTPUT DESIRED AFTER THE OPERATOR SEQUENCE

NP3

CODE	JST	JEND	LST	LEND

*** NP3-1 MORE CARDS DESCRIBING TYPE

*** OF PRINTED OUTPUT DESIRED DURING THE OPERATOR SEQUENCE

Data Files Used for MESH3D, BLADE3D and GRAPH3D

Several data files are used by MESH3D, BLADE3D and GRAPH3D as input files, scratch files, and permanent storage files. These files and their characteristics are shown below.

Table 4.3. Data Files for MESH3D

FORTRAN Unit Number	Type of File	Comments
1	Scratch UNFORMATTED	Used by BLDT
2	Permanent UNFORMATTED	Used by RGRID, INSEC, GETTHA, CALDR, CALDER for scratch file and BLDT for creating file TGEOM to be used by BLADE3D
3	Scratch UNFORMATTED	Used by XRGRID, RGRID, BUILD
4	Permanent UNFORMATTED	Used by GETTHA, CALDR, CALDER, BLDT as scratch file and BUILD for creating file GEOM (to be used by MESH3D)
5	Input Data FORMATTED	All Input Data in this file. Used by MESH3D, BLADE3D, XRGRID, FILL, RMID
6	Output Data FORMATTED	Message and Error file used by all routines
8	Scratch UNFORMATTED	Used by INSEC, GETTHA, CALDR, CALDER
9	Scratch UNFORMATTED	Used by CALDER, BLDT
12	Permanent UNFORMATTED	Used by SVGRID to create file SVSAVE which contains r,θ,z coordinates of grid nodes
IWR	Output Data FORMATTED	Used by all routines as an optional bulk output file

Table 4.4 Data Files for BLADE3D

FORTRAN Unit Number	Type of File	Comments
1	Permanent UNFORMATTED	Initial solution matrix storage used by START
2	Permanent UNFORMATTED	Blade geometry for MESH3D, file TGEOM used by OPEN
3	Permanent UNFORMATTED	Axisymmetric geometry file from MESH3D, file GEOM used by OPEN
5	Input Data FORMATTED	All input data in this file, used by MAIN program and MTHREE
6	Output Data FORMATTED	Used by all routines for Printed Output
7	Permanent UNFORMATTED	Final solution matrix written by CLOSE

Table 4.5 Data Files for GRAPH3D

FORTRAN Unit Number	Type of File	Comments
1	Permanent UNFORMATTED	Solution Matrix File from BLADE3D unit number 7
2	Permanent UNFORMATTED	File TGEOM from MESH3D unit number 2
3	Permanent UNFORMATTED	File GEOM from MESH3D unit number 4
4	Permanent UNFORMATTED	File SVSAVE from MESH3D unit number 12
5	Permanent FORMATTED	Grid Numbering Information from BLADE3D unit number 5
6	Output Data FORMATTED	Used for Printed Output
7	Permanent UNFORMATTED	Solution Matrix Storage for Entire Finite Difference Grid
8	Permanent UNFORMATTED	Solution Matrix Storage for S1-S2 Stream Surfaces

Description of Printed Output for MESH3D

The printed output from MESH3D consists of a message and error file which reproduces the axial grid numbering information, a running execution sequence log for major subroutines, and a bulk output file. This message file is of critical importance in locating input or logical errors in MESH3D operation. A sample message file is shown in Figure 24. The initial portion reproduces the axial grid input data, and if any parameter is outside of allowed ranges an error message will be printed in this file. Program execution terminates when an input error is found. After successful completion of each principal subroutine a message is printed. This run file also contains a set of warning messages from subroutine CALT which are generated when the blade row geometric input data must be extrapolated rather than interpolated. Printed values of blade row normal vectors and curvatures should be closely monitored to insure that the linear extrapolation performed represents the blade row geometry adequately. No further warning or error messages are normally produced by CALT, BLDT or BUILD.

The bulk output from MESH3D reproduces the geometric input data and the calculated results from MESH3D. Figure 25 illustrates the raw data input check for the hub and tip casing geometry, leading and trailing edge geometry, and damper geometry. This data is the "as read" geometry for each input data class. Figure 26 illustrates the scaled data smoothness check for XRGRID input. This data includes the scaled axial and radial coordinates and the first and second derivatives of radial position with respect to axial position. Small errors in these input quantities are usually quite apparent because of their influence on the second derivatives. The principal output from subroutine XRGRID is illustrated in Figure 27 and consists of the axial and radial positions of the x and r coordinate line intersections in physical space for each axial grid station. The calculated metric derivatives $(\partial X/\partial z)$, $(\partial X/\partial r)$, $(\partial R/\partial r)$ and $(\partial R/\partial z)$ are also shown.

Bulk data output for subroutine CALT is the scaled blade row geometry as well as first and second derivatives of theta position with axial position for both pressure surface and suction surface. Best results from the calculation program BLADE3D are obtained when the first and second derivatives are smooth. When "jumps" in either derivative occur special care should be taken to insure that the input data accurately represents the blade design intent. This bulk output is illustrated in Figure 28. The blade row normal vectors and radii of curvatures calculated from the input geometric data are illustrated in Figure 29. This data is presented for each axial grid station inside the blade row. Special attention should be paid to the calculated radii of curvatures since small input errors greatly affect their value. This output is generated by subroutine BLDT.

The final bulk output from MESH3D is generated by subroutine BUILD and consists of the hub and tip slope and radius of curvature and the value of the transformation Jacobian, equation 23, for each axial and radial station. This output is illustrated in Figure 30.

Printed Output for BLADE3D

The printed output from BLADE3D begins by reproducing the input card file directing a particular solution pass. Figure 31 illustrates output from this first section. Particular attention should be paid to the printed MacCormack Operator sequence to insure that it is the one intended and that it is a symmetric sequence. At the user selected axial and radial node points, the solution matrix will be displayed for all theta nodes. Figure 32 illustrates this output section. The content of this printed output, variables and coordinate system, is determined by options selected in the card input file for BLADE3D. If print option 4 or 5 is selected, then conventional theta averaged variables (meridional Mach numbers, total and pressure and temperature ratios, etc.) are calculated and displayed. This output is illustrated in Figure 33. Definitions of printed variables are given in special instruction number 4 for BLADE3D.

In addition to the user selected printed output, a substantial amount of information is printed during the operator sequence in order to document the history of a particular calculation. This information is printed after each 100 operator sequences and consists of printer/plotter plots of mass flow rate vs axial grid plane number, mid-span trailing edge static pressure vs operator sequence number and mid-span blade static pressure vs axial grid plane number. This information is the best guide to solution convergence rate and should be monitored closely. Examples of these three informational plots are shown in Figures 34, 35 and 36.

Output Description for GRAPH3D

The printed output from GRAPH3D consists of printer/plotter plots of blade surface MACH number and static pressure for each S1 surface and plots of S2 streamsurface positions for the pressure surface, mid-channel surface and the suction surface. Examples of the S1 and S2 surface plots are given in Figures 37 and 38. In addition, a summary of S1 streamsurface-theta averaged flow variables is presented for the grid planes corresponding to the blade leading edge and the blade trailing edge. An example of this output is shown in Figure 39.

Both user defined solution matrix storage files have the same format which is specified in Table 4.6. Each FORTRAN record corresponds to one grid node point and contains the radial, tangential and axial grid index number, the non-dimensional radial, tangential and axial positions, the nondimensional conservation variables ($r\rho$, $r\rho u_r$, $r\rho u_\theta$, $r\rho u_z$, rE_t) and the nondimensional physical flow variables (P_t, M_r, M_θ, M_z, T_t). The finite difference grid output file contains all axial plane numbers 1 through NX. The S1-S2 streamsurface file contains only axial plane numbers N1 through N2.

EXAMPLE CALCULATION

The computer codes described in the previous section were used to predict the flow through a low aspect ratio, transonic compressor rotor designed by Urasek [22] of NASA LEWIS RESEARCH CENTER. This rotor has an inlet hub to tip ratio of 0.375, an aspect ratio of 1.56 and an inlet relative Mach number of 1.38. In conventional steady state testing at NASA LeRC, the rotor was found to have a peak adiabatic efficiency of 90.6%, a total pressure ratio of 1.686 and a mass flow rate of 34.03 Kg/sec. In Blowdown Tunnel testing at MIT [23], the rotor was found to have an adiabatic efficiency of 89.5%, a total pressure ratio of 1.677 and a mass flow rate of 33.3 Kg/sec.

The calculated operating point for the sample, inviscid calculation was set such that the predicted passage shock pattern approximated that determined in MIT BLOWDOWN COMPRESSOR TUNNEL flow visualization testing [24]. It was found to be impossible to match the mid-span bow-shock shape, the shape of tip wall static signature and the level of the tip wall static measurements. Predicted overall performance parameters were found to be a mass flow rate of 35.6 Kg/sec, a total pressure ratio of 1.756 and an adiabatic efficiency of 94.2%. Having generally the same shock structure at a higher mass flow rate and total pressure ratio is consistent with the assumption of inviscid flow.

In order to verify that the calculated flow condition realistically represents the test rotor performance, comparisons between calculated and measured theta averaged performance is useful. A comparison of relative flow angle at the rotor trailing edge is shown in Figure 40 along with the blade metal angles. For $R/R_{ref} < 0.90$, the inviscid predictions follow the expected variation with respect to the metal angles and match the experimental values. For $R/R_{ref} > 0.90$, the experimental values show considerably less turning than would be expected either from deviation angle correlations or the inviscid predictions. The observed flow angle variation is difficult to explain on the basis of purely inviscid fluid phenomena, since as is shown in Figures 41 and 42, the experimental rotor leading edge meridional Mach numbers are nearly identical with the predicted values while the experimental total temperature ratios are larger than the predicted values. These phenomena suggest that either viscous phenomena such as profile boundary layer separation or viscous linked phenomena such as boundary layer flow migration significantly affect the flow for $R/R_{ref} > 0.90$.

A comparison of the theta averaged rotor total pressure ratios is shown in Figure 43. The inviscid prediction and the NASA LeRC steady state measurements compare well over the entire span, while neither compares well with the high response total pressure measurements made in the MIT BLOWDOWN COMPRESSOR Tunnel. The origin of the high total pressure area, $R/R_{ref} > 0.70$, in the MIT data, has not yet been explained.

Measurements of the blade-to-blade variation in static density have been reported in reference [24]. These studies have shown a rotor shock system consisting of a moderate strength bow shock at mid-span, a weak strength bow shock near the three-quarter span radius and of a secondary weak passage shock near the tip section. These characteristics are well illustrated in three contour plots, figures 44, 45 and 46, which show the computed relative Mach number on blade-to-blade running surfaces. These surfaces have the constant radii of R/R_{ref} = 0.80, 0.90 and 0.95. At an R/R_{ref} of 0.80 a strong oblique bow shock is predicted with the flow remaining subsonic nearly everywhere downstream of the shock. At an R/R_{ref} of 0.90 a weak oblique bow shock is predicted, but the flow becomes supersonic in a small region near the trailing edge. At an R/R_{ref} of 0.95, a weak bow shock is predicted with the flow remaining at supersonic across the entire passage. The supersonic region is terminated by a weak compression or shock and the flow is subsonic everywhere downstream of the trailing edge.

To clarify the predicted shock structure, relative Mach number contour plots for the pressure and suction surface are shown in figures 47 and 48. Figure 47 shows the flow to be subsonic over nearly the entire span. The supersonic flow portion is terminated by a weak shock. The suction surface flow pattern is much more complex as shown in figure 48. The flow is supersonic over a large fraction of the blade surface with two different passage shocks evident. The suction surface shock structure is sketched in figure 49 which illustrates that the first passage shock, really the bow shock, is a strong oblique shock near mid-span and a weak oblique shock near the tip section. The two shock families merge near the three-quarter span point where the shock turning angles are the same for both families.

The intra-blade flow visualization technique does not allow resolution of leading edge flow features for $R/R_{ref} > 0.85$ and high response wall static measurements must be used to experimentally probe the shock structure near the tip radius. Reference [23] presents wall static measurements at the axial locations illustrated in Figure 50, and sample static pressure traces are reproduced in Figures 51, 52 and 53. The predicted wall static pressures are also compared to 5 cycle ensemble averages of these data in Figures 54, 55 and 56. At the upstream measurement ports 2.0 and 56, the shape of the computed wall static pressure trace closely follows the measured 5 cycle average, but the shock pressure rise is well under-predicted. At the mid-chord measurement port 2.5, the shape of the pressure trace is well predicted, but the mid-passage pressure level is predicted to be too high.

In order to clarify the comparison of predicted and measured wall static pressures, the port 56 measurement is compared to the computed leading edge pressure in Figure 57. This figure shows that the correct bow shock pressure rise is predicted, but the predicted bow shock appears at the wrong axial position. Since the predicted shock pressure rise is consistent with the blade leading edge wedge angle, it must be concluded that the tip bow shock is detached in the experiment. The most likely explanation for this difference is that the experimental compressor has a tip "end-bend" or local over-twist to accommodate a tip end-wall boundary layer. The end-wall boundary layer is absent in the MIT test configuration.

To complete the documentation of the sample solution, blade surface static pressures and blade surface Mach number distributions along each radial grid plane are shown in Figures 58 through 87. Figures 58 through 72 illustrate the static pressure, and Figures 73 through 87 illustrate the relative coordinate system total Mach number. The nominal upstream sonic line occurs at radial plane number 9, but supersonic flow extends inward to radial plane number 5. These figures illustrate the transition from subsonic flow to supersonic flow; the inviscid calculation leading edge resolution in subsonic flow, Figures 59 and 73; and the shock resolution, Figure 87. These figures show that the compromises in leading edge resolution have not greatly degraded the solution.

Table 4.6. Format of Solution Matrix Storage File Produced by GRAPH3D

RECORD NUMBER	TANGENTIAL STATION NUMBERS 3 INTEGER VALUES			RADIAL, TANGENTIAL, AXIAL POSITIONS 3 FLOATING POINT VALUES	FLOW VARIABLES $r\rho$, $r\rho u_r$, $r\rho u_\theta$, $r\rho u_z$, $r\rho E$ 5 FLOATING POINT VALUES	FLOW VARIABLES, LABORATORY COORDINATES P_T, M_r, M_θ, M_z, T_t 5 FLOATING POINT VALUES
	ℓ	k	j			
1	1	1	1	0.3093, 0., -0.4880	0.270, 0., 0., 0.138, 0.493	0.714, 0., 0., 0.547, 1.00
2	1	2	1	0.3093, 0., -0.4880	same	same
⋮						
NTH	1	NTH	1	0.3093, 0., -0.4880	same	same
NTH + 1	2	1	1	0.3904, 0., -0.4790	0.337, 0., 0., 0.179, 0.614	0.714, 0., 0., 0.547, 1.0
⋮						
2NTH	2	NTH	1	0.3904, 0., -0.4790	same	same
⋮						
NTH * R	NR	NTH	1	1.0407, 0., -0.4180	0.909, 0., 0., 0.466, 1.658	0.714, 0., 0., 0.539, 0.99
1 + NTH * R	1	1	2	0.3801, 0., -0.4337	0.379, -0.10, 0.0, 0.18, 0.519	0.714, -0.035, 0., 0.612, 1.0
⋮						
2 * NTH * NR	NR	NTH	2	1.0408, 0., -0.3536	0.817, -0.006, 0.001, 0.442, 1.55	0.714, -0.015, 0.0, 0.546, 1.0
⋮						
NX * NTH * NR	NR	NTH	NX	.9796, 0.0, 0.8463	1.231, 0., 0.426, 0.631, 2.645	1.101, 0.0, 0.345, 0.479, 1.150

REFERENCES

1. MacCormack, R.W. and Warming, R.F.: "Survey of Computational Methods for Three Dimensional, Supersonic, Inviscid Flows with Shocks." AGARD Lecture Series No. 73, COMPUTATIONAL METHODS FOR INVISCID AND VISCOUS TWO-AND-THREE-DIMENSIONAL FLOW FIELDS, Feb. 1975.

2. MacCormack, R.W.: "Computational Efficiency Achieved by Time Splitting of Finite Difference Operators," AIAA Paper 72-154, 1972.

3. Salas, M.: "The Anatomy of Floating Shock Fitting," AIAA 2nd Computational Fluid Dynamics Conference, Hartford, CT, June 1975, pp 47-54.

4. Moretti, G.: "On the Matter of Shock Fitting," Proceedings of the 4th International Conference on Numerical Methods in Fluid Dynamics, Springer-Verlag, June, 1974.

5. Steger, J.L.: "Implicit Finite-Difference Simulation of Flow about Arbitrary Two-Dimensional Geometries," AIAA Journal, Vol 16, July 1978, pp 679-686.

6. Viviand, H.: "Conservative Forms of Gas Dynamic Equations," La Recherche Aerospatiale, No. 1, Jan. 1974, pp 65-68.

7. Merrington, G.L.: ARL Report/ME, No. 146.

8. Yanenko, N.N.: "The Method of Fractional Steps," Springer-Verlag, New York, 1971.

9. Lapidus, A.: "A Detached Shock Calculation by Second Order Finite Differences," J. of Comp. Phys., Vol. 2, 1967, pp 154-177.

10. Thompkins, W.T., and Epstein, A.H.: "A Comparison of the Computed and Experimental Three-Dimensional Flow in a Transonic Compressor Rotor," AIAA Paper 76-368, July 1976.

11. Roache, P.J.: "Computational Fluid Dynamics," Hermosa Publishers, Albuquerque, 1976.

12. Kreiss, H. and Oliyer, J.: "Methods for the Approximate Solution of Time Dependent Problems," Global Atmospheric Research Program Publication Series No. 10, 1973.

13. Abbett, M.: "Boundary Condition Computational Procedures for Inviscid Supersonic Steady Flow Field Computations," Aerotherm Corp., Mt. View, Calif, Final Report 71-41, 1971.

14. Thompkins, W.T. and Tong, S.S.: "Inverse or Design Calculations for Non-Potential Flow in Turbomachinery Blade Passages," ASME Paper 81-GT-78, March 1981.

15. Pulliam, T.H., Steger, J.L.: "Implicit Finite-Difference Simulations of Three-Dimensional Compressible Flow," AIAA Journal, Vol 18, No. 2, Feb. 1980, pp 159-167.

16. Salas, M.D. and Daywitt, J.: "Structure of the Conical Flowfield about External Axial Corners," AIAA Journal, Vol. 17, Jan. 1979, pp 41-47.

17. Kutler, P. and Shankar, V.: "Computation of the Inviscid Supersonic Flow Over an External Axial Corner," Proceedings of the 1976 Heat Transfer and Fluid Mechanics Institute, Davis, Calif., June 1976, pp 356-373.

18. Haymann-Haber, G. and Thompkins, W.T.: "Comparison of Experimental and Computational Shock Structure In a Transonic Compressor Rotor," J. of Eng. for Power, Vol. 103, Jan. 1981, pp 78-88.

19. Berenfeld, S.: "A Study of Boundary Conditions for Three Dimensional Transonic Compressor Rotors," SM Thesis, MIT, June 1979.

20. Rae, W.J. and Lordi, J.A.: "A Study of Inlet Conditions for Three Dimensional Compressor Flows," XE-6129-A-4, June 1978, Calsan Corporation, Buffalo, NY.

21. Griffin, M.D., Jones, E., Anderson, T.D.: "A Computational Fluid Dynamic Technique Valid at the Centerline for Non-Axisymmetric Problems in Cylindrical Coordinates," J. of Comp. Physics, Vol. 30, March 1979, pp 352.

22. Urasek, D. C., Gorrell, W.T., and Cannon, W.S.: "Performance of Two-Stage Fan Having Low-Aspect-Ratio, First Stage Rotor Blading," NASA Technical Paper 1493, 1978.

23. Ng, W.F.: "Detailed Time Resolved Measurement and Analysis of Unsteady Flow in a Transonic Compressor," MIT Gas Turbine and Plasma Dynamics Lab. Report No. 150, Aug. 1980.

24. Epstein, A.H., Ng, W.F. and Thompkins, W.T.: MIT Blowdown Test Report on NASA Low-Aspect-Ratio Transonic Compressor Stage," NASA Contractor Report, to be published

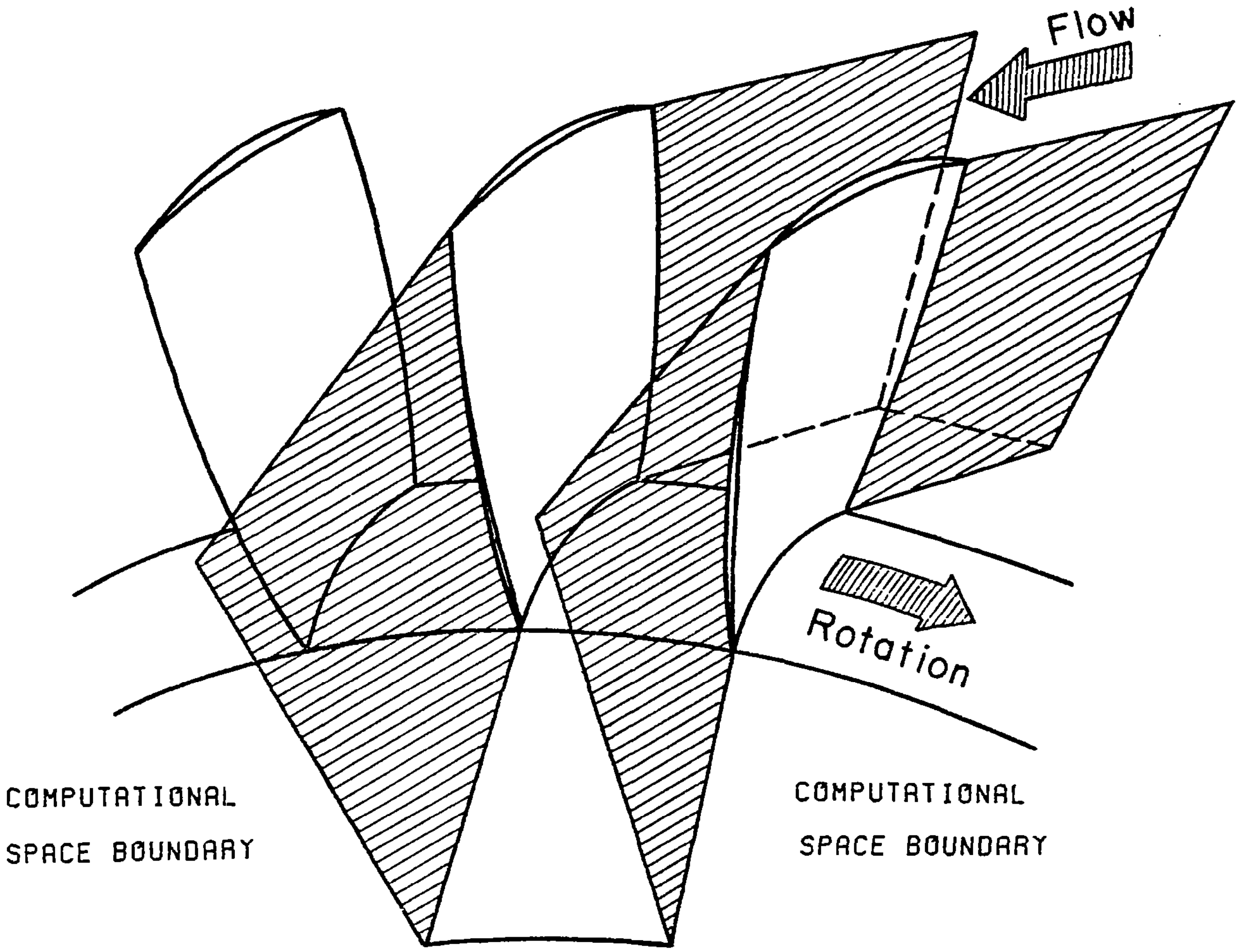

FIGURE 1. PHYSICAL SPACE VIEW OF SINGLE BLADE PASSAGE SHOWING COMPUTATIONAL DOMAIN

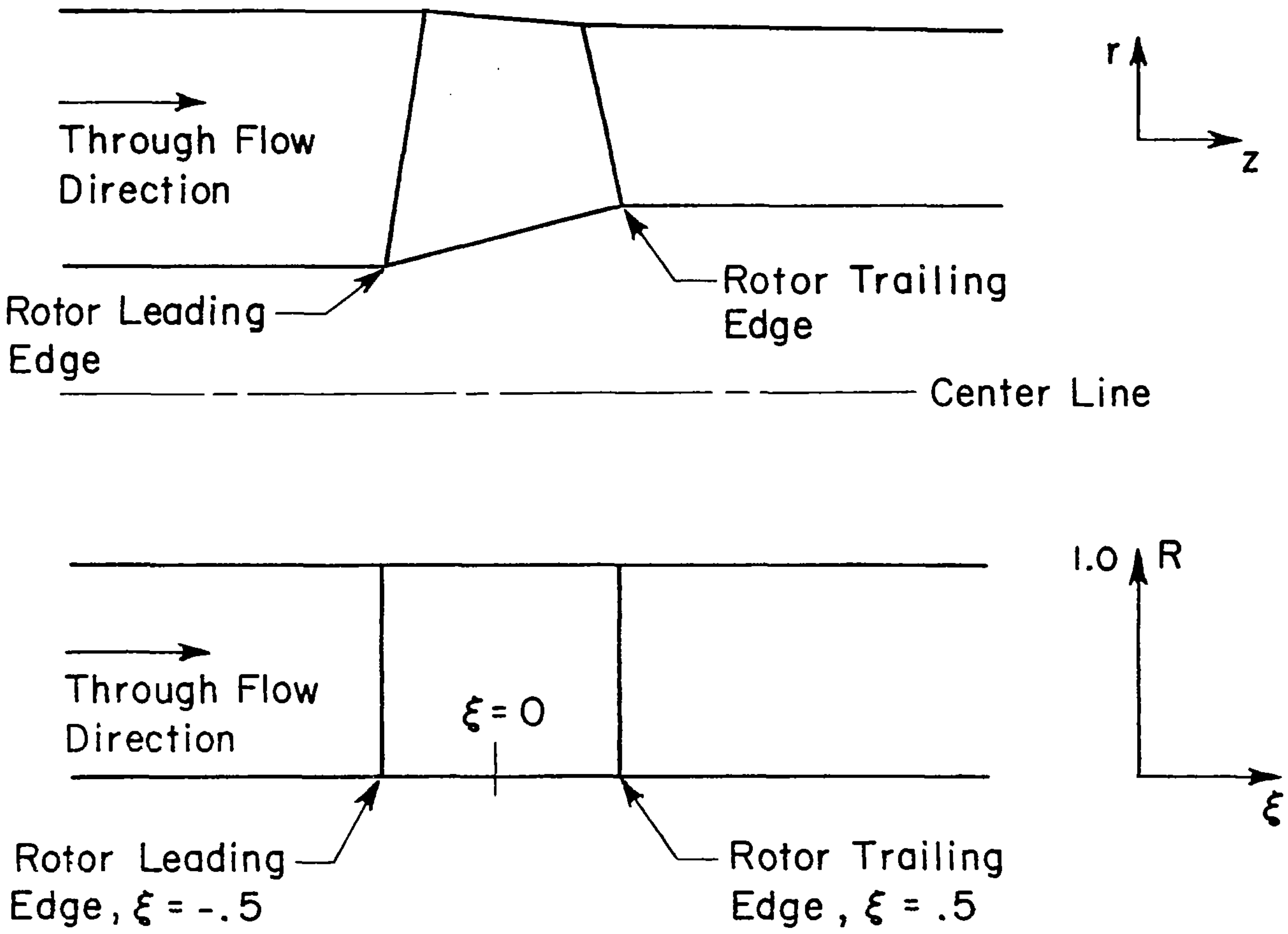

Mapping Function

$$R = \frac{r - r_{hub}}{r_{tip} - r_{hub}} \qquad \xi = \frac{z - z_{\ell e}}{z_{te} - z_{\ell e}} - 0.5$$

FIGURE 2 PLAN VIEW OF PHYSICAL SPACE AND FIRST COMPUTATIONAL DOMAIN

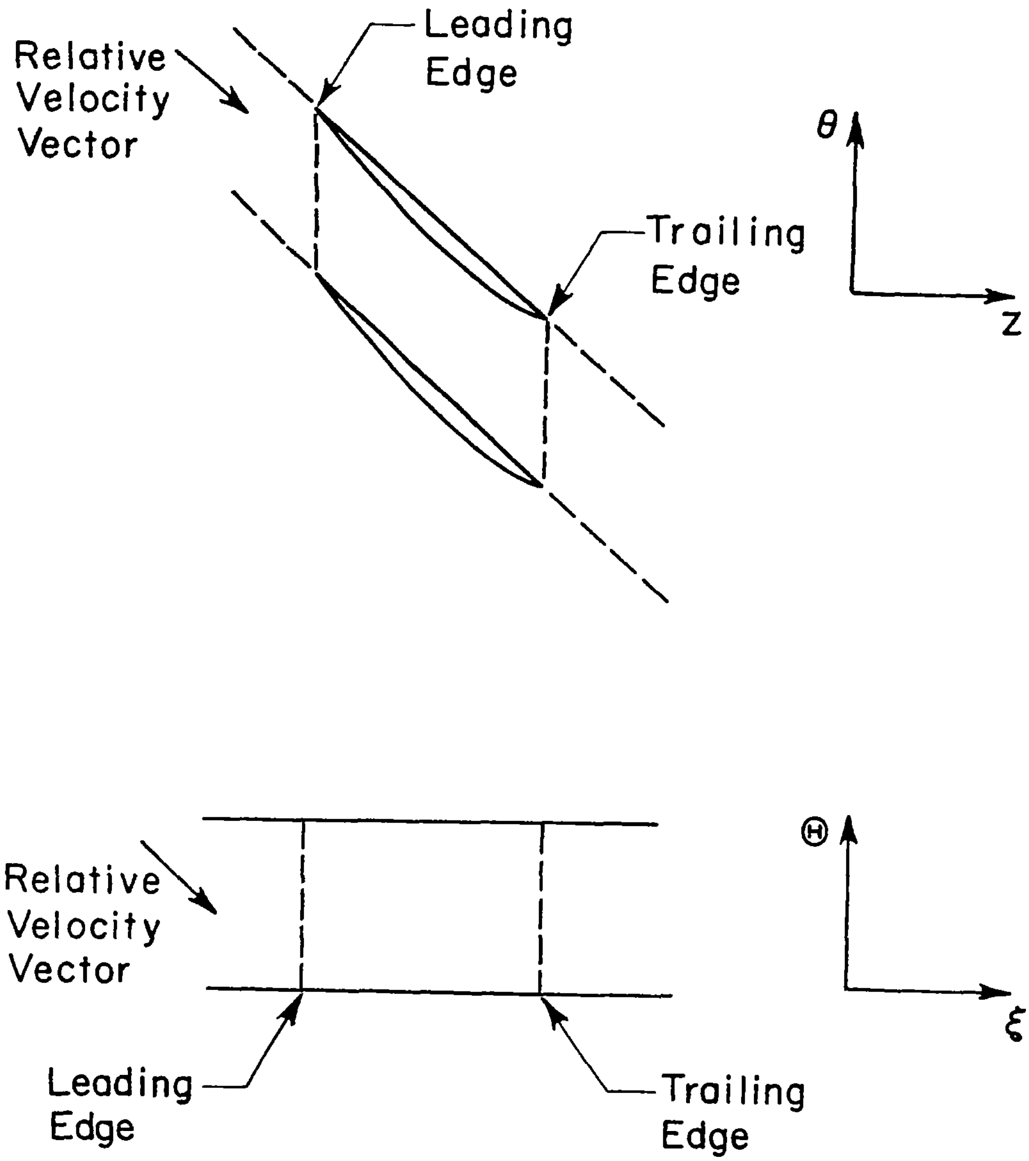

Mapping Function

$$\Theta = \frac{\theta - \theta_{ps}}{\theta_{ss} - \theta_{ps}}$$

FIGURE 3 BLADE TO BLADE VIEW OF PHYSICAL SPACE AND FIRST COMPUTATIONAL DOMAIN

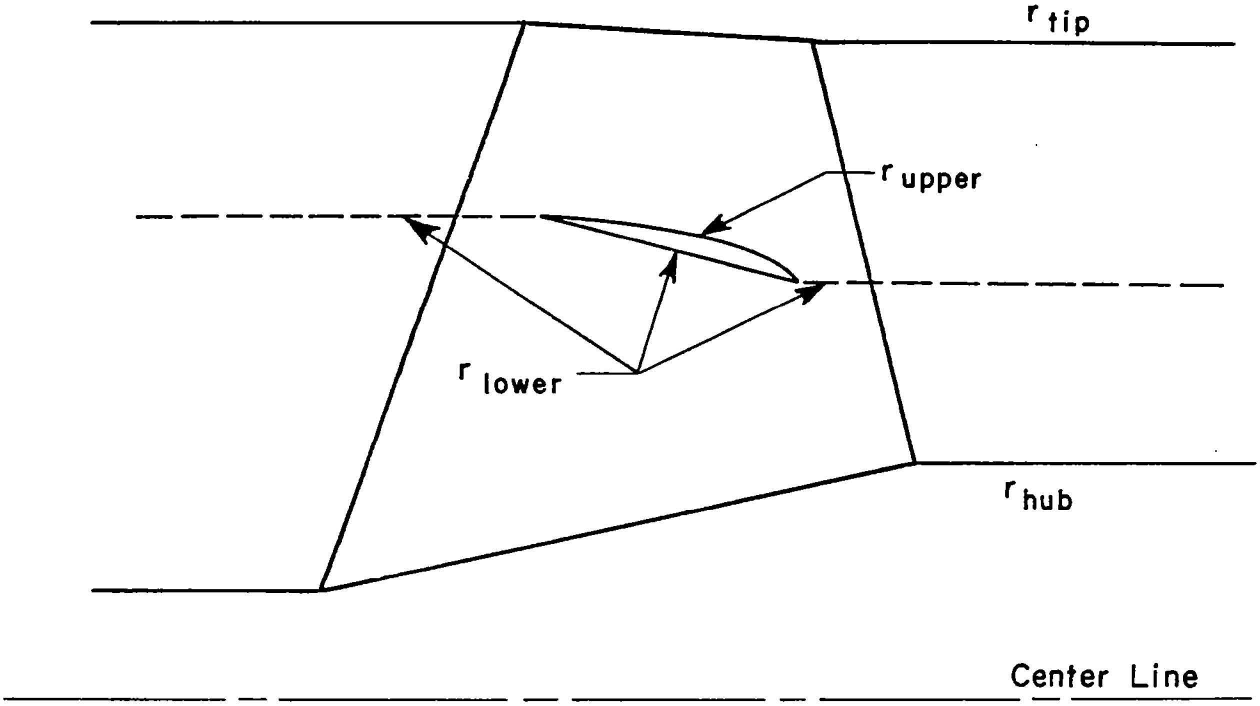

FIGURE 4 PLAN VIEW OF ROTOR GEOMETRY SHOWING PART-SPAN SHROUD

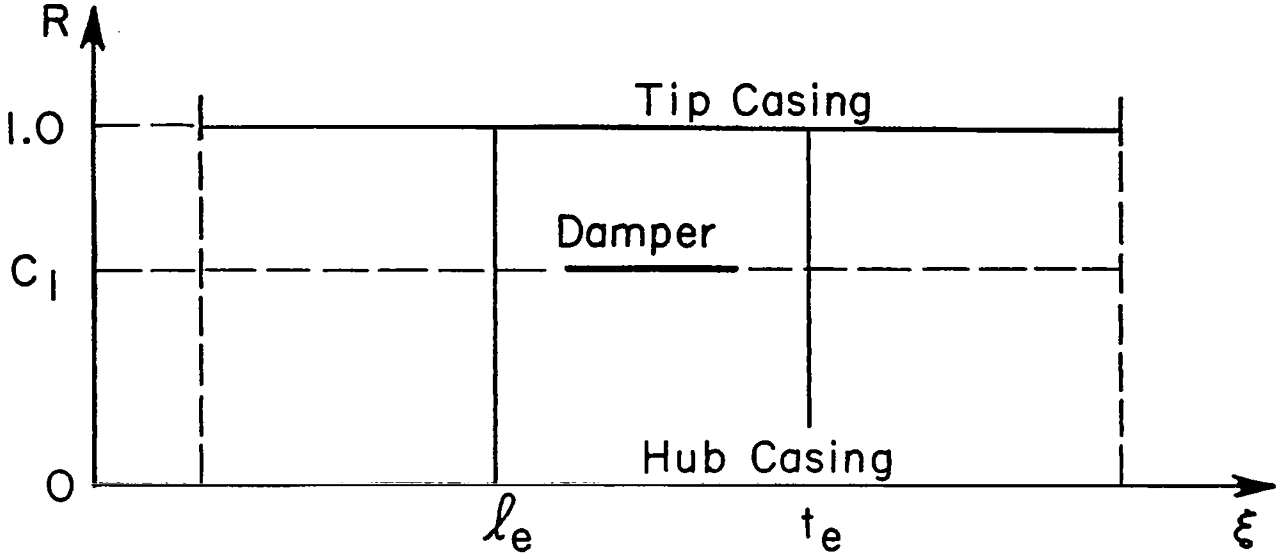

FIGURE 5 PLAN VIEW OF COMPUTATIONAL DOMAIN SHOWING PART-SPAN SHROUD

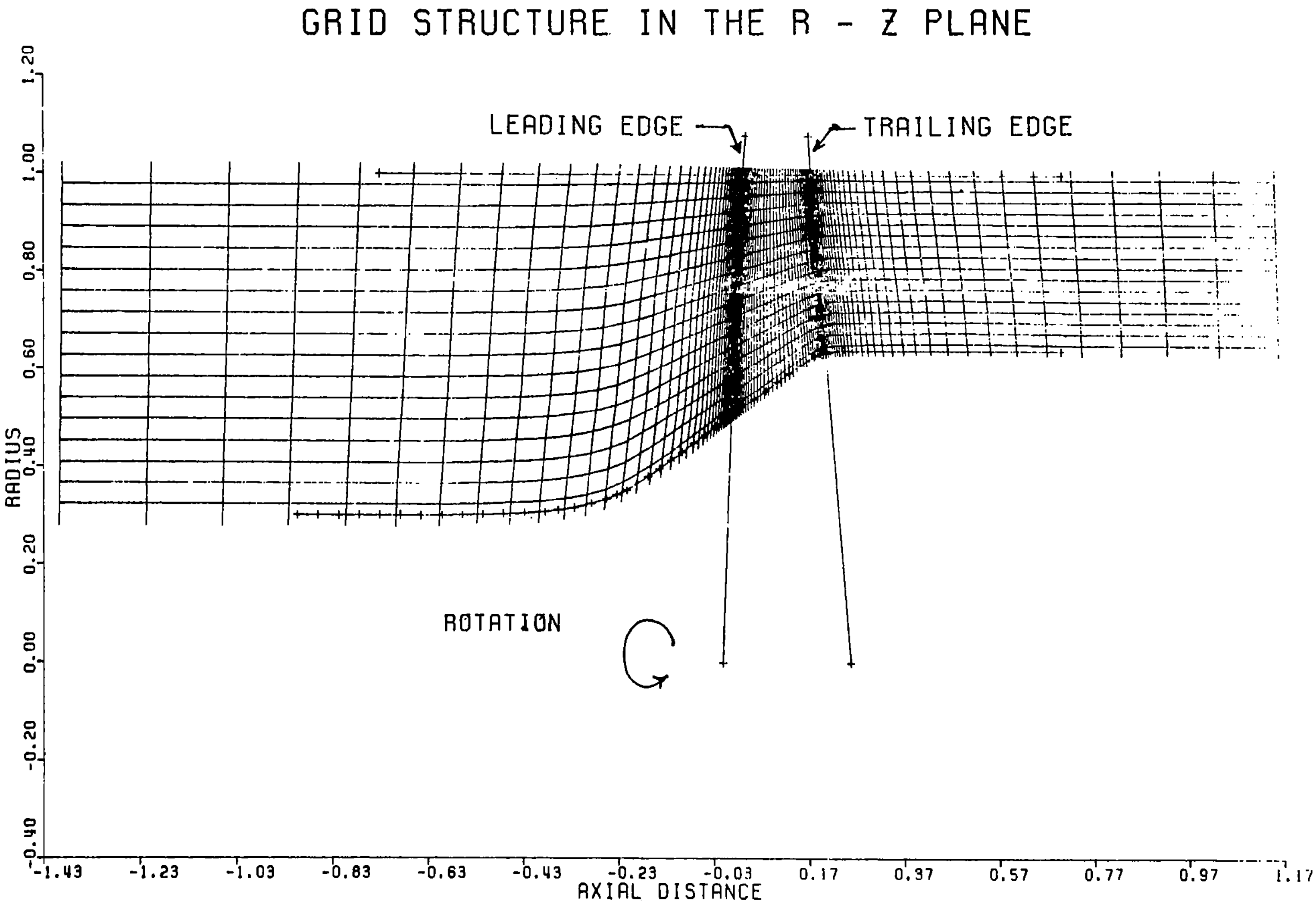
GRID STRUCTURE IN THE R - Z PLANE
LEADING EDGE
TRAILING EDGE
ROTATION
RADIUS
1.20
1.00
0.80
0.60
0.40
0.20
0.00
-0.20
-0.40
AXIAL DISTANCE
-1.43
-1.23
-1.03
-0.83
-0.63
-0.43
-0.23
-0.03
0.17
0.37
0.57
0.77
0.97
1.17

FIGURE 6

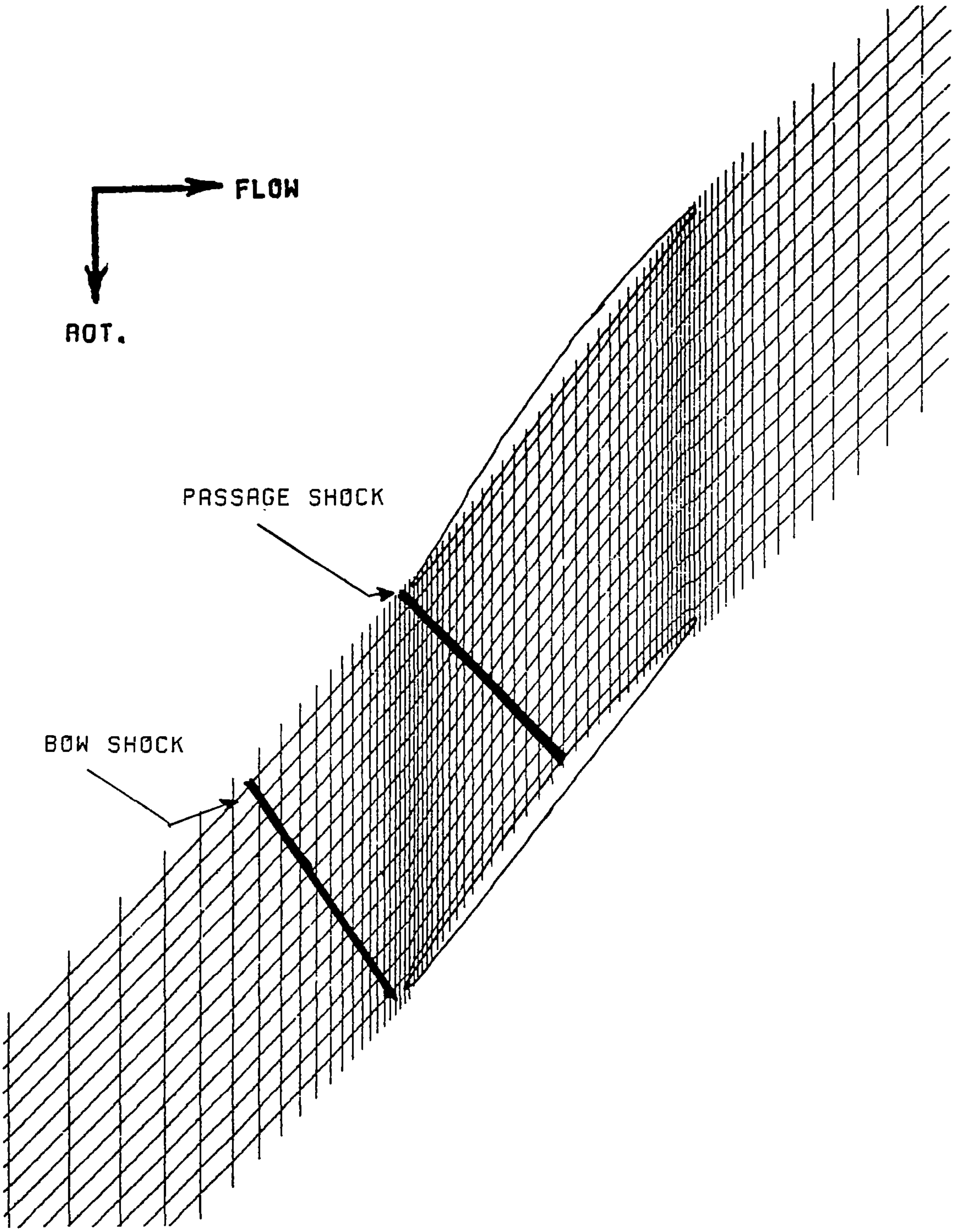

FIGURE 7 GRID STRUCTURE IN R - THETA PLANE

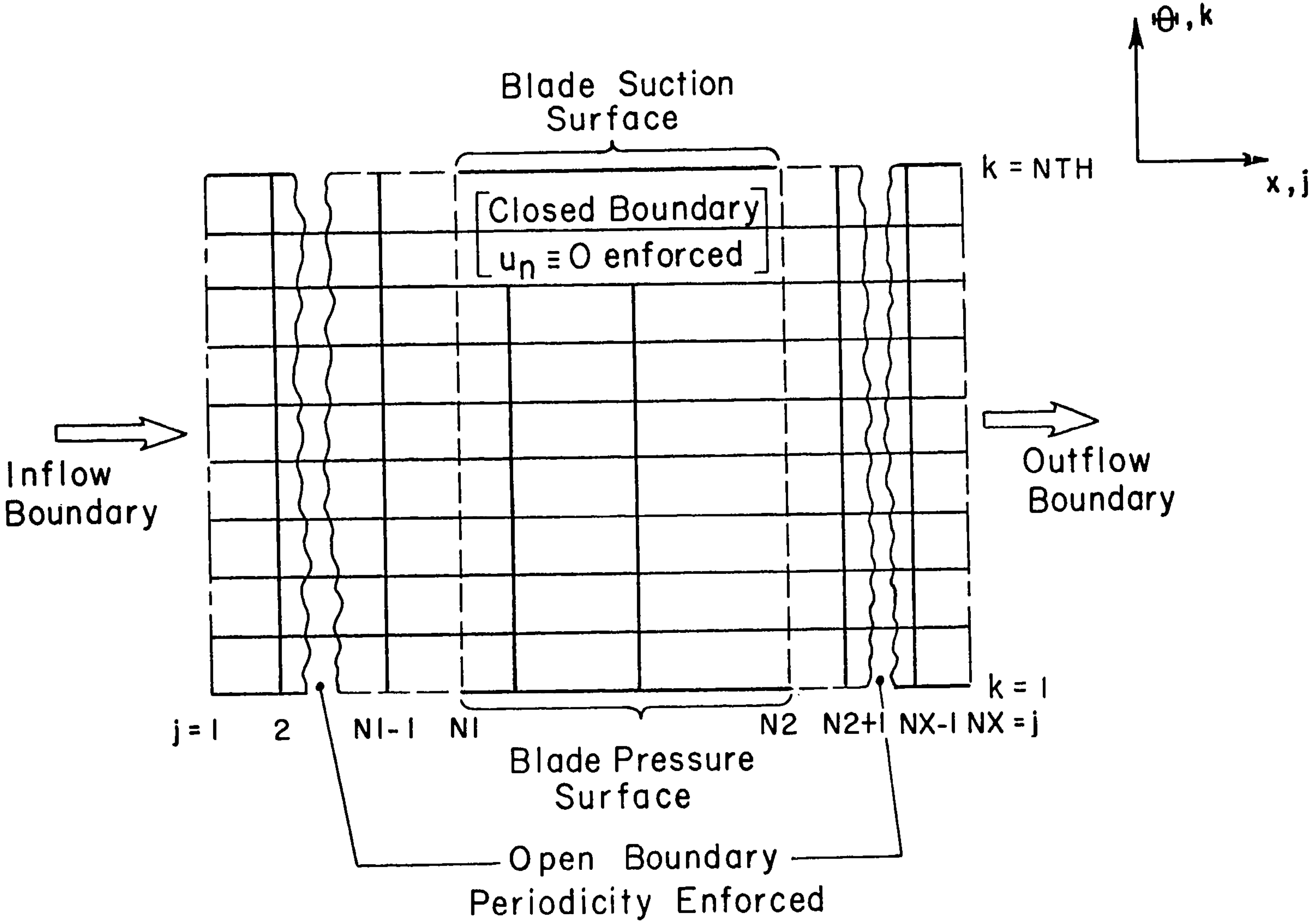

FIGURE 8 BLADE TO BLADE VIEW OF COMPUTATIONAL DOMAIN SHOWING DIFFERENT BOUNDARY TYPES

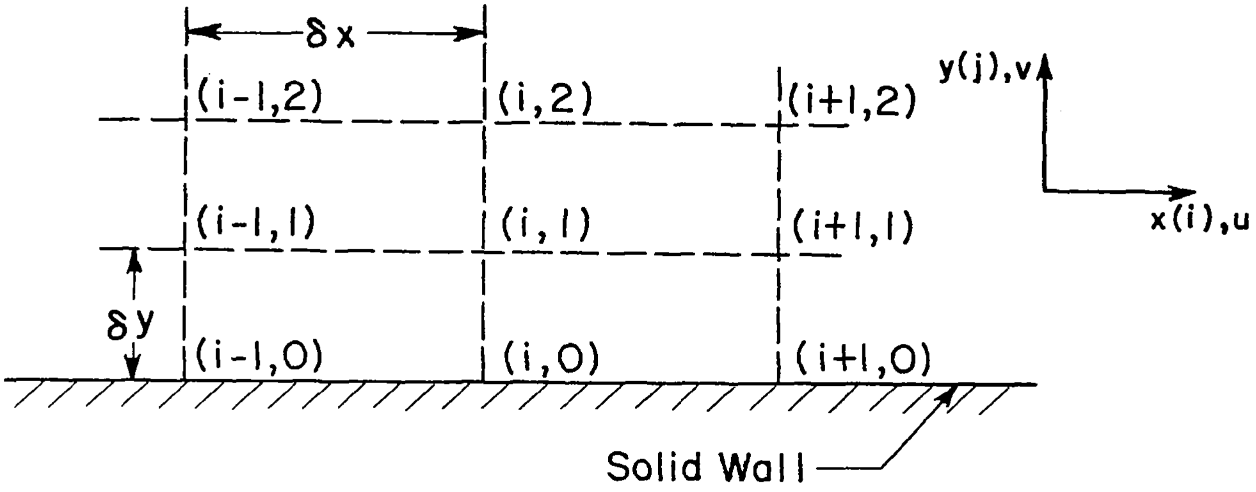

FIGURE 9 EXAMPLE GRID FOR CONTINUITY INTEGRATION

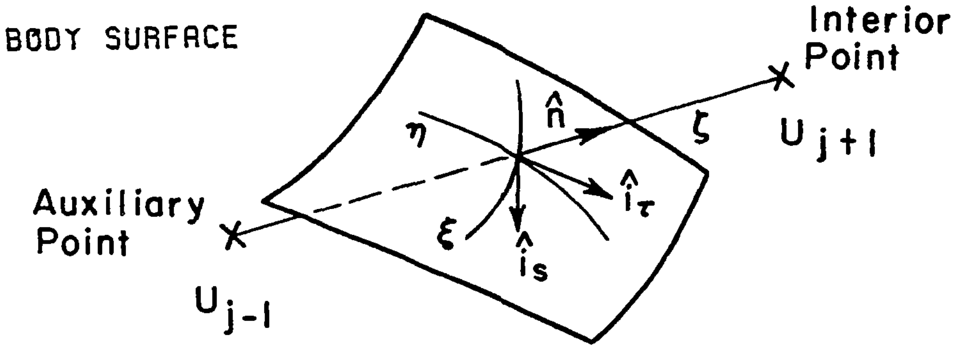

SURFACE NORMAL VECTOR

UNIT VECTOR TANGENT TO ξ COORDINATE LINE

UNIT VECTOR TANGENT TO η COORDINATE LINE

FIGURE 10 COORDINATE SYSTEM FOR WALL STATIC PRESSURE EVALUATION

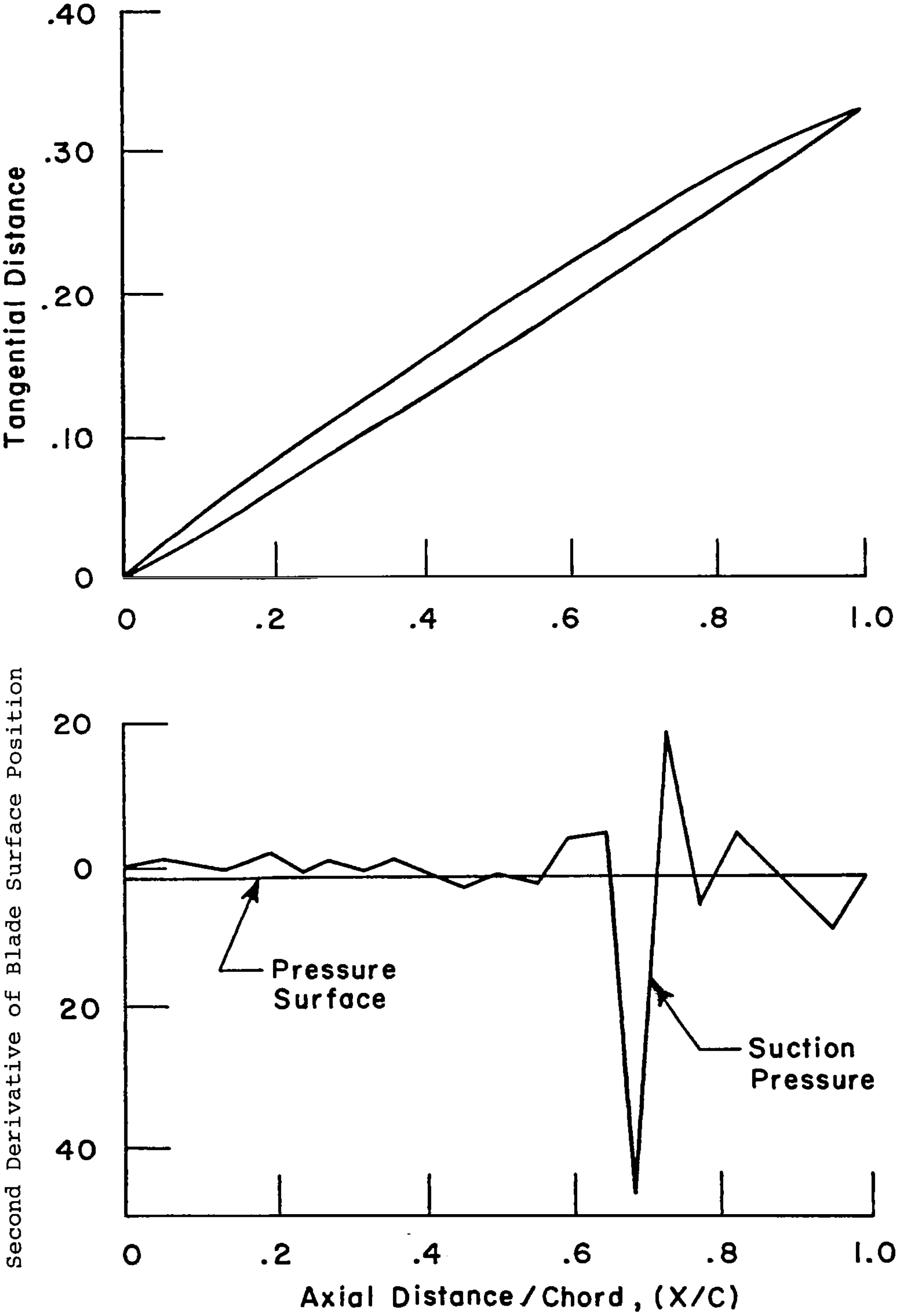

FIGURE 11 TYPICAL BLADE SECTION GEOMETRY AND CALCULATED SECOND DERIVATIVE OF BLADE SURFACE POSITION

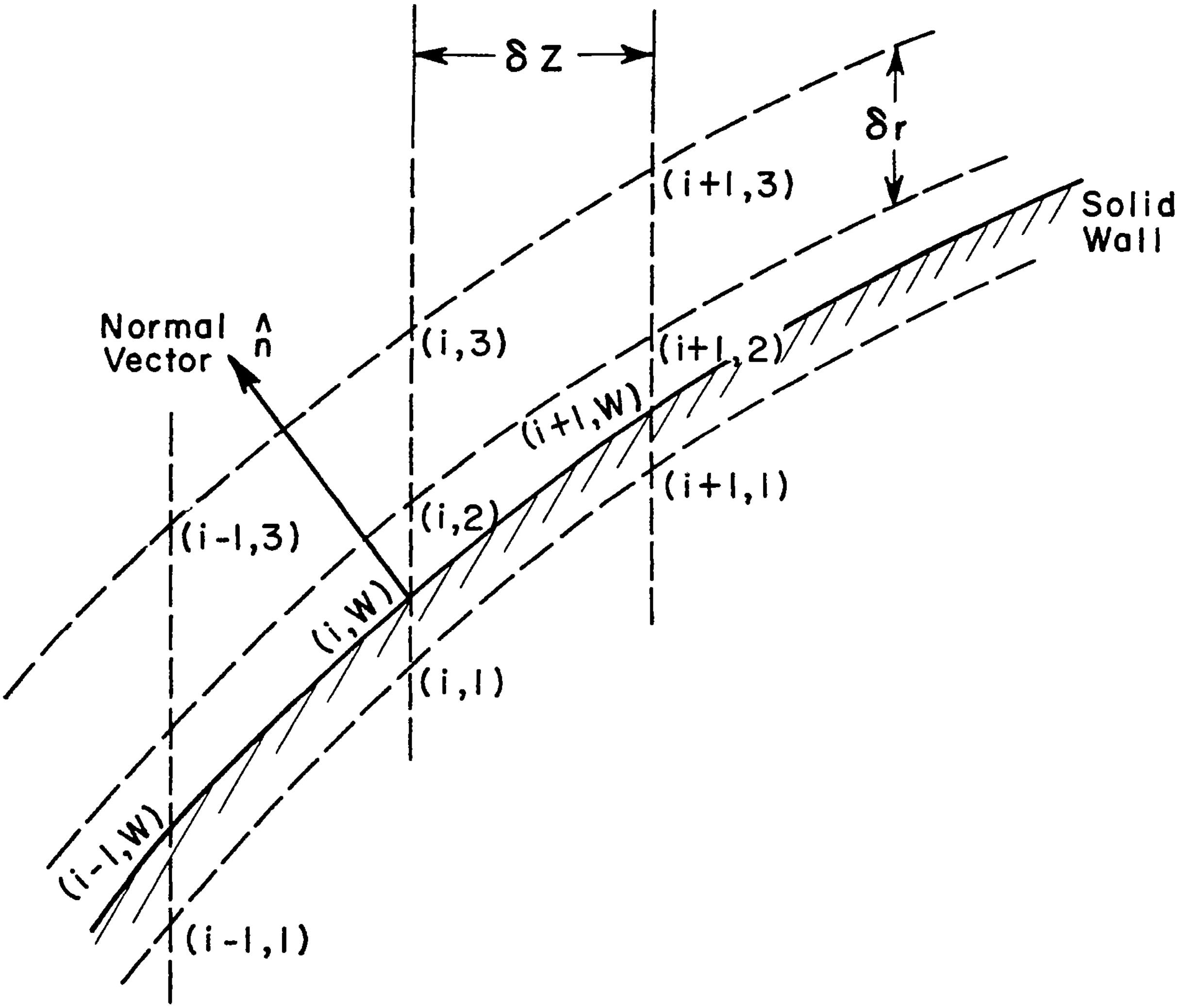

FIGURE 12 GRID POINT NUMBERING SCHEME FOR STAGGERED GRID SYSTEM

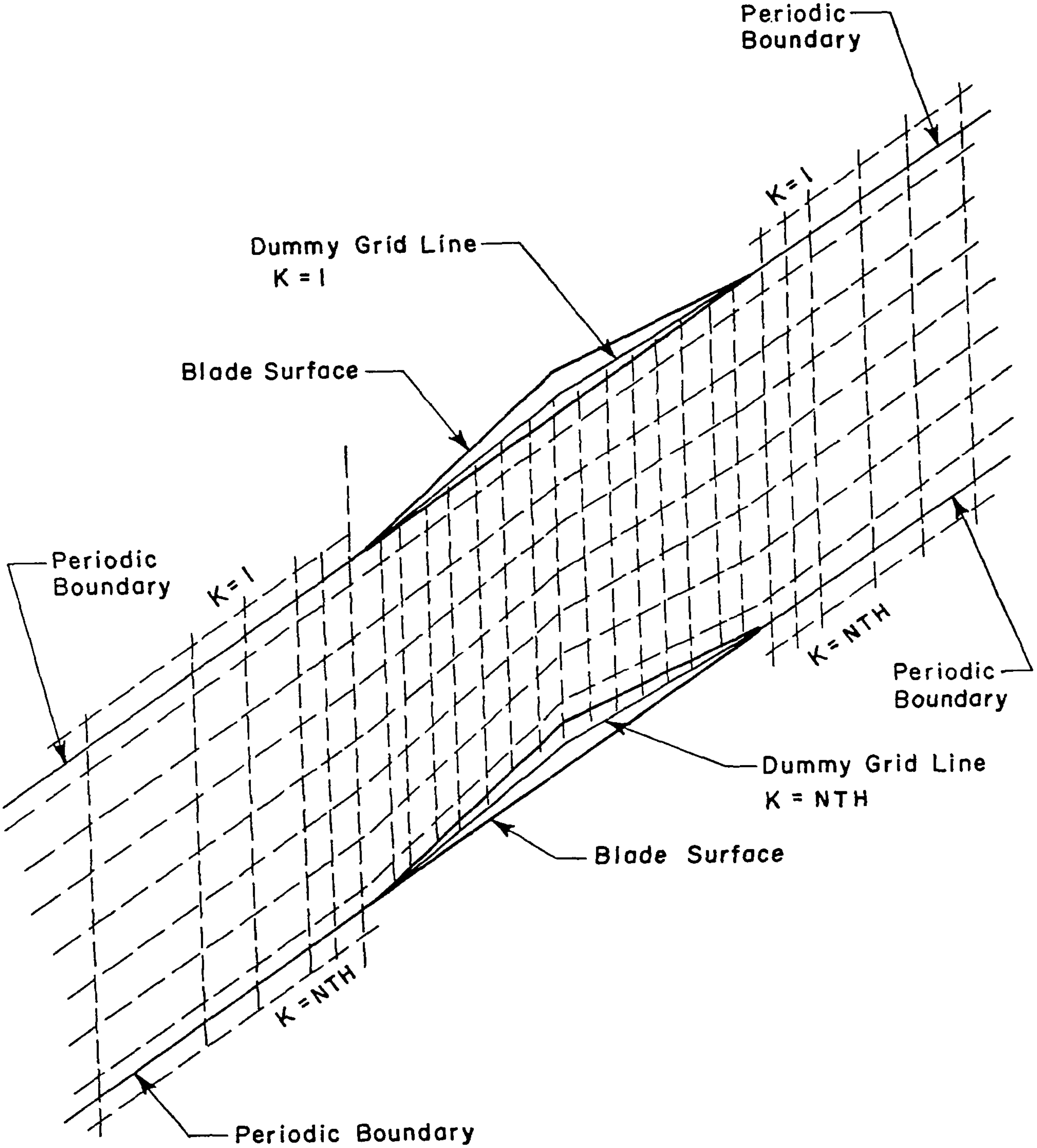

FIGURE 13 BLADE TO BLADE VIEW OF STAGGERED GRID SYSTEM

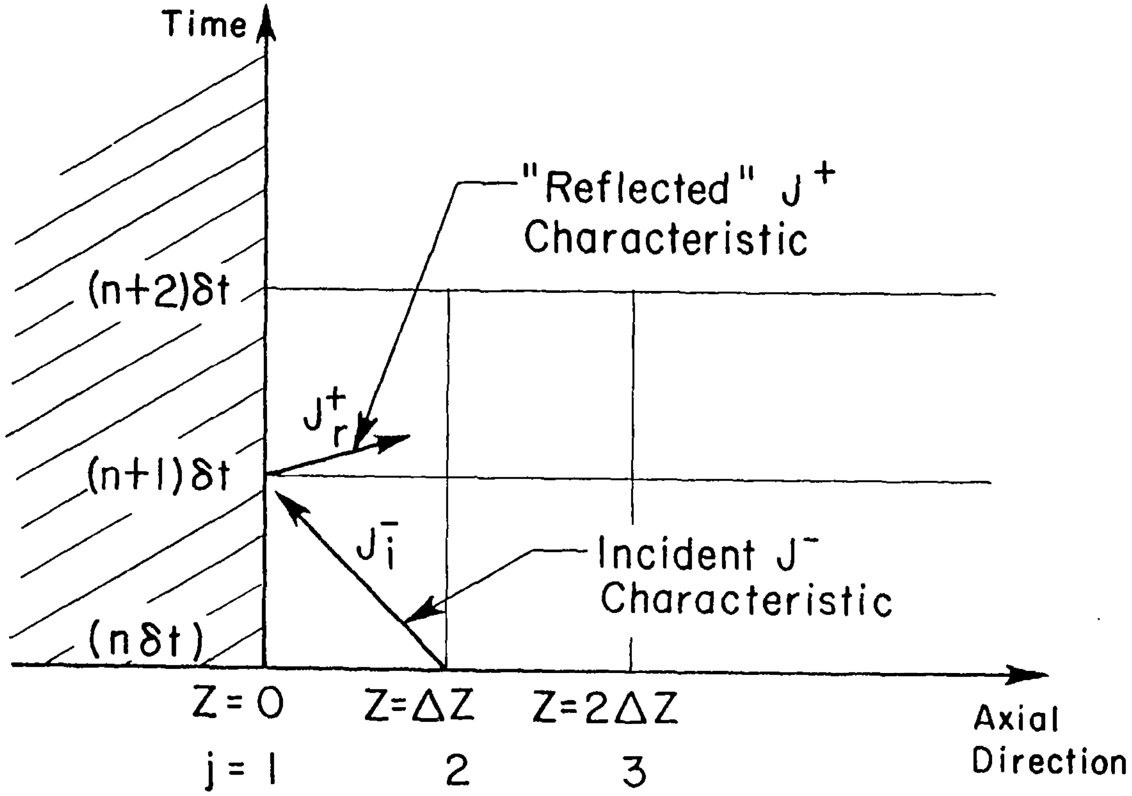

FIGURE 14 INFLOW BOUNDARY CHARACTERISTIC FORMULATION

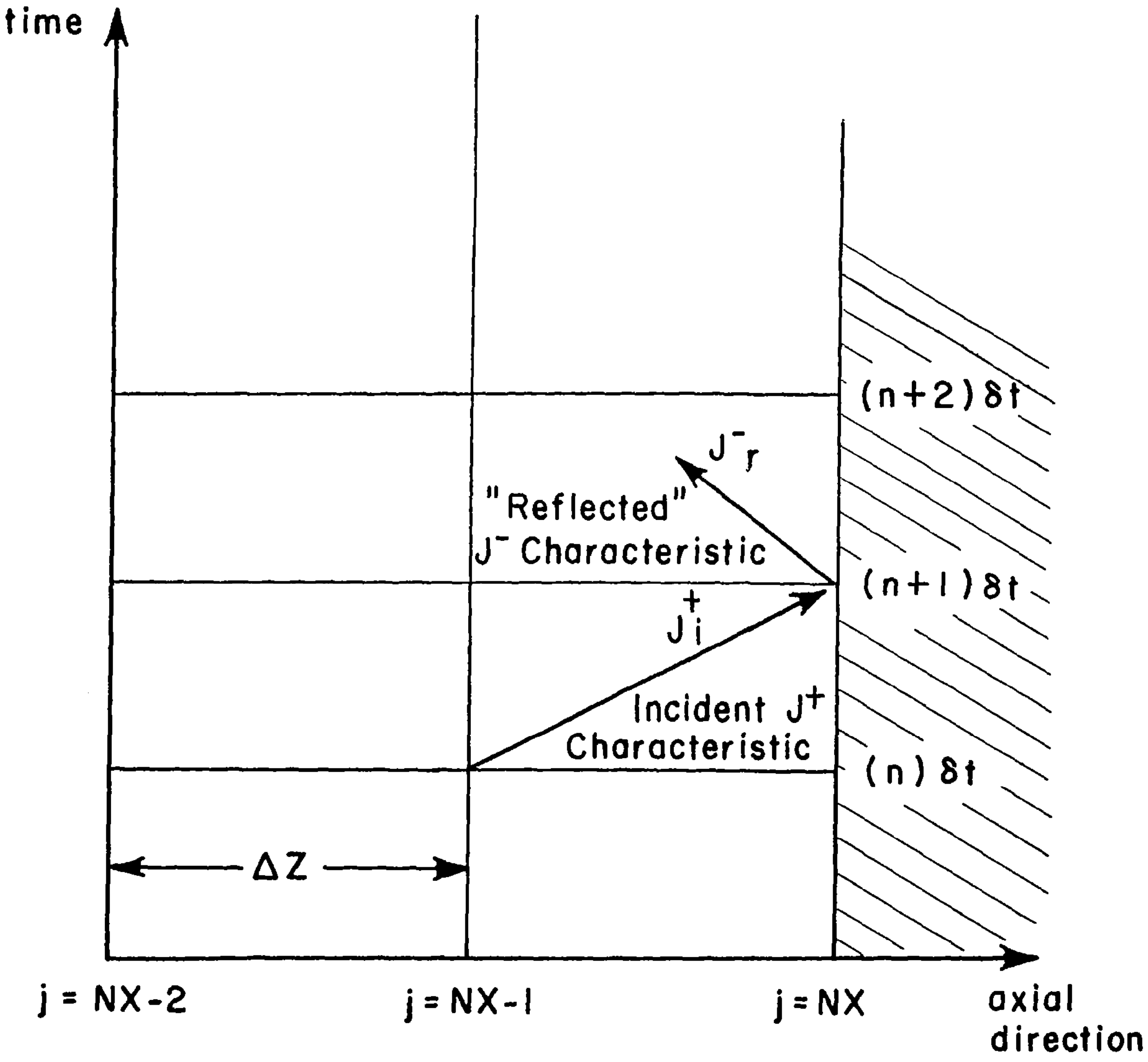

FIGURE 15 OUTFLOW BOUNDARY CHARACTERISTIC FORMULATION

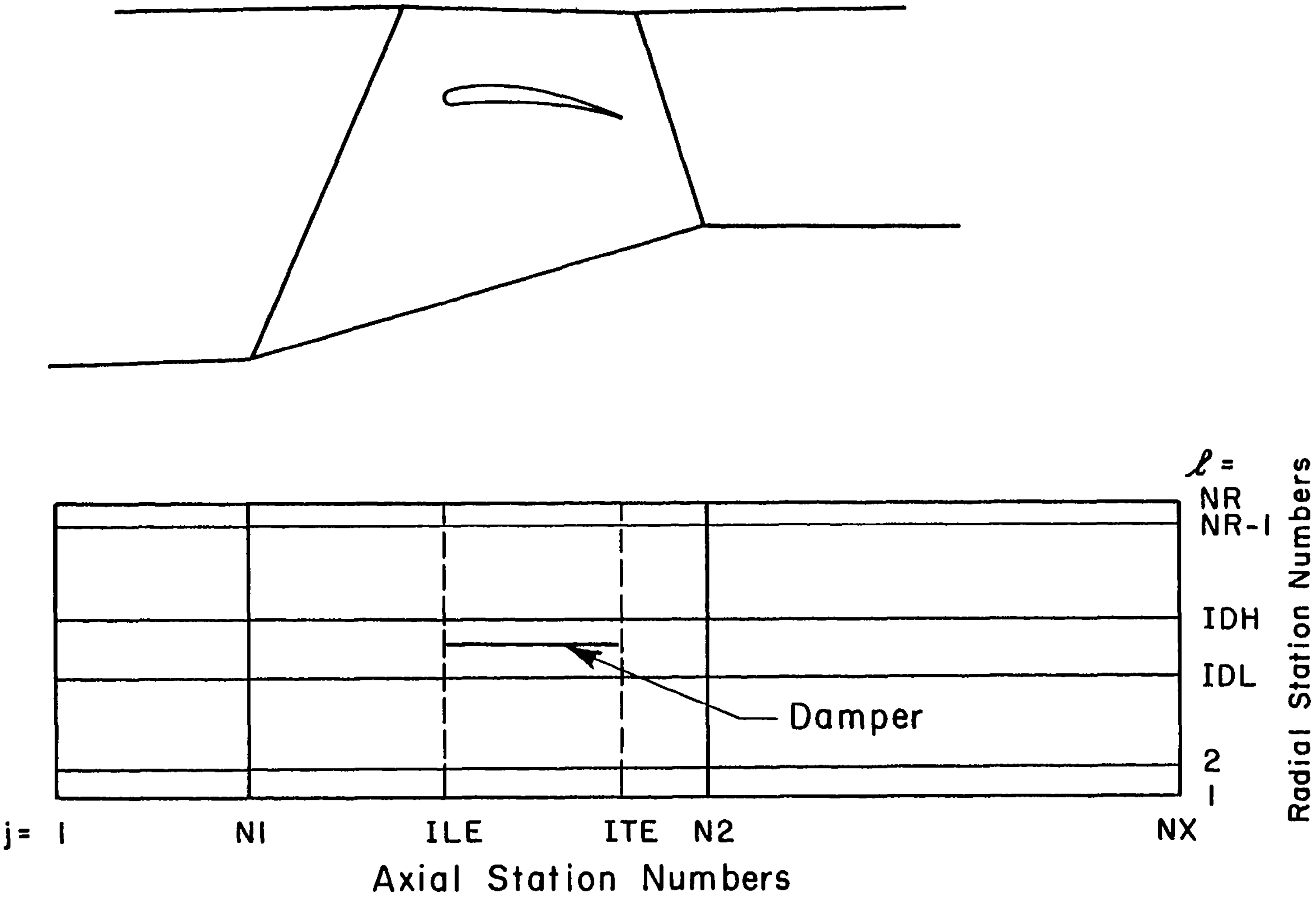

FIGURE 16 COMPUTATIONAL SPACE GRID NUMBERING SCHEME

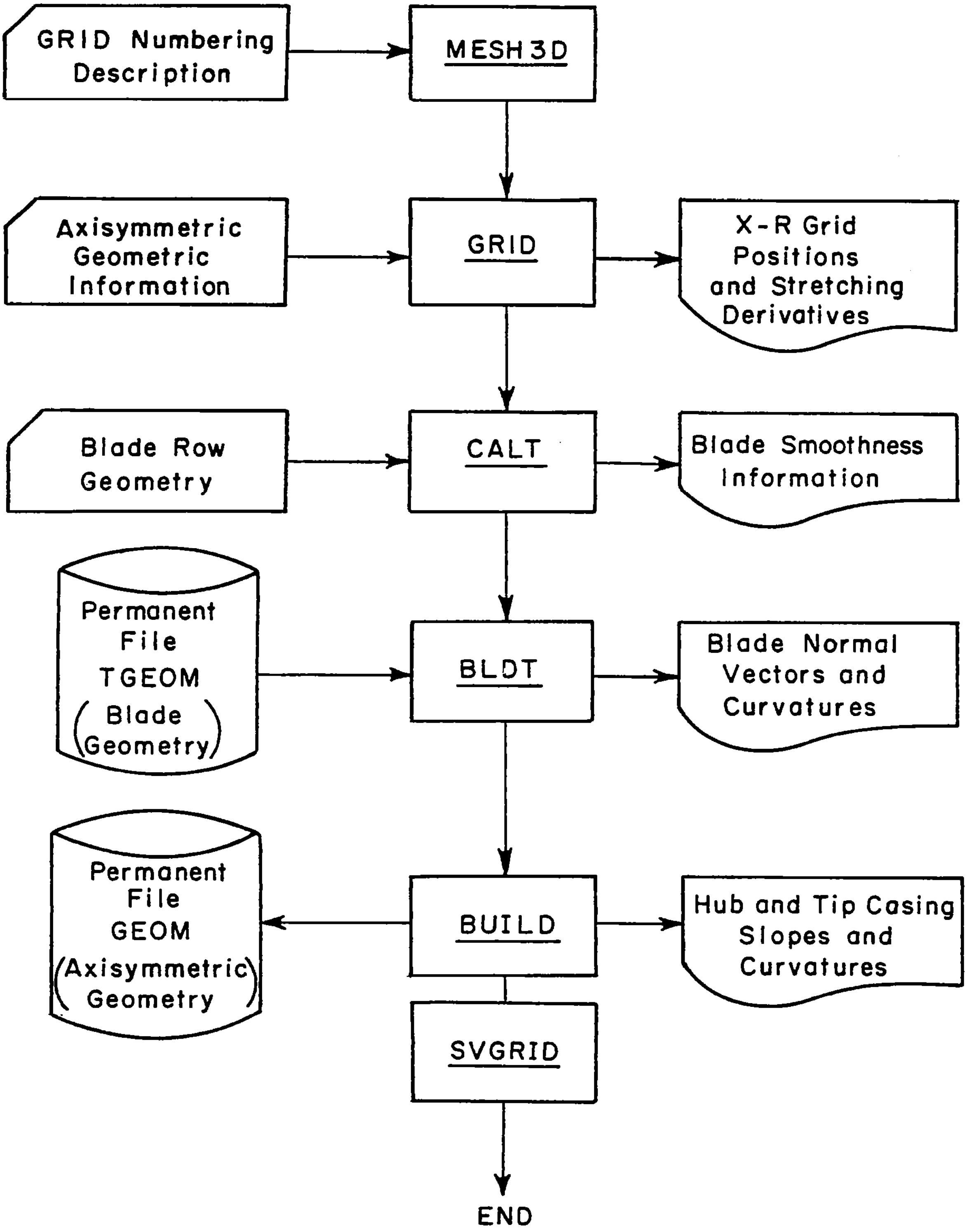

FIGURE 17 FLOWCHART FOR PROGRAM MESH3D

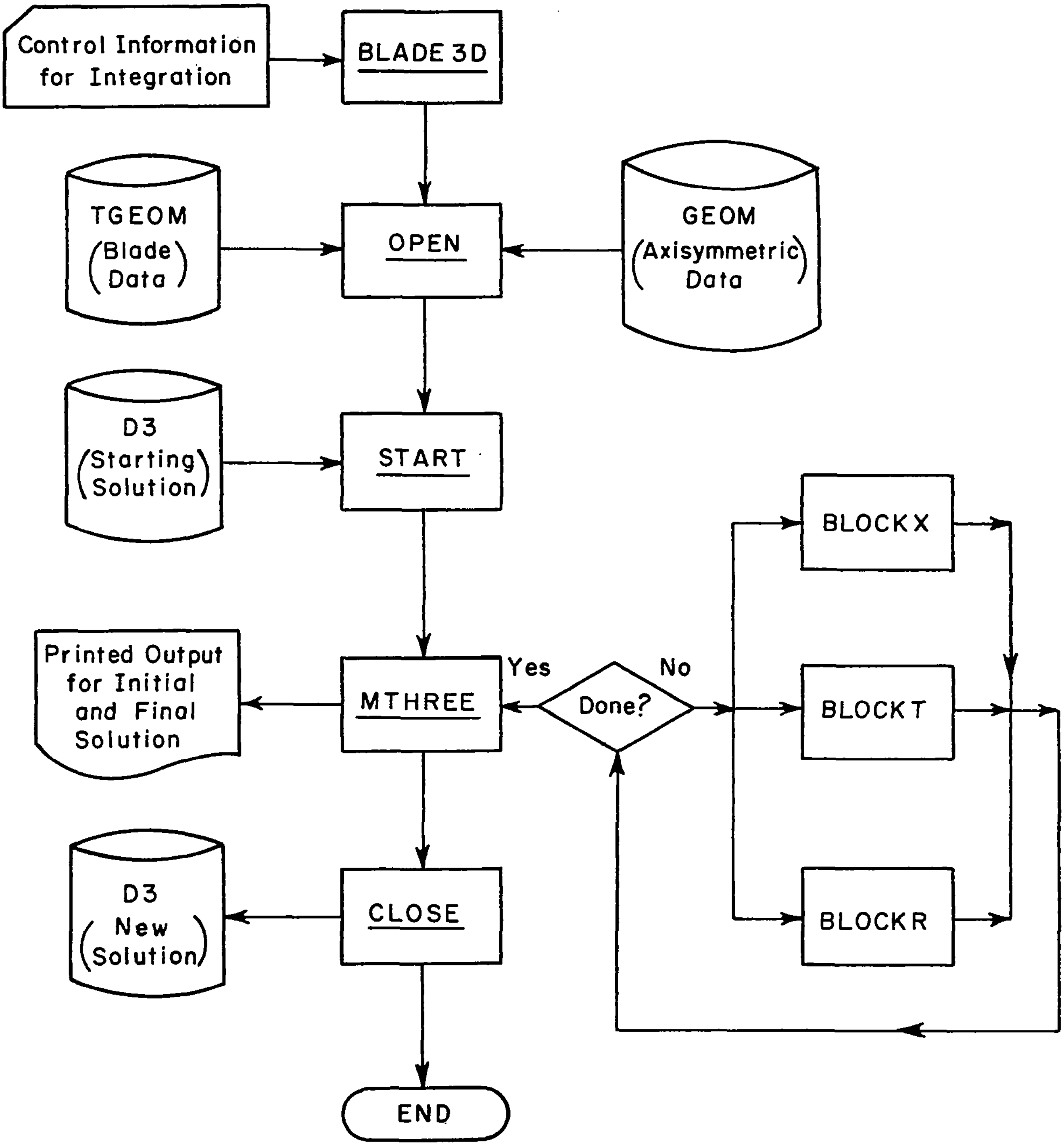

FIGURE 18 FLOWCHART FOR PROGRAM BLADE3D

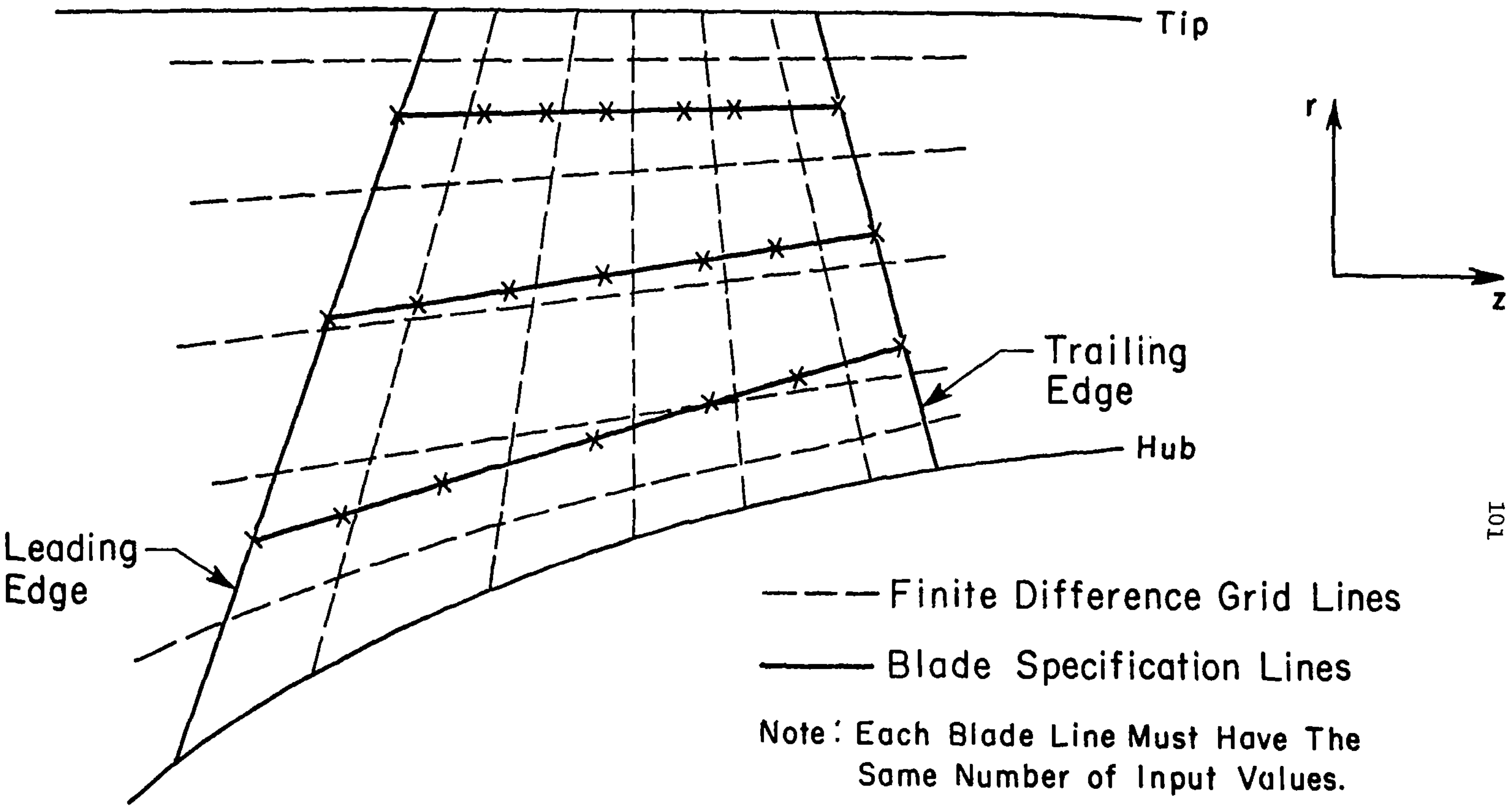

FIGURE 19 PLAN VIEW OF BLADE GEOMETRY SHOWING TYPICAL POSITIONS OF FINITE DIFFERENCE GRID LINES AND BLADE SPECIFICATION LINES

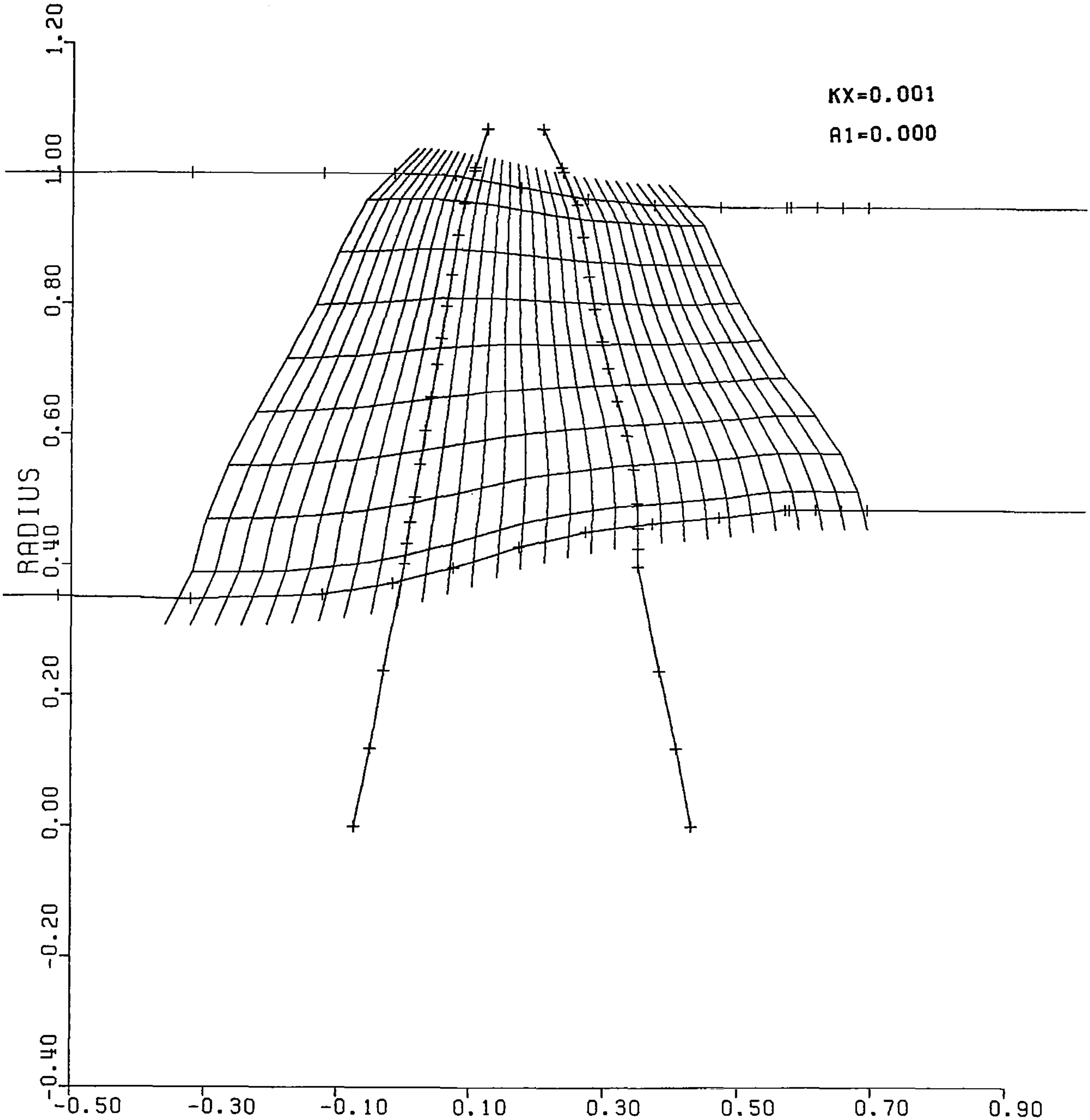

FIGURE 20 AXIAL GRID PLANE SPACING EXAMPLE

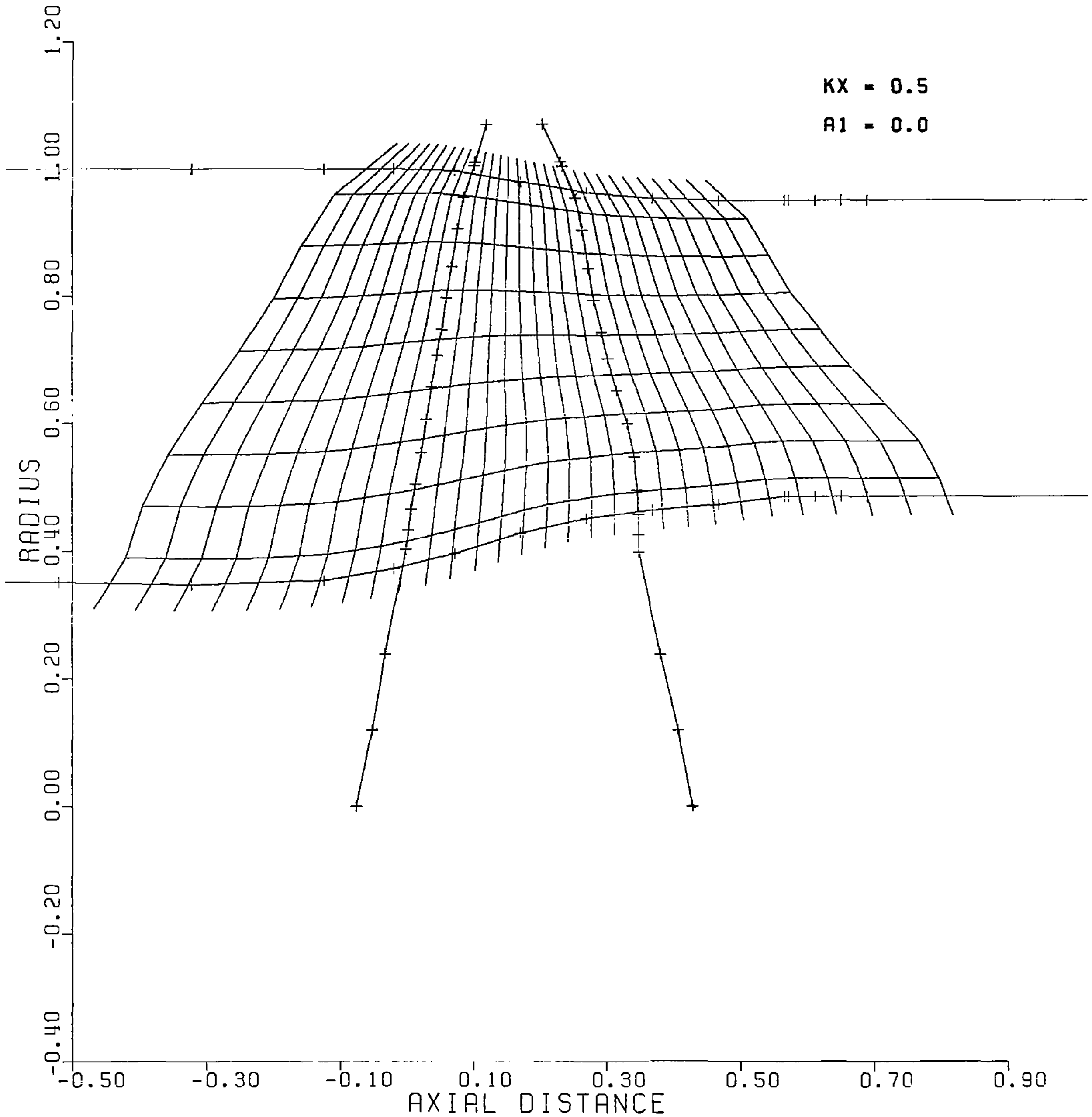

FIGURE 21 AXIAL GRID SPACING EXAMPLE

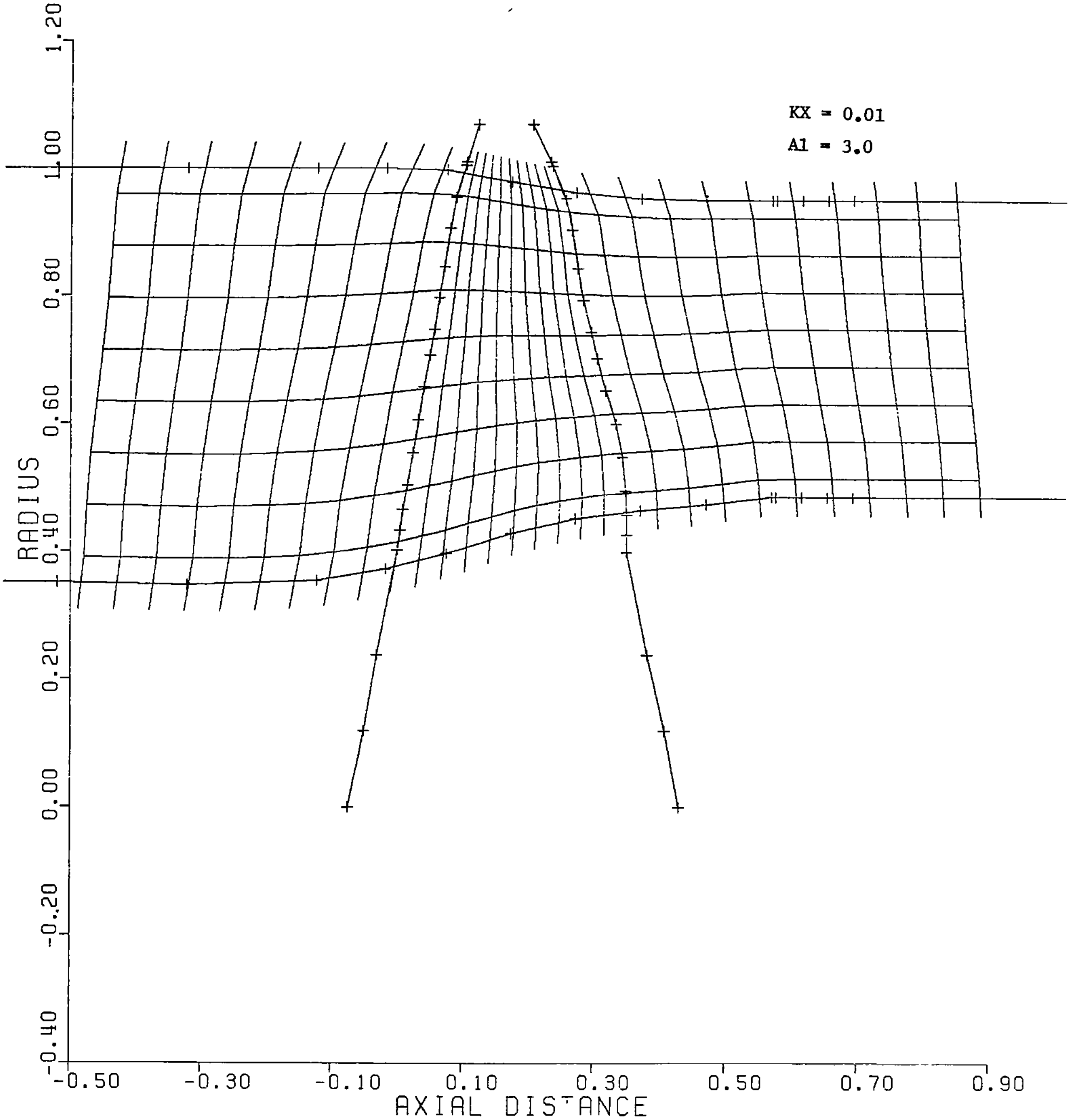

FIGURE 22 AXIAL GRID SPACING EXAMPLE

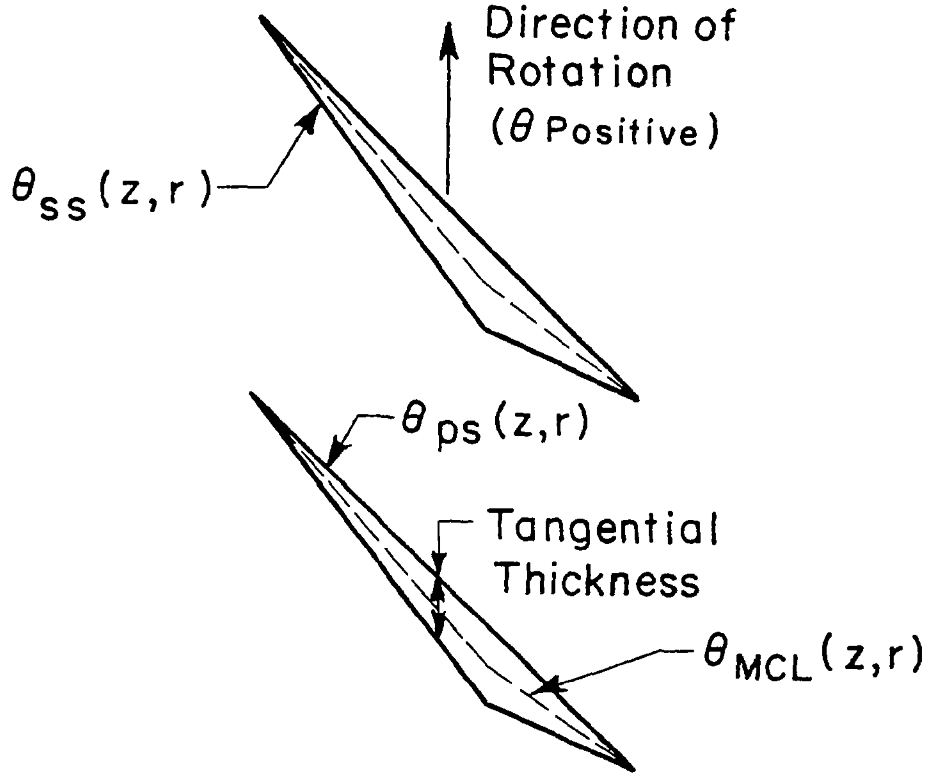

FIGURE 23 BLADE GEOMETRY INPUT TABLE DEFINITIONS

```
 3D AXIAL COMPRESSOR GRID CODE.
-NASA LOW ASPECT RATIO GRID TEST
-THE NUMBER OF BLADES IS     22
-HALF MESH SPACING CONSTANT IS 0.500
-GRID POINTS IN X DIRECTION =     30
-IN THETA DIRECTION =     10 IN R DIRECTION =    10
-THE BLADE LEADING EDGE AND TRAILING EDGE ARE AT AXIAL GRID LINES     10    20
-KUTTA POINT IS AT GRID LINE     20
-THE FIRST POINT ON THE DAMPER IS      0
-THE LAST POINT ON THE DAMPER IS      0
-OUTPUT FILE NUMBER IS    14
-DEBUG DUMP PARAMETER IS      0
-SUBROUTINE GRID FINISHED.IER=     0
-EXTRAPOLATION NEEDED FOR J,L     10     1
-EXTRAPOLATION NEEDED FOR J,L     11     1
-EXTRAPOLATION NEEDED FOR J,L     12     1
-EXTRAPOLATION NEEDED FOR J,L     13     1
-EXTRAPOLATION NEEDED FOR J,L     14     1
-EXTRAPOLATION NEEDED FOR J,L     15     1
-SUBROUTINE CALT FINISHED.IER=     0
-SUBROUTINE BLDT FINISHED
-SUBROUTINE BUILD FINISHED
-SUBROUTINE SVGRID FINISHED
-STOP
```

FIGURE 24   MESH3D RUN LOG FILE

HUB AND TIP COORDINATE INPUT CHECK

```
HUB, TIP, L.E., AND T.E. COORDINATES.

   SCALED RAW DATA INPUT    X,Y PAIRS
                 -3.12771    0.35052
                 -1.17908    0.35052
                 -0.52017    0.35052
                 -0.32230    0.34697
                 -0.12432    0.35438
                 -0.01781    0.37192
                  0.07366    0.39596
                  0.17265    0.42765
                  0.27164    0.45072
                  0.37063    0.46385
                  0.46962    0.47309
                  0.56861    0.48474
                  0.57469    0.48474
                  0.61366    0.48474
                  0.65264    0.48474
                  0.69161    0.48474
                  1.15928    0.48474

   SCALED RAW DATA INPUT    X,Y PAIRS
                 -3.12832    1.00000
                 -1.17931    1.00000
                 -0.52027    1.00000
                 -0.32237    1.00000
                 -0.12435    1.00000
                 -0.01781    0.99988
                  0.07367    0.99673
                  0.17268    0.97950
                  0.27169    0.96207
                  0.37070    0.95346
                  0.46971    0.95049
                  0.56872    0.95049
                  0.57480    0.95049
                  0.61378    0.95049
                  0.65276    0.95049
                  0.69174    0.95049
                  1.15951    0.95049
```

FIGURE 25   MESH3D BULK OUTPUT FILE

HUB AND TIP COORDINATE SMOOTHNESS CHECK

```
HUB, TIP, L.E., AND T.E. DERIVITIVES.

    J          X           Y          DYDX        D2YDX
    1     -3.1283      1.0000      0.0000       0.0000
    2     -1.1793      1.0000      0.0000       0.0001
    3     -0.5203      1.0000     -0.0001      -0.0005
    4     -0.3224      1.0000      0.0003       0.0041
    5     -0.1243      1.0000     -0.0009      -0.0159
    6     -0.0178      0.9999     -0.0006       0.0215
    7      0.0737      0.9967     -0.1033      -2.2658
    8      0.1727      0.9795     -0.2033       0.2448
    9      0.2717      0.9621     -0.1334       1.1673
   10      0.3707      0.9535     -0.0520       0.4784
   11      0.4697      0.9505     -0.0095       0.3784
   12      0.5687      0.9505      0.0003      -0.1786
   13      0.5748      0.9505     -0.0001       0.0136
   14      0.6138      0.9505      0.0000      -0.0036
   15      0.6528      0.9505      0.0000       0.0009
   16      0.6917      0.9505      0.0000       0.0000
   17      1.1595      0.9505      0.0000       0.0000
```

FIGURE 26   MESH3D BULK OUTPUT FILE

R-Z COORDINATES IN PHYSICAL SPACE

```
X-R GRID COORDINATES AND METRICS.
THE AXIAL PACKING FACTOR IS  0.100


 AXIAL      RADIAL     AXIAL      RADIAL
 STATION    STATION    POSITION   POSITION      XX         XR          RR          RX
       1          1     -0.4964    0.3094     3,558     -0.486       1.539       0.033
       1          2     -0.4876    0.3905     3.497     -0.224       1.538       0.029
       1          3     -0.4837    0.4717     3.463     -0.209       1.538       0.026
       1          4     -0.4776    0.5529     3.416     -0.289       1.538       0.022
       1          5     -0,4690    0,6341     3.357     -0.428       1.537       0.018
       1          6     -0.4599    0.7153     3.292     -0.327       1.537       0.014
       1          7     -0.4521    0.7966     3.234     -0.267       1.536       0.010
       1          8     -0.4465    0.8779     3.189     -0.203       1.536       0.006
       1          9     -0.4401    0.9593     3.138     -0.420       1.536       0.002
       1         10     -0.4278    1.0407     3.041     -0.436       1.535      -0.002
```

FIGURE 27   MESH3D BULK OUTPUT FILE

SCALED BLADE ROW GEOMERTY

```
    NASA LOW ASPECT RATIO TWO-STAGE -- NEW ROTOR ONE GEOMETRY -- 8/28/78

INPUT DATA FOR SECTION      1
   L     J          X          R       RTHPS      RTHSS
   1     1   0.00000    0.40147    0.00160   -0.00160
   1     2   0.00127    0.40126    0.00075   -0.00315
   1     3   0.01699    0.39901   -0.00994   -0.02000
   1     4   0.03271    0.39743   -0.01973   -0.03438
   1     5   0.04843    0.39634   -0.02836   -0.04727
   1     6   0.06415    0.39563   -0.03603   -0.05870
   1     7   0.07988    0.39519   -0.04301   -0.06863
   1     8   0.09560    0.39496   -0.04931   -0.07719
   1     9   0.11132    0.39487   -0.05500   -0.08454
   1    10   0.12704    0.39488   -0.06003   -0.09073
   1    11   0.14276    0.39496   -0.06442   -0.09583
   1    12   0.15848    0.39505   -0.06813   -0.09984
   1    13   0.17420    0.39516   -0.07115   -0.10279
   1    14   0.18993    0.39524   -0.07343   -0.10468
   1    15   0.20565    0.39529   -0.07495   -0.10546
   1    16   0.22137    0.39530   -0.07566   -0.10512
   1    17   0.23709    0.39526   -0.07550   -0.10355
   1    18   0.25281    0.39518   -0.07442   -0.10069
   1    19   0.26853    0.39506   -0.07233   -0.09641
   1    20   0.28426    0.39494   -0.06912   -0.09057
   1    21   0.29998    0.39487   -0.06469   -0.08293
   1    22   0.31570    0.39491   -0.05884   -0.07315
   1    23   0.33142    0.39518   -0.05135   -0.06085
   1    24   0.34714    0.39589   -0.04230   -0.04448
   1    25   0.34805    0.39595   -0.04179   -0.04331

SECOND DERIVATIVE CHECK FOR PRESSURE SURFACE

   J        X         Y       DYDX      D2YDX
   1    0.0000    0.0016   -0.6722   -1.7001
   2    0.0013    0.0008   -0.6754   -3.4001
   3    0.0170   -0.0099   -0.6619    5.1238
   4    0.0327   -0.0197   -0.5845    4.7202
   5    0.0484   -0.0284   -0.5155    4.0563
   6    0.0642   -0.0360   -0.4644    2.4397
   7    0.0799   -0.0430   -0.4224    2.9042
   8    0.0956   -0.0493   -0.3810    2.3609
   9    0.1113   -0.0550   -0.3412    2.7080
  10    0.1270   -0.0600   -0.2998    2.5585
  11    0.1428   -0.0644   -0.2579    2.7705
  12    0.1585   -0.0681   -0.2141    2.7992
  13    0.1742   -0.0711   -0.1687    2.9773
  14    0.1899   -0.0734   -0.1212    3.0727
  15    0.2056   -0.0749   -0.0716    3.2260
  16    0.2214   -0.0757   -0.0182    3.5723
  17    0.2371   -0.0755    0.0388    3.6729
  18    0.2528   -0.0744    0.0996    4.0731
  19    0.2685   -0.0723    0.1674    4.5474
  20    0.2843   -0.0691    0.2414    4.8666
  21    0.3000   -0.0647    0.3252    5.7928
  22    0.3157   -0.0588    0.4195    6.2089
```

FIGURE 28   MESH3D BULK OUTPUT FILE

CALCULATED BLADE NORMAL VECTORS AND CURVATURES

```
NORMAL VECTORS AND RADII OF CURVATURE FOR AXIAL STATION NO.     10
 L  COSNR  COSNT  COSNZ    RES    RTAU L  COSNR  COSNT  COSNZ    RES   RTAU
PRESSURE SIDE NORMAL VECTOR
 1 -0.099  0.841  0.532  0.000  0.000 2 -0.073  0.823  0.563  0.000 -0.198
 4 -0.148  0.765  0.627  0.000  0.074 5 -0.142  0.678  0.721  0.000  0.850
 7 -0.070  0.573  0.817  0.000  0.299 8 -0.060  0.532  0.845  0.000  0.686
10 -0.072  0.435  0.897  0.000  0.000
```

FIGURE 29   MESH3D BULK OUTPUT FILE

CALCULATED HUB AND TIP CASING SPLOE

CALCULATED TRANSFORM JACOBIAN VALUES

```
   HUB SLOPE    HUB CURV.     TIP SLOPE    TIP CURV. FOR AXIAL STATION NO.      1
    -0.02018      0.04881      -0.00006      0.00151
 JACOBIANS FOR RADIAL GRID LOCATIONS.
  1  19.22562  2  18.85800  3  18.66972  4  18.41212  5  18.09552  6  17.72968
  7  17.41035  8  17.15939  9  16.88091 10  16.34608
```

FIGURE 30   MESH3D BULK OUTPUT FILE

```
INVISCID 3-D AXIAL COMPRESSOR ANALYSIS CODE.
NASA LOW ASPECT RATIO ROTOR TEST
THE NUMBER OF BLADES IS    22
 50 CYCLES ARE TO BE RUN WITH DT =     0.00200


OPERATOR SEQUENCE IS
OPERATOR,DT MULTIPLER,REPEAT COUNT
   T OP            1            8
   X OP            1            8
   R OP            8            1
   R OP            8            1
   X OP            1            8
   T OP            1            8
GRID POINTS IN X DIRECTION IS    60
GRID POINTS IN THETA DIRECTION IS    17
GRID POINTS IN R DIRECTION IS    18
THE BLADE LEADING AND TRAILING EDGES ARE  AT AXIAL STATIONS    25 AND    45
THE KUTTA POINT IS LOCATED AT AXIAL STATION    45
FIRST DAMPER STATION IS AT     0
THE LAST DAMPER STATION IS AT     0
IDLOW  IS     1
IDHIGH IS   18
GAMMA  IS  1.400
BLADE SPEED (WRT/AO) IS  1.271
ARTIFICAL VISCOSITY PARAMETER IS 0.400
DOWNSTREAM PRESSURE IS TO BE SET TO  0.780
UPSTREAM MACH NUMBER PARAMETER IS  0.510


   L  RADIUS    UTHETA     TTIN      PTIN OR JPLUS
   1  0.33194   0.00000   1.00000   5.32000
   2  0.37240   0.00000   1.00000   5.32000
   3  0.41288   0.00000   1.00000   5.32000
   4  0.45336   0.00000   1.00000   5.32000
   5  0.49385   0.00000   1.00000   5.32000
   6  0.53432   0.00000   1.00000   5.32000
   7  0.57480   0.00000   1.00000   5.32000
   8  0.61528   0.00000   1.00000   5.32000
   9  0.65576   0.00000   1.00000   5.32000
  10  0.69625   0.00000   1.00000   5.32000
  11  0.73674   0.00000   1.00000   5.32000
  12  0.77723   0.00000   1.00000   5.32000
  13  0.81773   0.00000   1.00000   5.32000
  14  0.85823   0.00000   1.00000   5.32000
  15  0.89874   0.00000   1.00000   5.32000
  16  0.93924   0.00000   1.00000   5.32000
  17  0.97975   0.00000   1.00000   5.32000
  18  1.02026   0.00000   1.00000   5.32000
```

FIGURE 31   BLADE3D RUN LOG FILE

```
GRID OUTPUT FOR  30 TO  30 IN ABS  SYSTEM
NASA LOW ASPECT RATIO ROTOR TEST


 30  5         1       2       3       4       5       6       7       8       9      10
    PT     0.944   0.940   0.937   0.934   0.932   0.929   0.925   0.919   0.912   0.904
    MR     0.102   0.102   0.103   0.105   0.106   0.108   0.112   0.115   0.117   0.119
    MTH    0.355   0.357   0.351   0.345   0.337   0.327   0.316   0.305   0.294   0.282
    MX     0.521   0.523   0.533   0.547   0.561   0.576   0.589   0.602   0.614   0.625
    TT     1.116   1.109   1.103   1.097   1.091   1.085   1.081   1.078   1.075   1.072

THETA AVERAGE PROPERTIES.
    %SPAN    PT      MR      MTH     MX      TT
    0.227   0.898   0.119   0.294   0.603   1.074
```

FIGURE 32 BLADE3D BULK OUTPUT FILE

SOLUTION MATRIX FOR

AXIAL GRID PLANE 30

RADIAL GRID PLANE 5

NON-DIMENSIONAL FLOW VARIABLES AT

TANGENTAL POINTS 1 TO 10

```
 L   RADIUS MACH NUMBERS            P  ON   T  ON   ANGLES
            MERID  TANGEN  TOTAL   PREF    TREF    WHIRL   MERID
 1   0.381  0.556   0.34   0.654   1.257   1.002    31.7    18.1
 2   0.419  0.544   0.31   0.624   1.199   1.060    29.4    16.8
 3   0.458  0.577   0.31   0.653   1.222   1.062    27.9    14.3
 4   0.496  0.599   0.30   0.671   1.241   1.069    26.9    12.6
 5   0.533  0.615   0.29   0.682   1.259   1.074    25.5    11.1
 6   0.571  0.625   0.28   0.685   1.273   1.077    24.2    10.1
 7   0.608  0.630   0.26   0.683   1.280   1.077    22.7     9.4
 8   0.645  0.635   0.24   0.678   1.269   1.073    20.5     8.5
 9   0.681  0.647   0.20   0.678   1.245   1.065    17.6     7.0
10   0.718  0.660   0.17   0.681   1.215   1.057    14.2     4.8
11   0.755  0.665   0.14   0.679   1.185   1.049    11.5     2.8
12   0.791  0.664   0.11   0.673   1.157   1.042     9.4     1.0
13   0.827  0.659   0.09   0.666   1.134   1.035     7.9    -0.8
14   0.863  0.652   0.08   0.657   1.114   1.030     6.7    -2.9
15   0.899  0.640   0.07   0.643   1.098   1.027     5.8    -4.7
16   0.935  0.627   0.06   0.629   1.078   1.025     5.1    -7.5
17   0.970  0.597   0.06   0.600   1.101   1.024     5.4    -7.4
18   1.005  0.589   0.06   0.592   1.066   1.034     5.7   -13.6
```

FIGURE 33   BLADE3D BULK OUTPUT FILE
THETA AVERAGED FLOW QUANTITES
AXIAL GRID PLANE 30

```
-                              AXIAL GRID PLANE
-              1.08E+01            3.05E+01            5.02E+01
-    1.00E+00            2.07E+01            4.03E+01            6.00E+01
-        0+---------+---------+---------+---------+---------+---------+0
- 122.86 ++         +         +         +         +         +         ++
-        -                                                             -
-        -                                                             -
-        -                                                             -
-        -                                                             -
-M       -                                                             -
-A117.28 ++         +         +         +         +         +         ++
-S       -                                                             -
-S       -                                                             -
-        -                                                             -
-F       -                                                             -
-L       - M                                       MMMMM M M   M      M-
-D111.69 +M MMMMMMMMMMMMMMMMM M M       +     MMMMM     M M MMM MMMMMM++
-W       -                   M M  MMMMMM MMMMM                         -
-        -                                                             -
-R       -                       M                                     -
-A       -                                                             -
-T       -                                                             -
-E106.11 ++         +         +         +         +         +         ++
-        -                                                             -
-        -                                                             -
-        -                                                             -
-        -                                                             -
-        -                                                             -
- 100.52 ++         +         +         +         +         +         ++
-        0+---------+---------+---------+---------+---------+---------+0
-    1.00E+00            2.07E+01            4.03E+01            6.00E+01
-              1.08E+01            3.05E+01            5.02E+01
-                              AXIAL GRID PLANE
-
-
```

FIGURE 34   BLADE3D BULK OUTPUT FILE

MASS FLOW RATE VS. AXIAL GRID PLANE

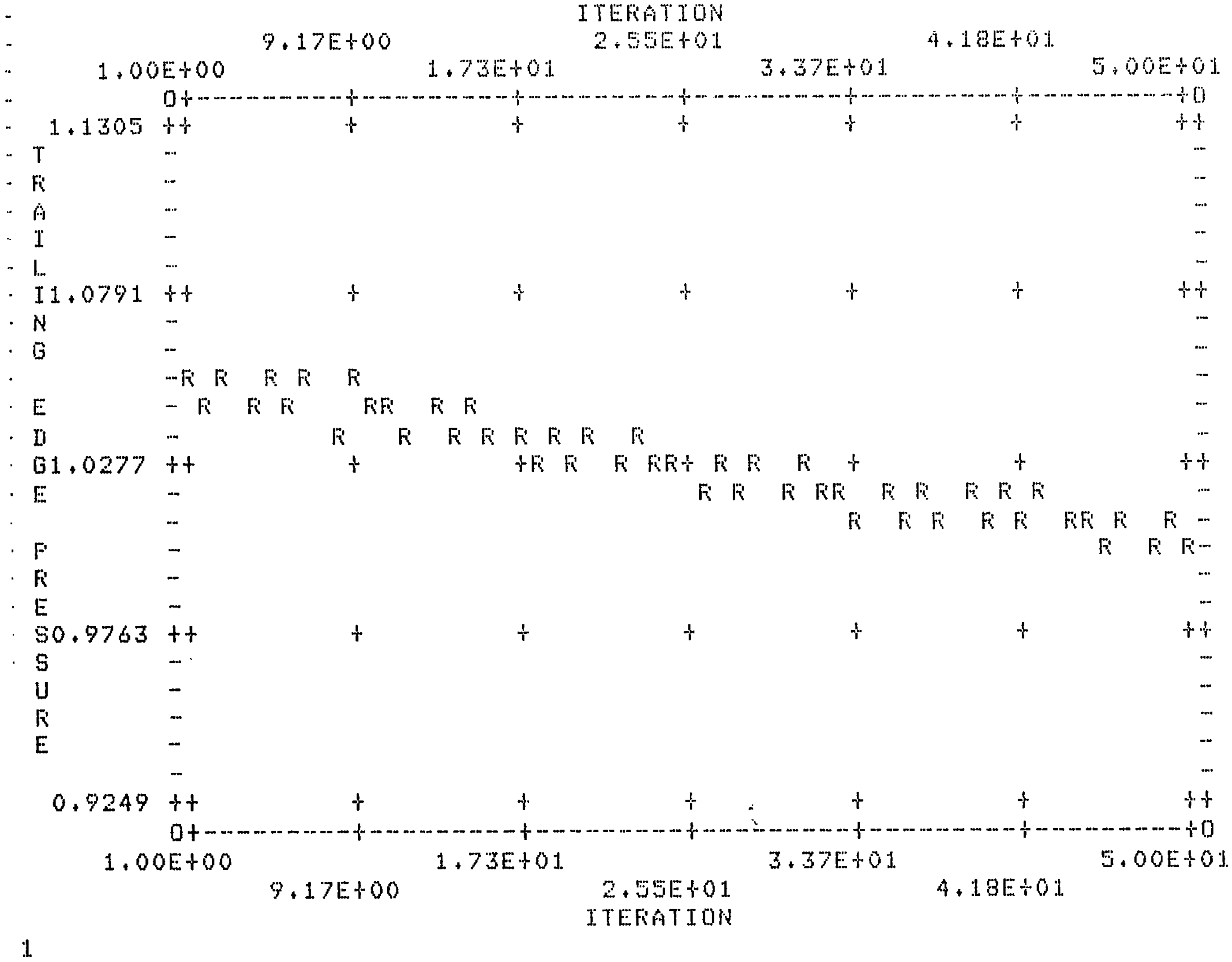

FIGURE 35 BLADE3D BULK OUTPUT FILE

TRAILING EDGE STATIC PRESSURE

VS. ITERATION NUMBER

```
-                              AXIAL GRID PLANE
-              1.08E+01            3.05E+01            5.02E+01
-    1.00E+00            2.07E+01            4.03E+01            6.00E+01
-        0+---------+---------+---------+---------+---------+---------+---------+0
- .99507 ++         +         +         +         +     S   +         ++
-        -                                           PPPP              -
-        -                                        PPP    XXXXXXXXXXXXXX-
-        -                                      PP    SS               -
-        -                                    PP                       -
-        -                                   P       S                 -
-S.85198 ++         +         +         +   P     + S       +         ++
-T       -                                PP       S                   -
-A       -                               P        S                    -
-I       -                             P         S                     -
-C       -                        P   P         S                      -
-        -                           P         S                       -
-P.70889 ++         +         +    PP   +     S   +         +         ++
-R       -                                                             -
-E       -                                   S                         -
-S       -                                  S                          -
-U       -                                 S                           -
-R       -X                      S                                     -
-E.56580 ++XXXXXXXXXXXXXXXXXXXXP P      + S       +         +         ++
-        -                     SX S                                    -
-        -                         S     S                             -
-        -                                                             -
-        -                          S                                  -
-        -                           S S                               -
- .42271 ++         +         +       S +         +         +         ++
-        0+---------+---------+---------+---------+---------+---------+---------+0
-    1.00E+00            2.07E+01            4.03E+01            6.00E+01
-              1.08E+01            3.05E+01            5.02E+01
-                              AXIAL GRID PLANE
-
```

FIGURE 36   BLADE3D BULK OUTPUT FILE

STATIC PRESSURE ON RADIAL GRID PLANE 5

```
     STATIC PRESSURE DIVIDED BY PREF
     FOR S1 SURFACE    16
                               AXIAL DISTANCE
              5.48E-02            1.73E-01            2.91E-01
   -4.22E-03            1.14E-01            2.32E-01            3.50E-01
        0+---------+---------+---------+---------+---------+---------+0
 1.7581 ++         +         +         +    P    +         +         ++
        -                                                             -
        -                                    P                        -
        -                                 P                           -
        -                                                             -
        -                                                             -
 1.5069 ++         +         +         +       P +         +         ++
        -                                                             -
        -                                          P P                -
        -                                       P                     -
        -                                         P                   -
        -                               P                             -
 1.2558 ++         +         +         +         +         +         ++
        -                                                             -
S       -                                             PS              -
T       -                                                             -
A       -                                                             -
T       -                                                             -
I1.0046 ++         +         +         +         +         +         ++
C       -                                                             -
        -               P              P                              -
P       -                P PP                                         -
R       -                     PP                                      -
E       -               S S      P                                    -
S0.7535 ++         +       SS+SS SX    +         +         +         ++
S       -                           XX SS                             -
U       -                                 S                           -
R       -                                   S                         -
E       -                                    S                        -
        -                                      SS    S                -
 0.5023 ++         +         +         +         +SS       +         ++
        -                                                             -
        -                                                             -
        -                                                             -
        -                                                             -
        -                                                             -
 0.2512 ++         +         +         +         +         +         ++
        -                                                             -
        -                                                             -
        -                                                             -
        -                                                             -
        -                                                             -
 0.0000 ++         +         +         +         +         +         ++
        0+---------+---------+---------+---------+---------+---------+0
   -4.22E-03            1.14E-01            2.32E-01            3.50E-01
              5.48E-02            1.73E-01            2.91E-01
                               AXIAL DISTANCE
```

FIGURE 37 GRAPH3D BULK OUTPUT FILE

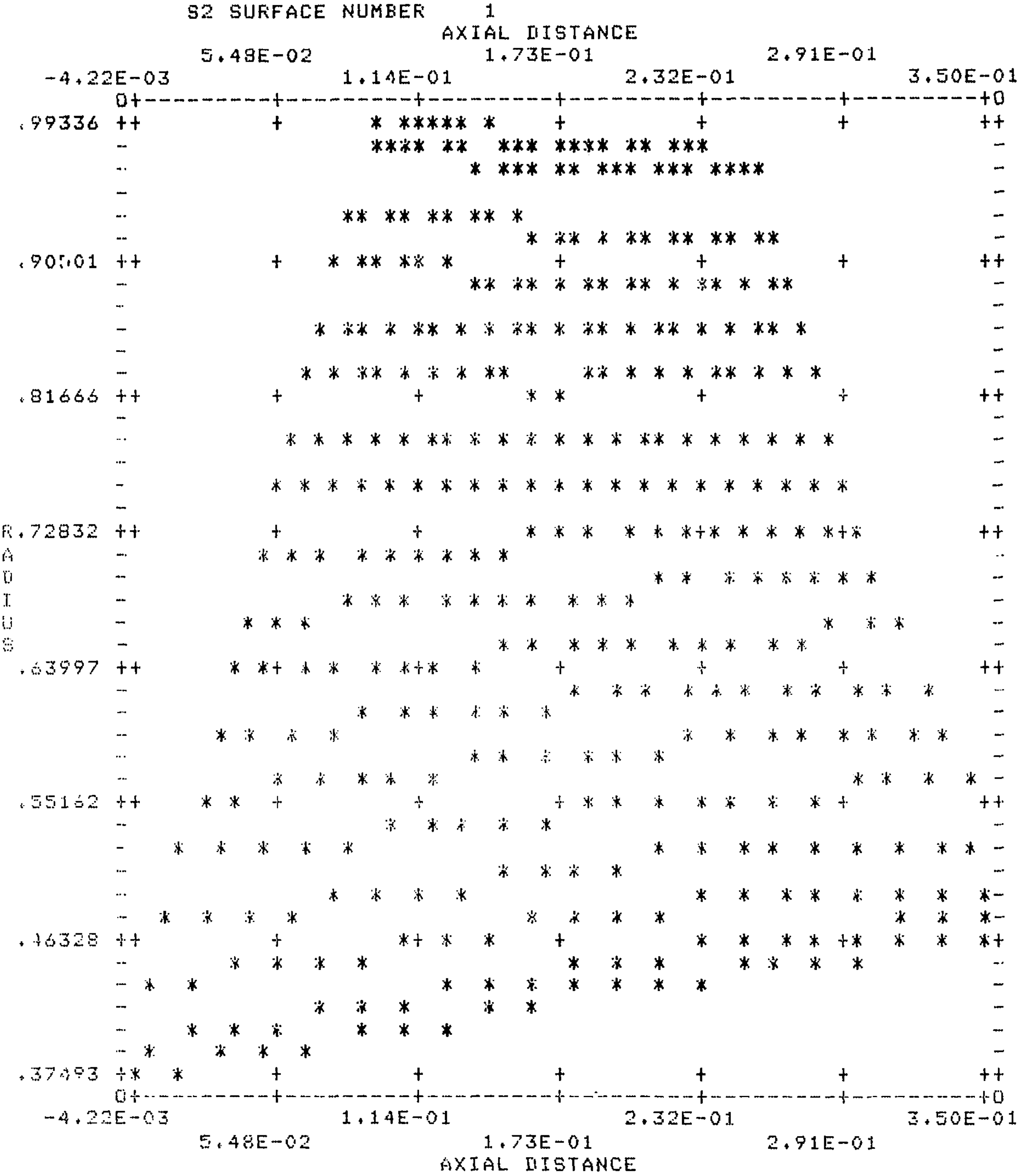

FIGURE 38 GRAPH3D BULK OUTPUT FILE

STREAMLINE POSITIONS

```
 L  RADIUS MACH NUMBERS               PRESS  DEL T  ANGLES
           MERID  TANGEN TOTAL  RATIO  ON   T  WHIRL  MERID
 1  0.444  0.535   0.75  0.924  1.725  0.184   54.6    6.6
 2  0.475  0.529   0.73  0.898  1.675  0.176   53.9    8.9
 3  0.506  0.529   0.69  0.872  1.730  0.172   52.7    7.3
 4  0.537  0.503   0.65  0.823  1.720  0.175   52.3    6.4
 5  0.568  0.483   0.61  0.782  1.722  0.177   51.8    5.7
 6  0.598  0.474   0.58  0.752  1.735  0.178   50.9    5.1
 7  0.629  0.472   0.56  0.730  1.750  0.179   49.7    4.5
 8  0.660  0.473   0.53  0.710  1.763  0.180   48.3    4.0
 9  0.691  0.471   0.51  0.692  1.775  0.180   47.1    3.5
10  0.723  0.469   0.49  0.676  1.784  0.180   46.0    2.9
11  0.754  0.468   0.47  0.662  1.786  0.180   45.0    2.2
12  0.786  0.467   0.45  0.649  1.775  0.179   44.0    1.3
13  0.818  0.468   0.44  0.639  1.756  0.176   42.9    0.3
14  0.851  0.471   0.42  0.632  1.729  0.173   41.8   -1.1
15  0.883  0.478   0.41  0.628  1.697  0.169   40.4   -3.0
16  0.916  0.487   0.40  0.629  1.666  0.166   39.3   -5.1
17  0.949  0.527   0.37  0.643  1.642  0.150   35.0   -8.0
18  0.984  0.523   0.36  0.635  1.552  0.142   34.6   -8.9
```

FIGURE 39 GRAPH3D BULK OUTPUT FILE
THETA AVERAGED BLADE ROW PERFORMANCE

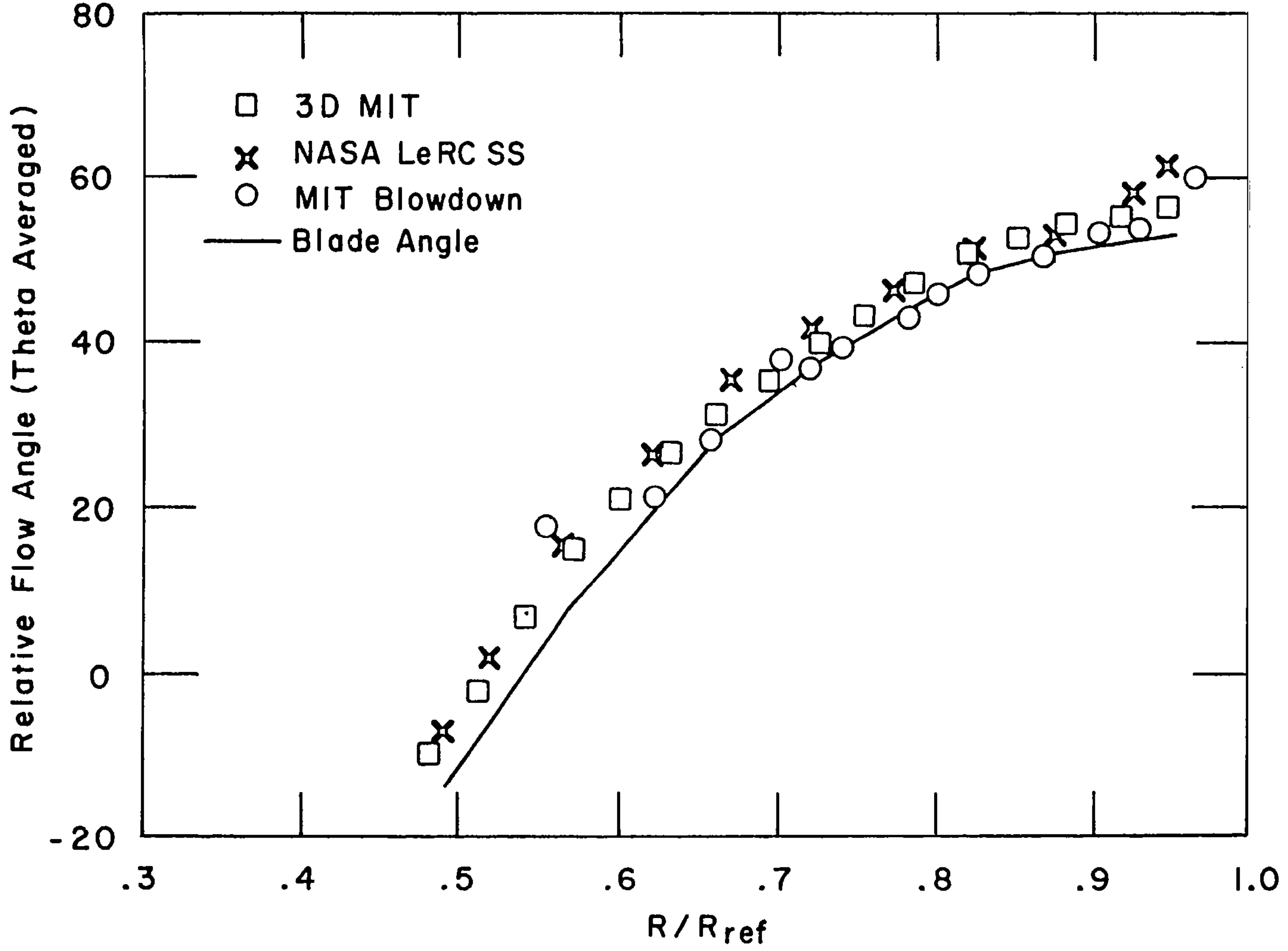

FIGURE 40 NASA LOW ASPECT RATIO ROTOR

RELATIVE FLOW ANGLE , THETA AVERAGED

ROTOR TRAILING EDGE

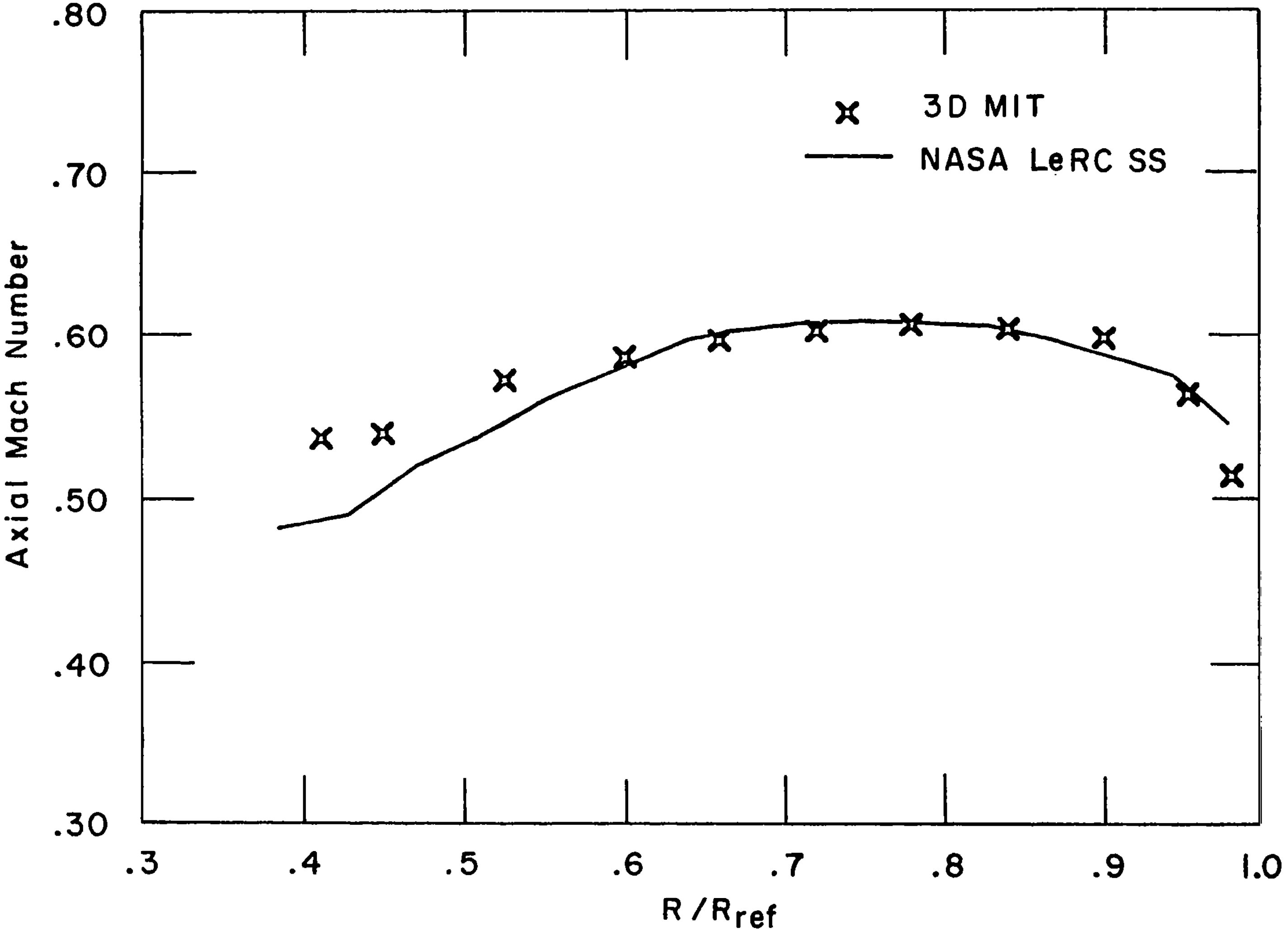

FIGURE 41 NASA LOW ASPECT RATIO ROTOR
MERIDIONAL MACH NUMBER , THETA AVERAGED
ROTOR LEADING EDGE

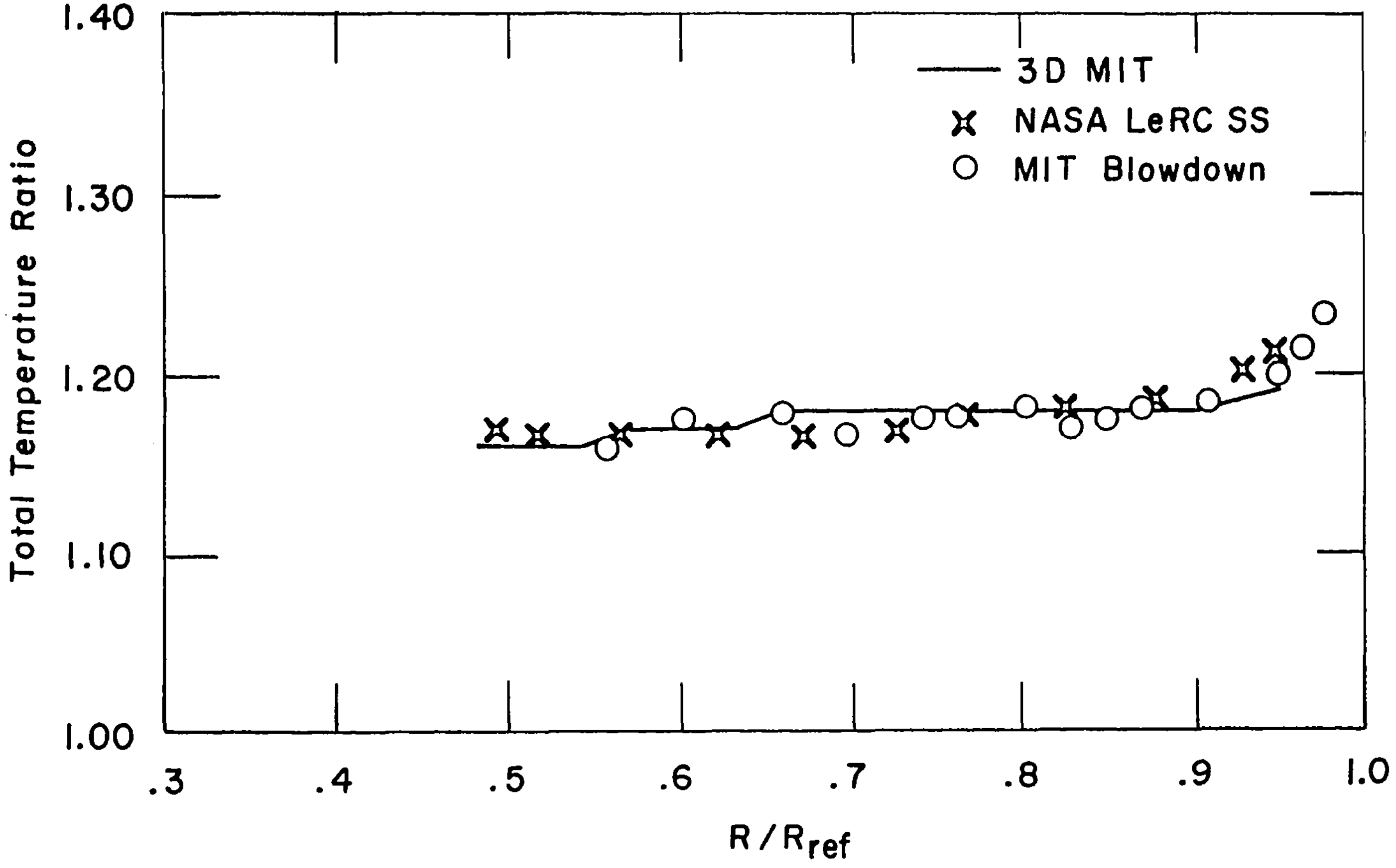

FIGURE 42 NASA LOW ASPECT RATIO ROTOR
TOTAL TEMPERATURE RATIO , THETA AVERAGED
ROTOR TRAILING EDGE

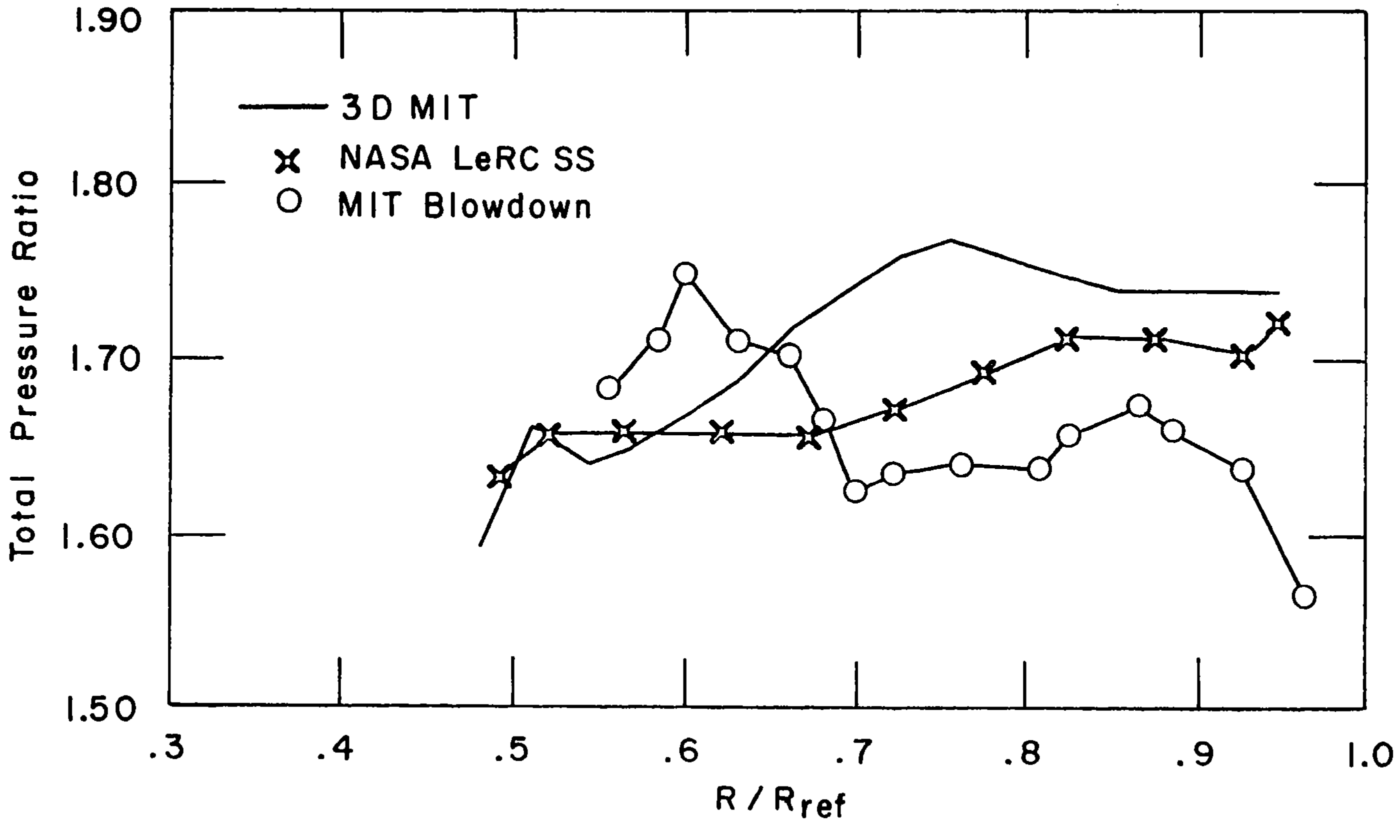

FIGURE 43 NASA LOW ASPECT RATIO ROTOR
TOTAL PRESSURE RATIO , THETA AVERAGED
ROTOR TRAILING EDGE

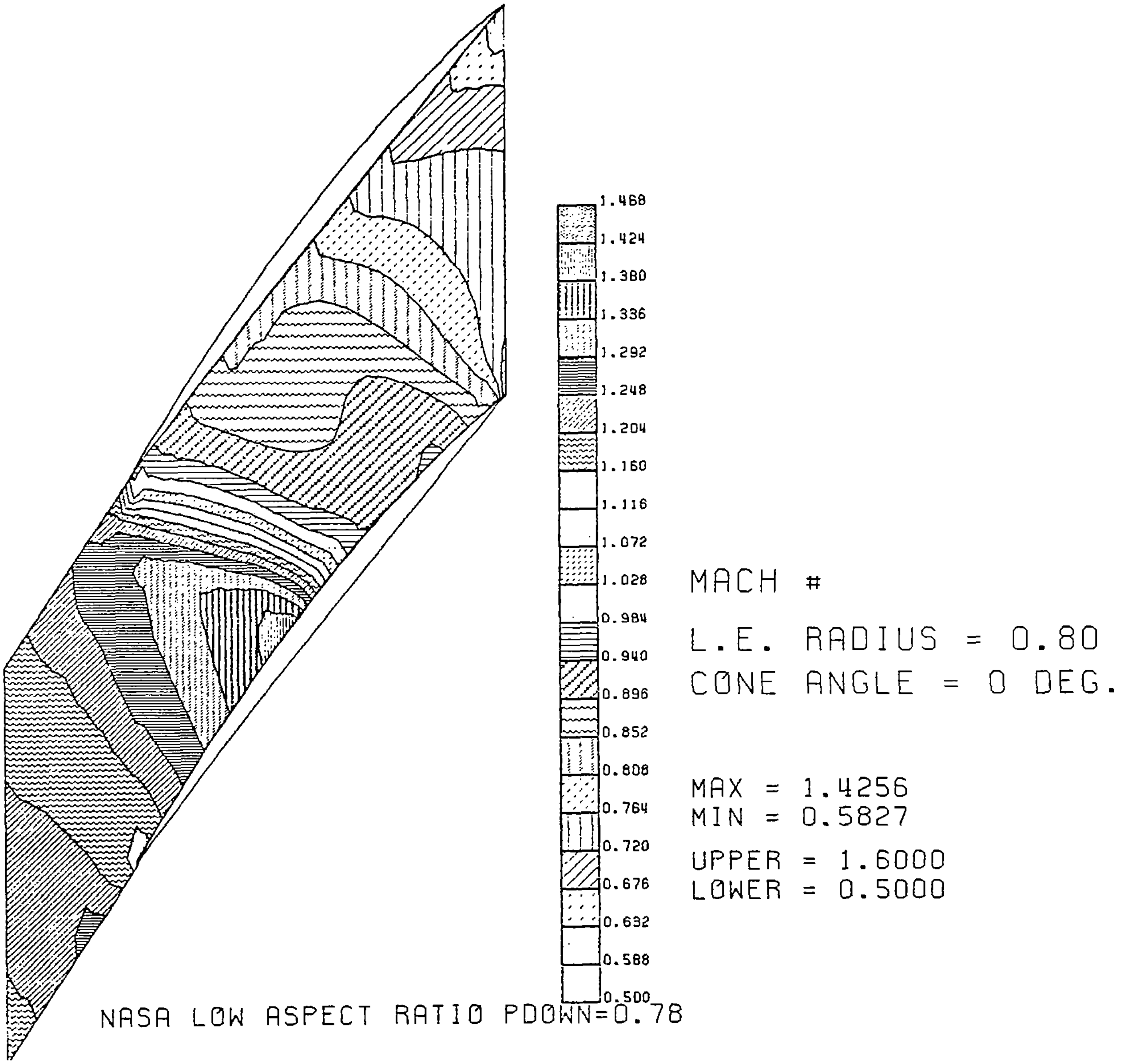

FIGURE 44 RELATIVE MACH NUMBER CONTOUR PLOT
CONSTANT RADIUS SURFACE

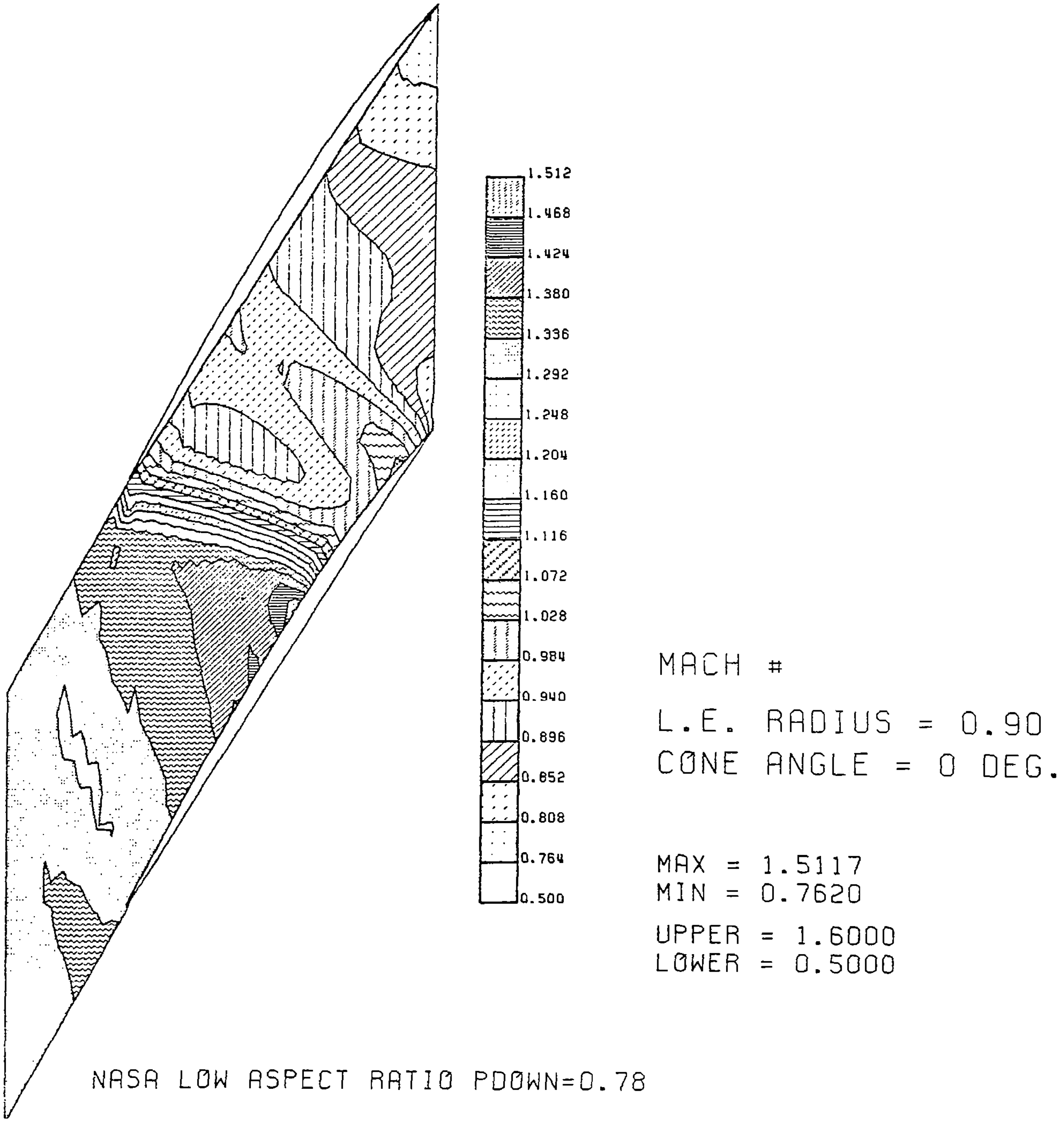

FIGURE 45 RELATIVE MACH NUMBER CONTOUR PLOT
CONSTANT RADIUS SURFACE

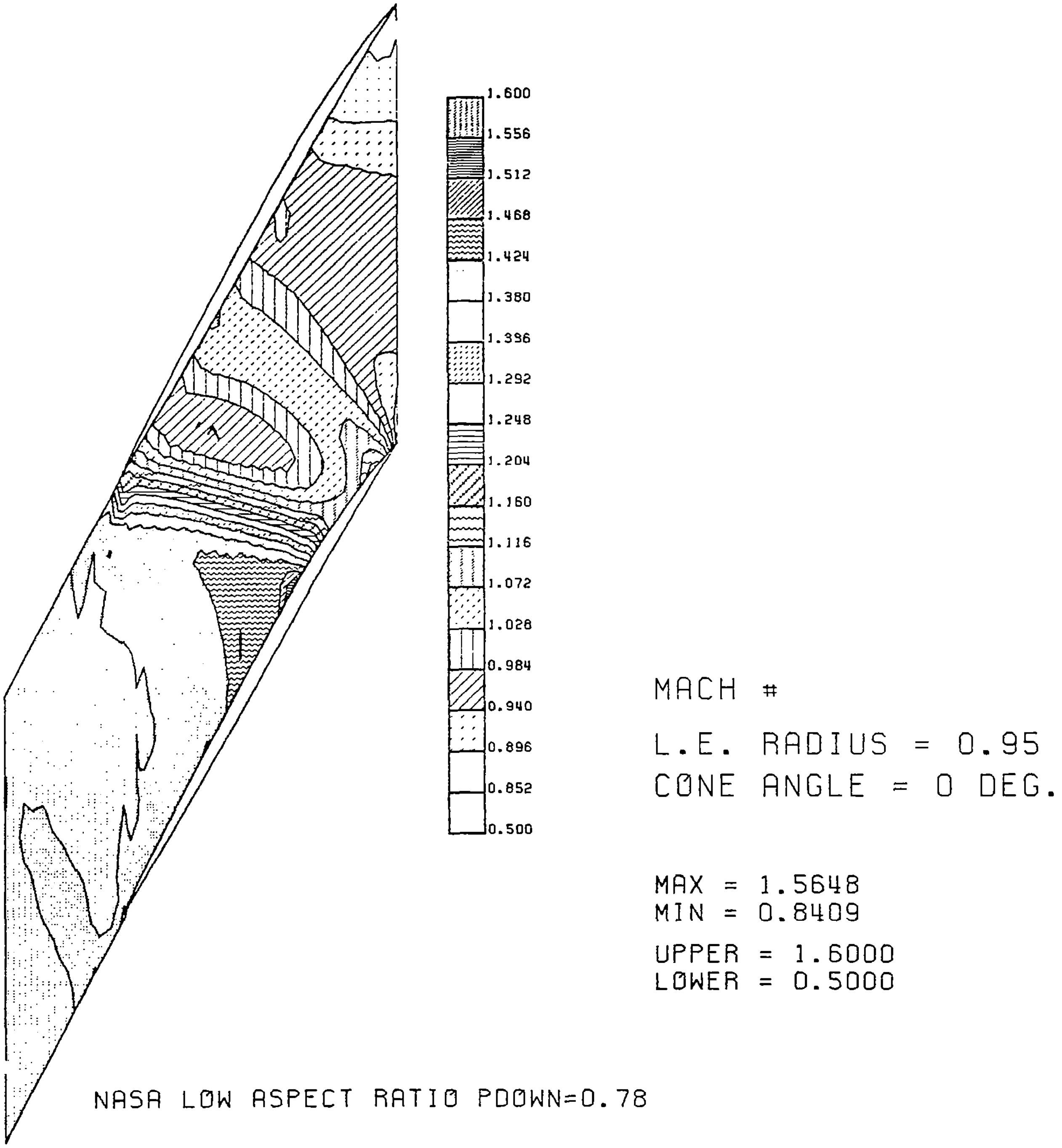

FIGURE 46 RELATIVE MACH NUMBER CONTOUR PLOT

CONSTANT RADIUS SURFACE

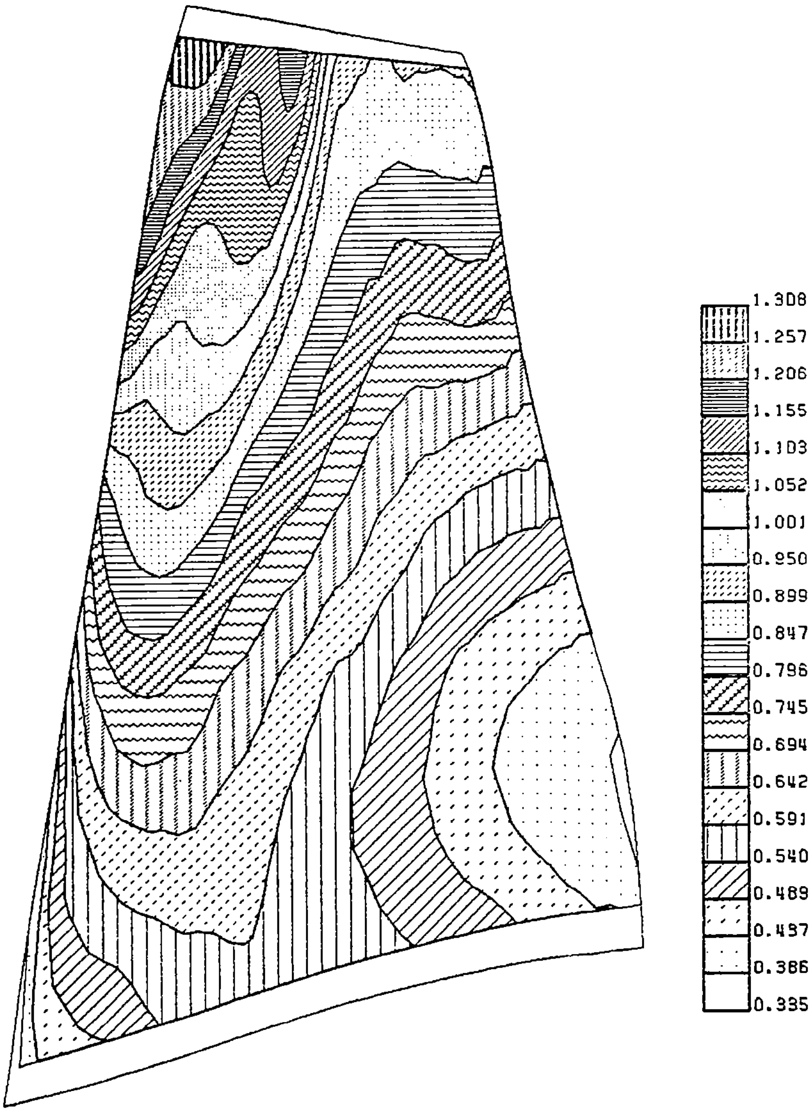

FIGURE 47 RELATIVE MACH NUMBER CONTOUR PLOT
BLADE PRESSURE SURFACE
NASA LOW ASPECT RATIO ROTOR

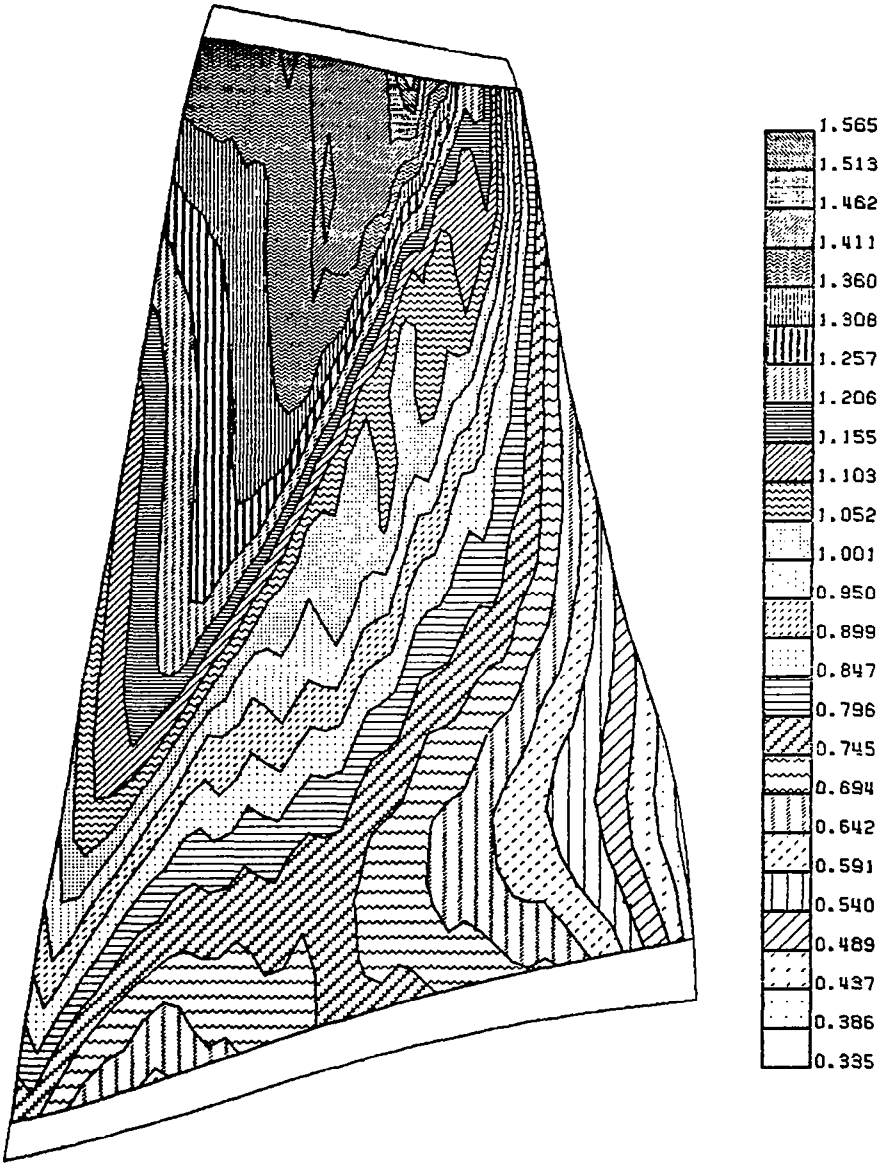

FIGURE 48 RELATIVE MACH NUMBER CONTOUR PLOT
BLADE SUCTION SURFACE
NASA LOW ASPECT RATIO ROTOR

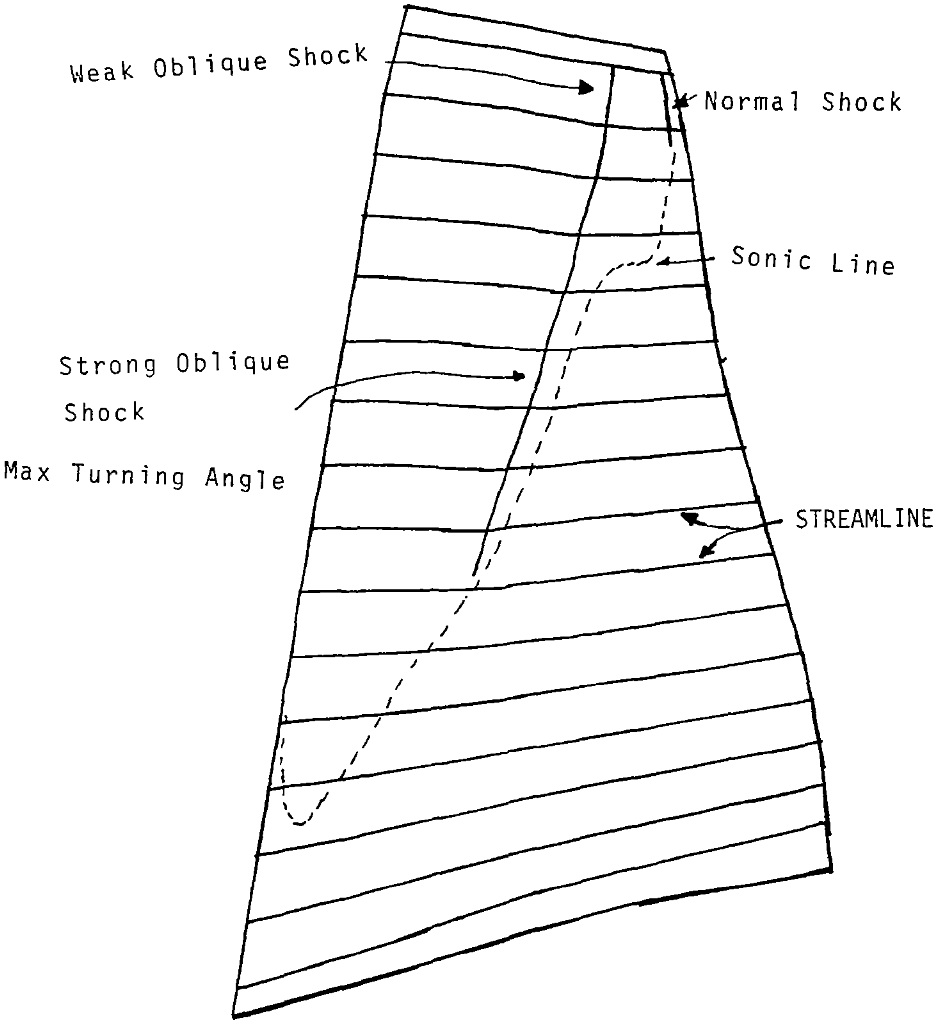

FIGURE 49 SUCTION SURFACE SHOCK STRUCTURE
NASA LOW ASPECT RATIO ROTOR

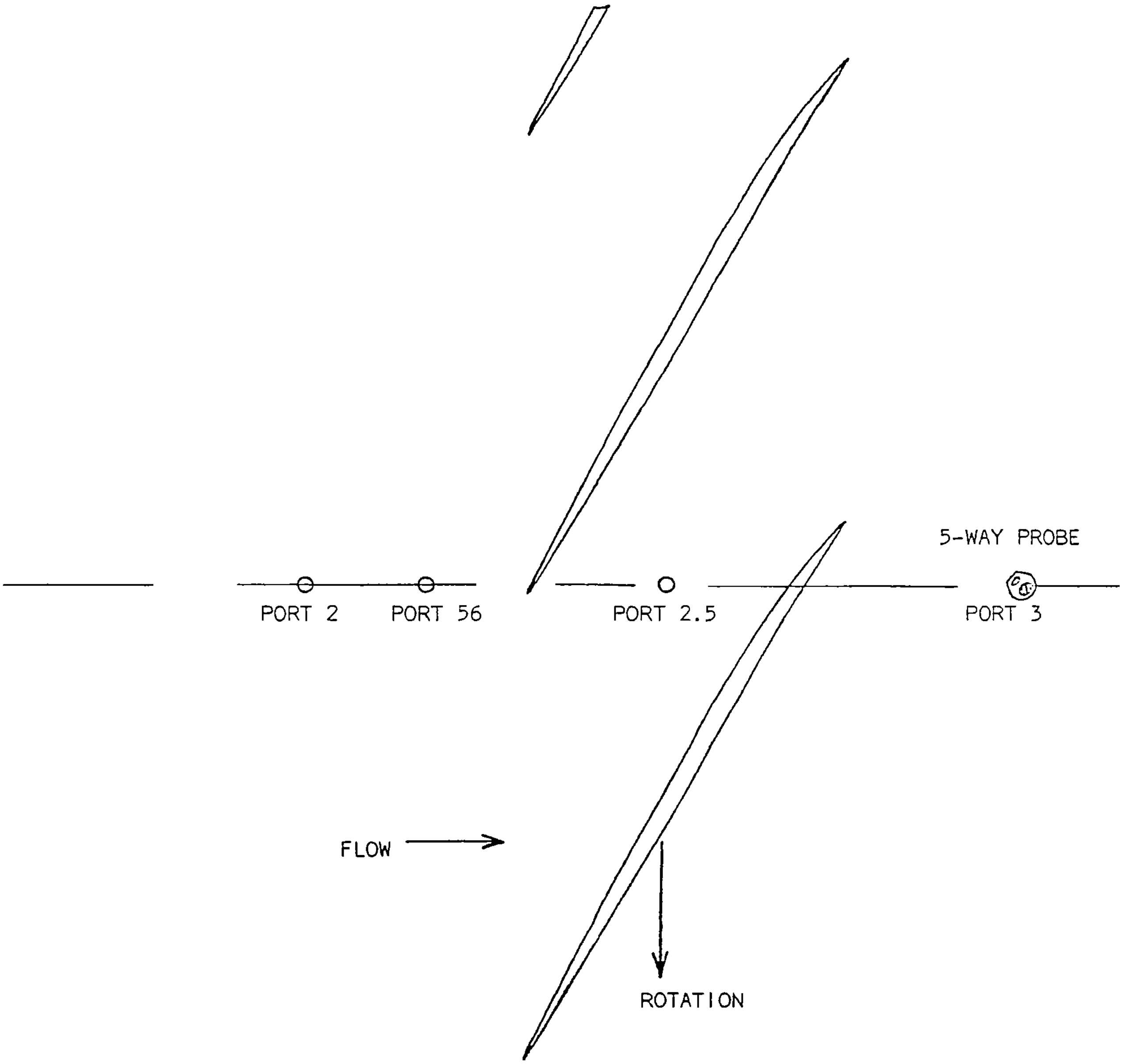

SCALE DRAWING OF ROTOR TIP SECTION & RELATIVE POSITION OF INSTRUMENTATION PORTS.

NASA LOW ASPECT RATIO ROTOR

FIGURE 50

PORT 2

AS MEASURED

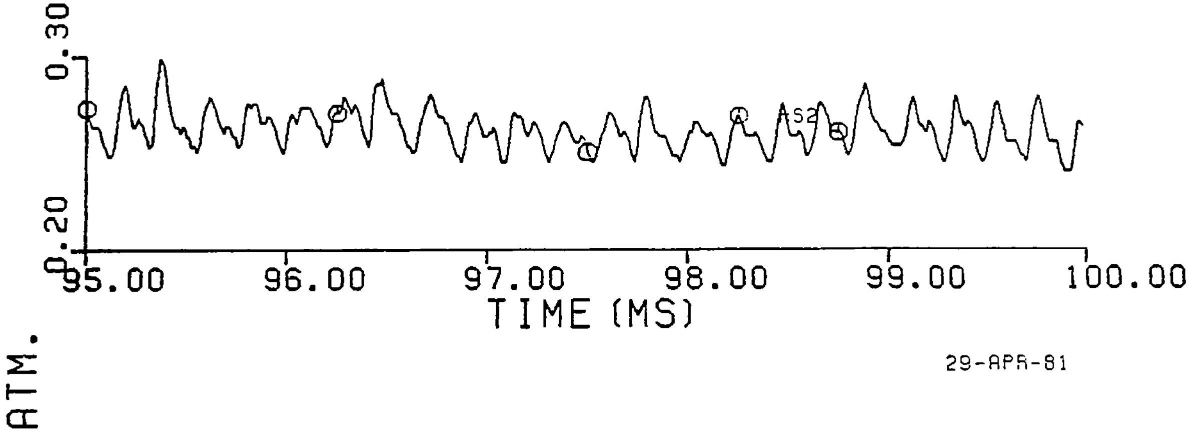

5 CYCLE BLADE PASSING PERIOD MOVING AVERAGE

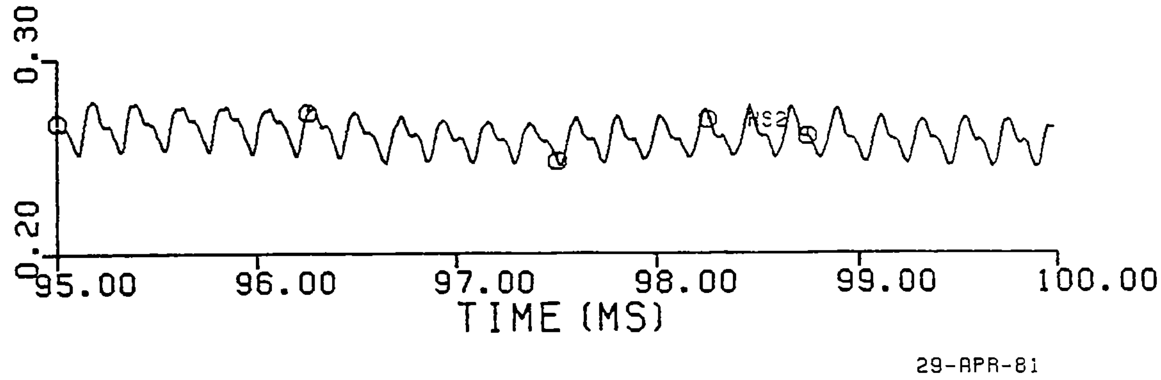

FIGURE 51 NASA LOW ASPECT RATIO ROTOR TEST
MEASURED WALL STATIC PRESSURE

PORT 56

AS MEASURED

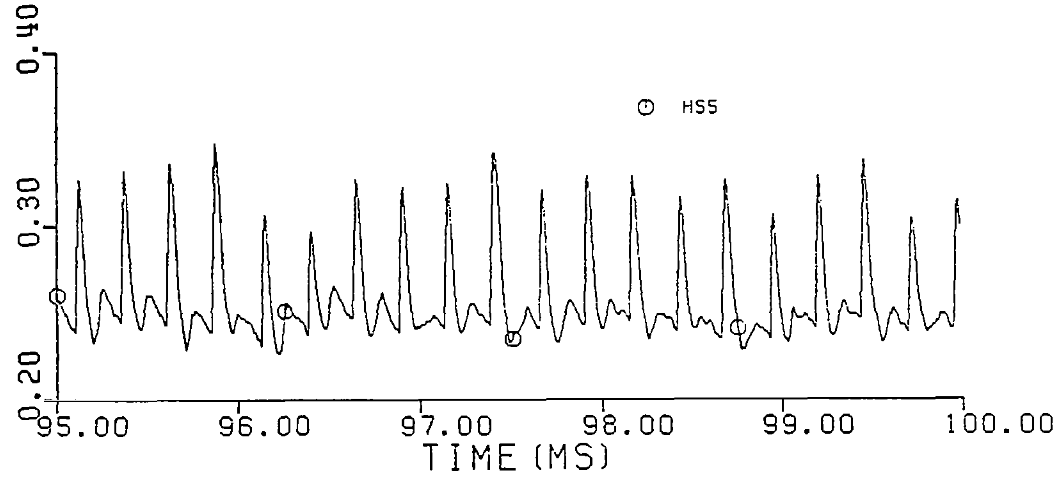

29-APR-81

5 CYCLE BLADE PASSING PERIOD

MOVING AVERAGE

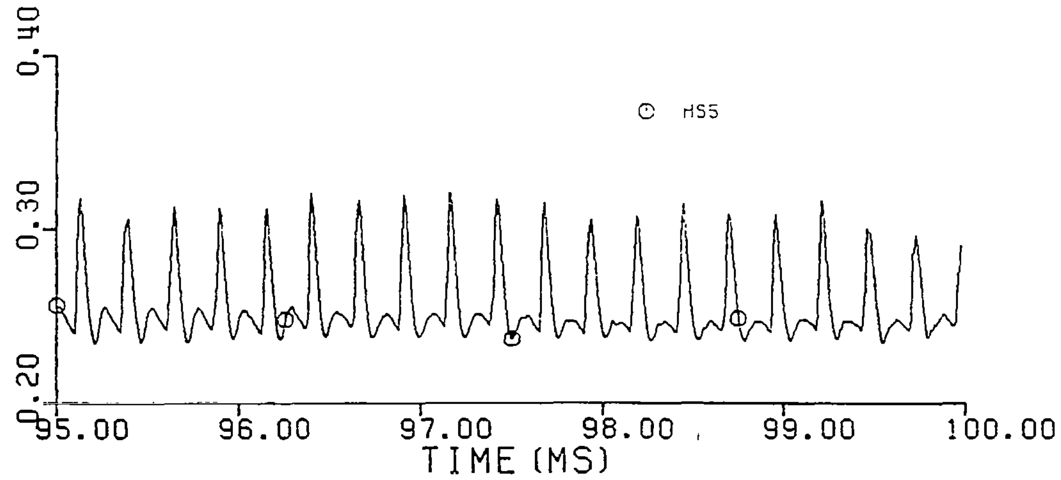

29-APR-81

FIGURE 52 NASA LOW ASPECT RATIO ROTOR
MEASURED WALL STATIC PRESSURE

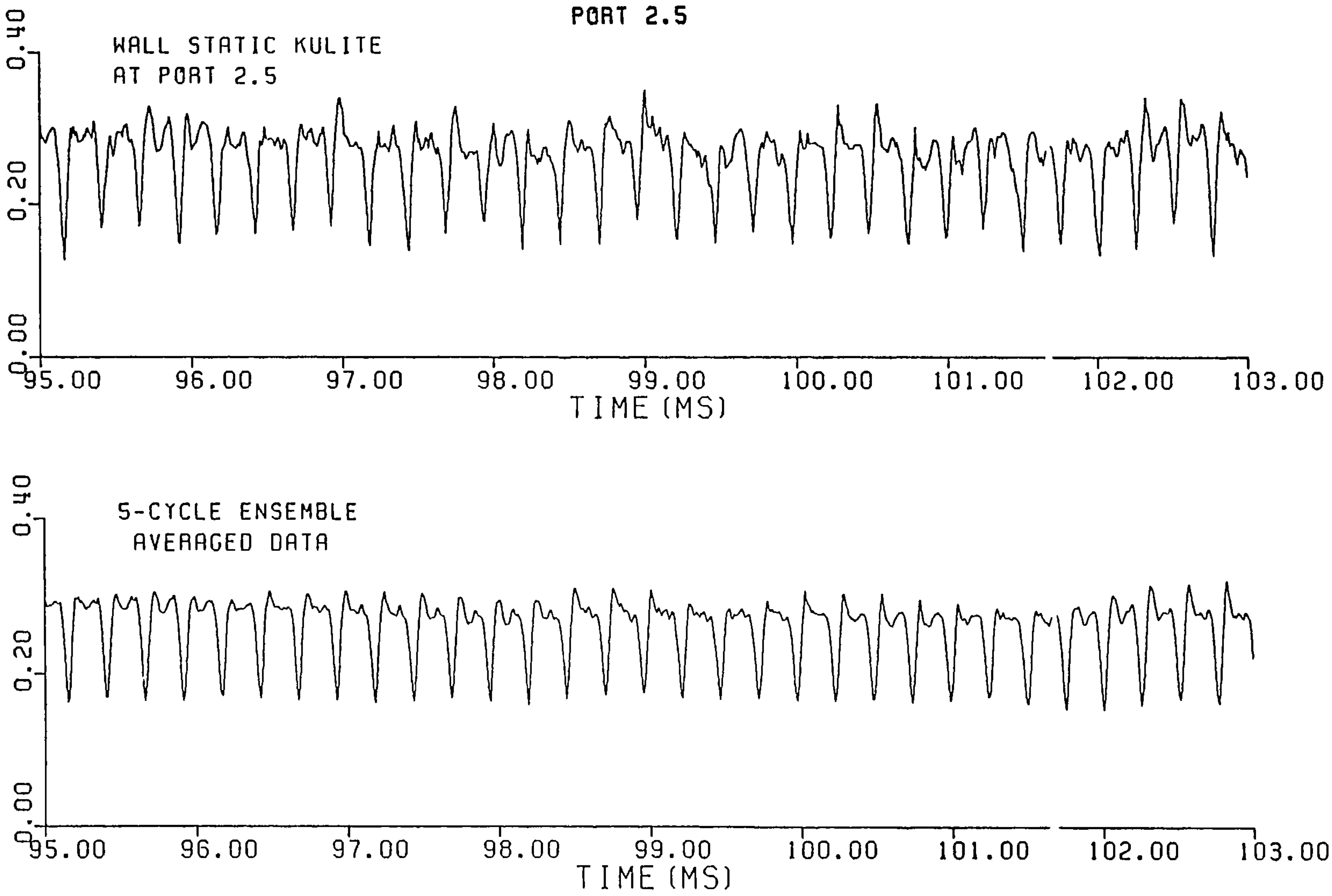

FIGURE 53 NASA LOW ASPECT RATIO ROTOR TEST

MEASURED WALL STATIC PRESSURE

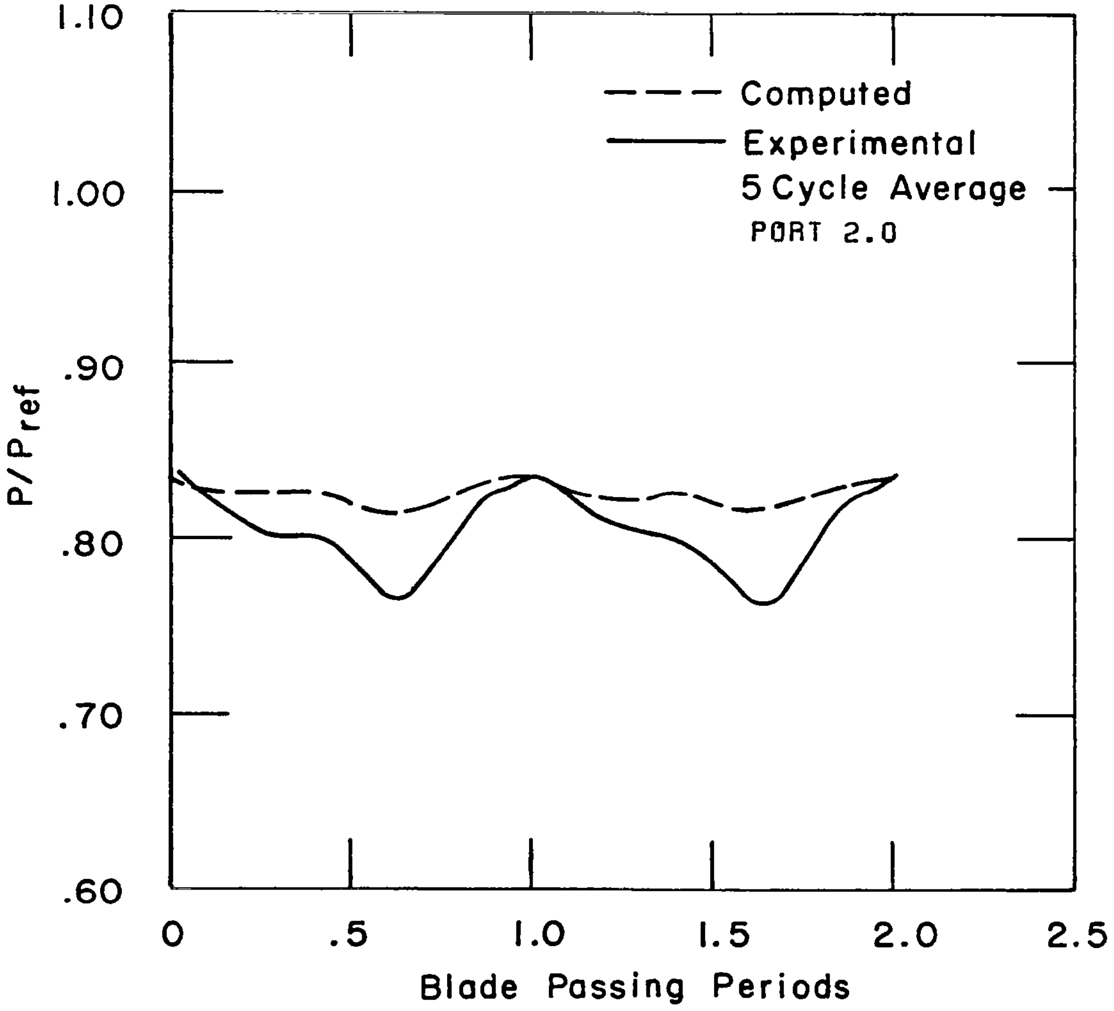

FIGURE 54 COMPARISON OF COMPUTED AND EXPERIMENTAL TIP WALL STATIC PRESSURE

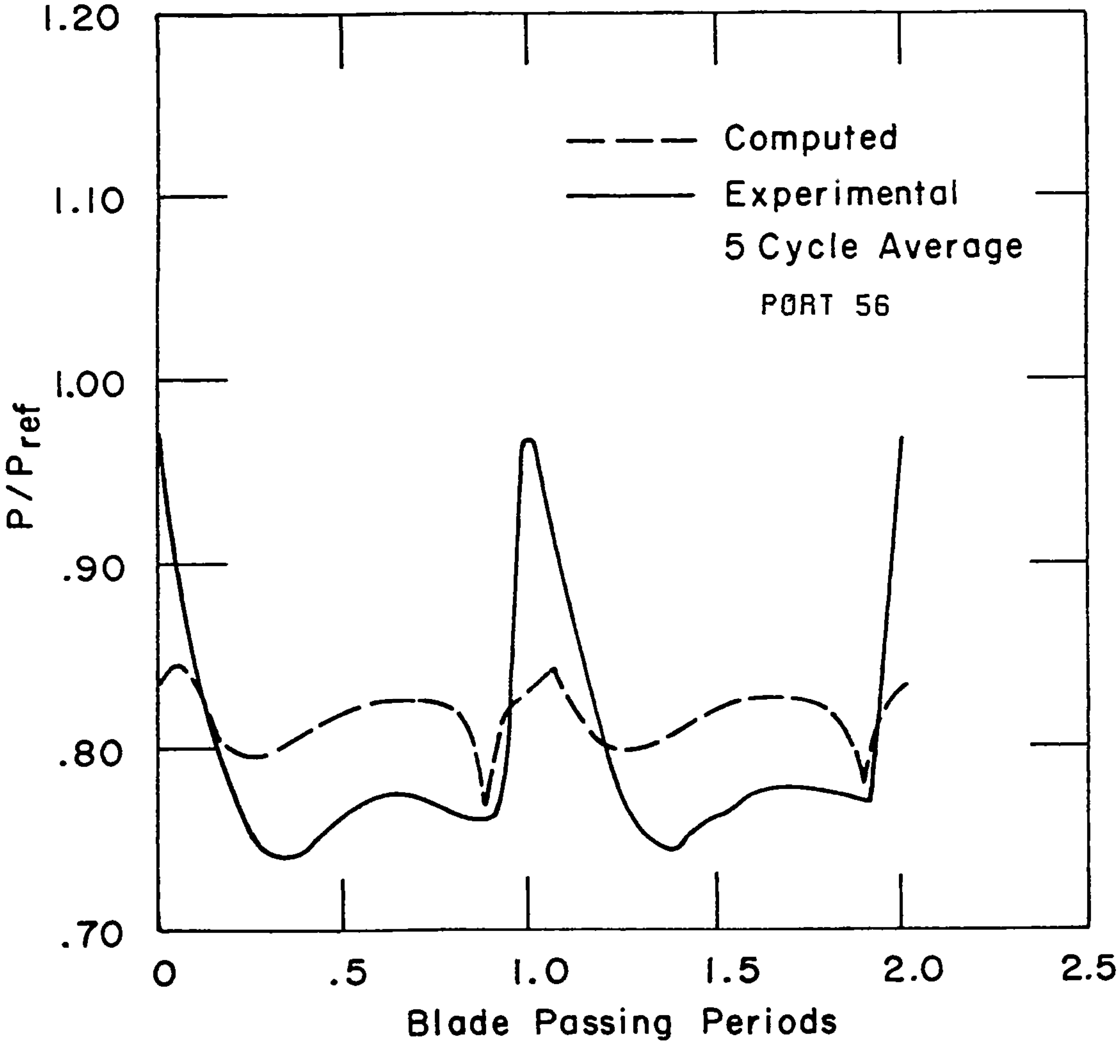

FIGURE 55 COMPARISON OF COMPUTED AND EXPERIMENTAL TIP WALL STATIC PRESSURE

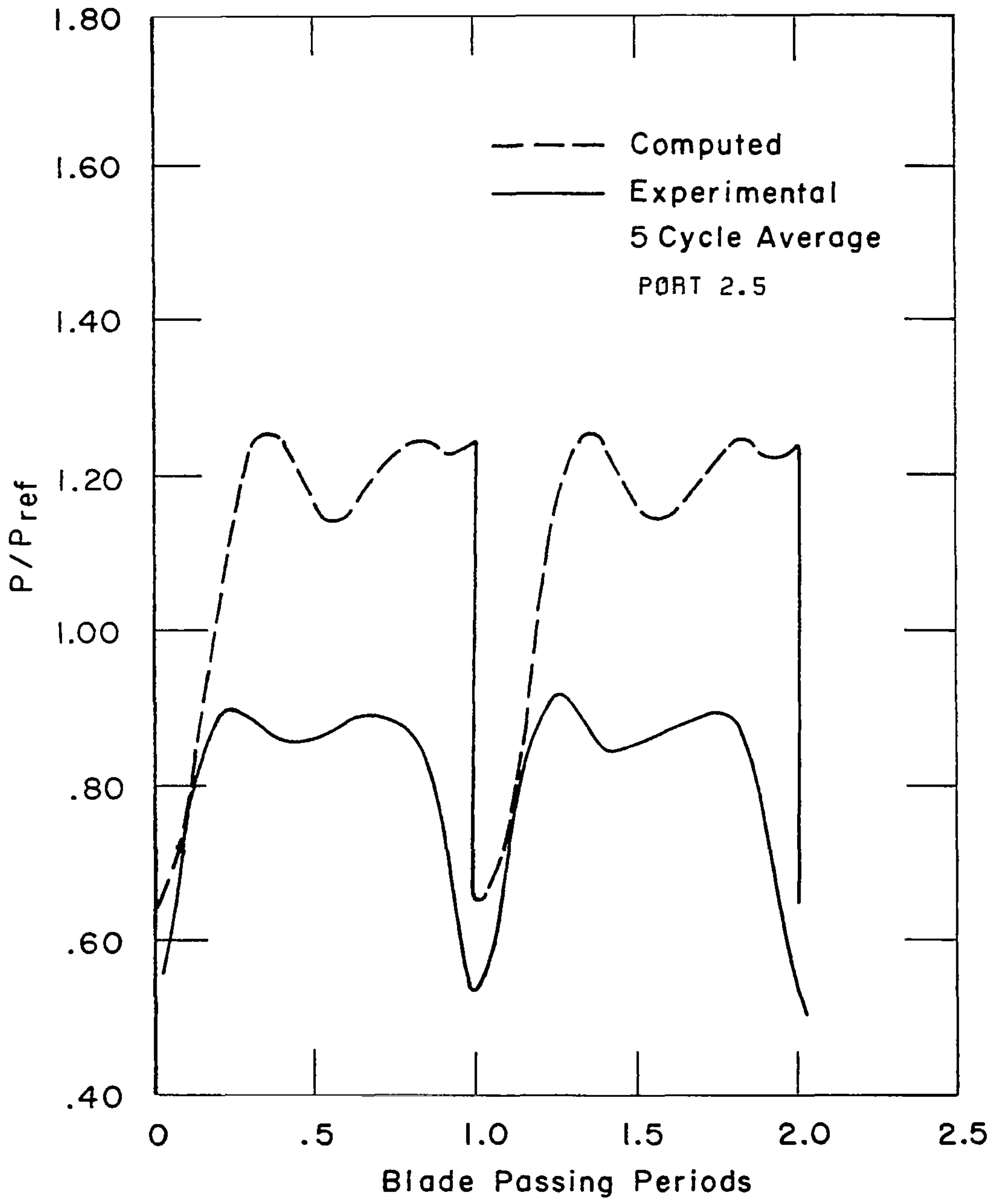

FIGURE 56 COMPARISON OF COMPUTED AND EXPERIMENTAL TIP WALL STATIC PRESSURE

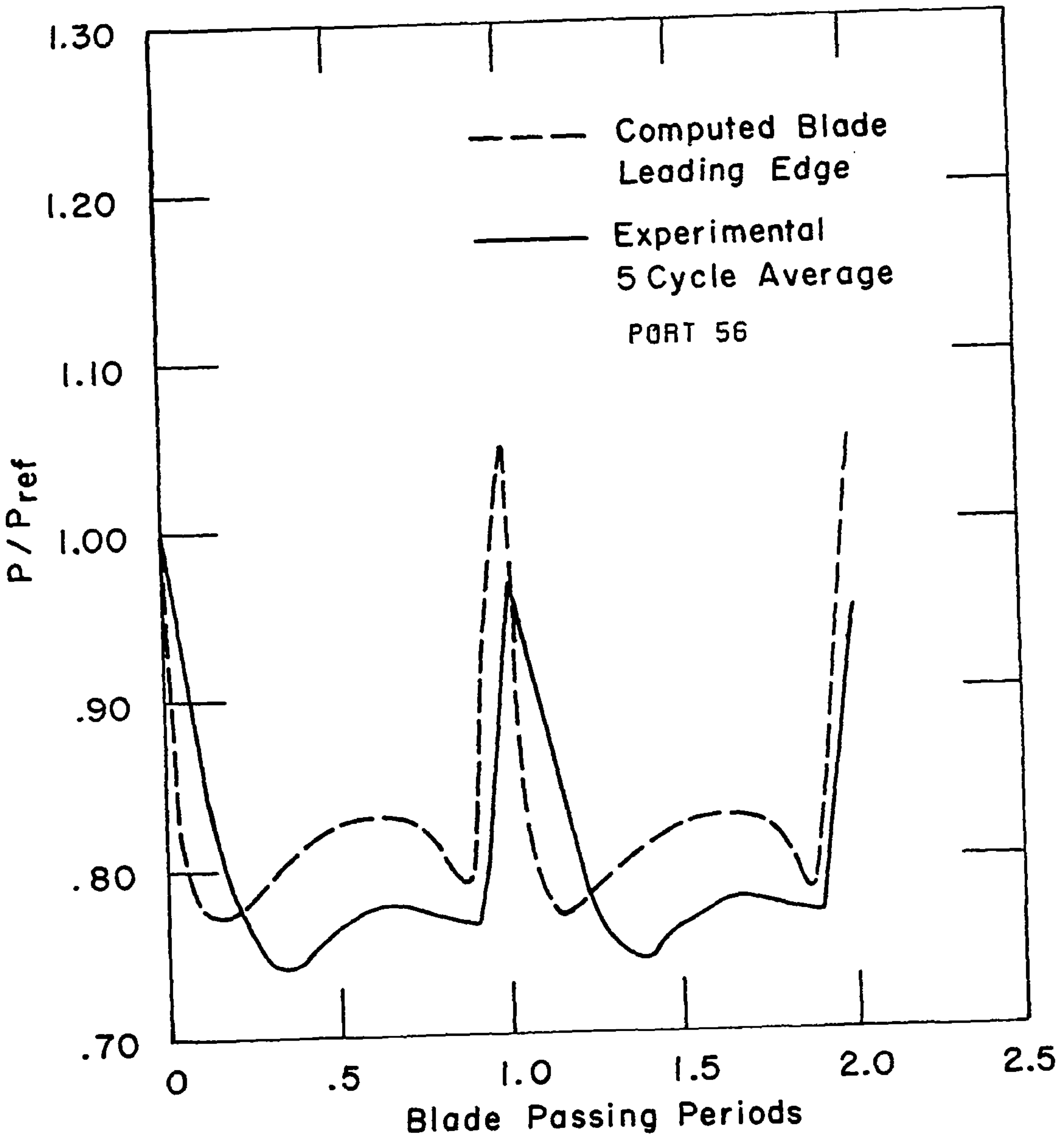

FIGURE 57 COMPARISON OF COMPUTED AND EXPERIMENTAL TIP WALL STATIC PRESSURE

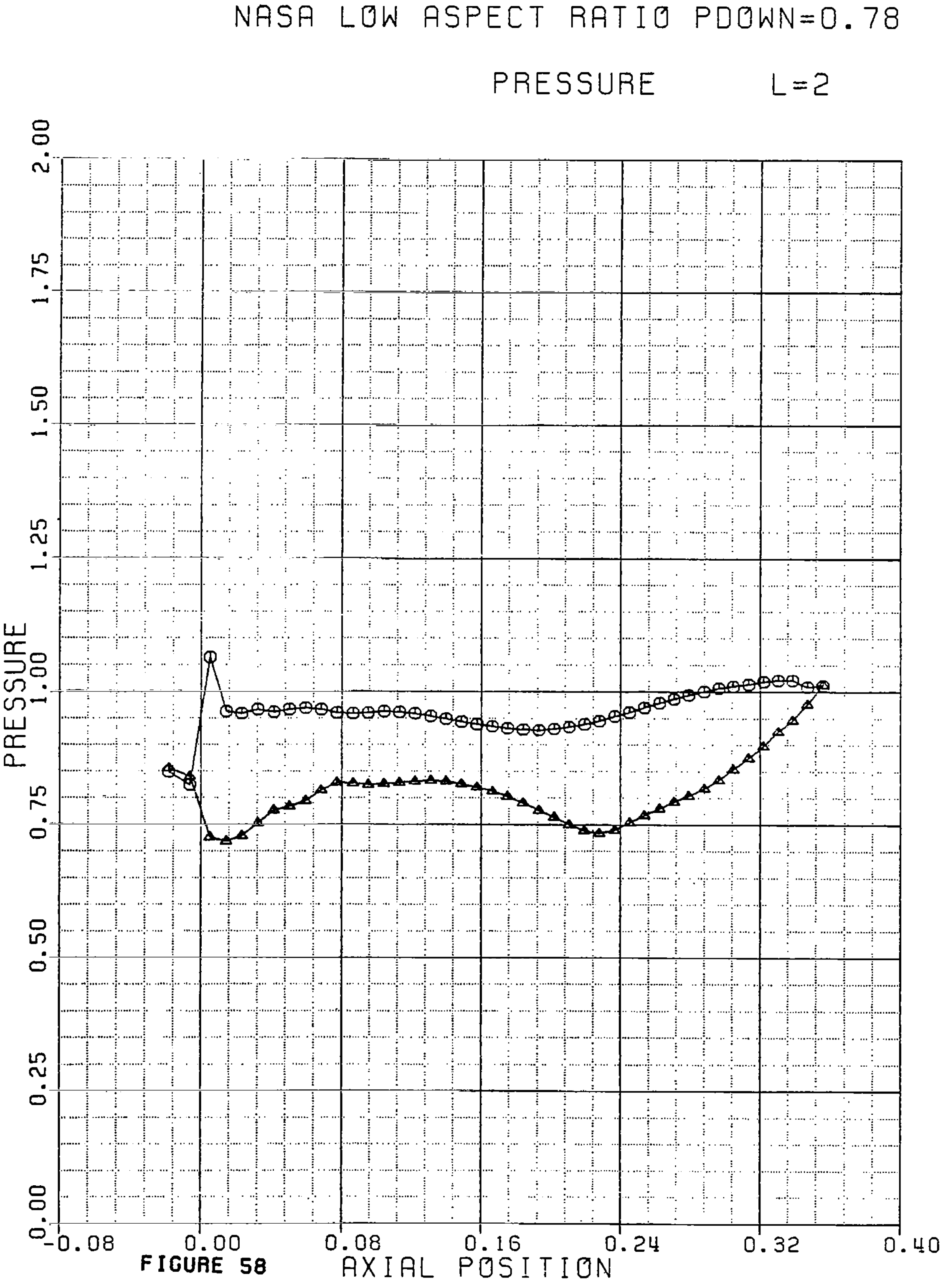
NASA LOW ASPECT RATIO PDOWN=0.78
PRESSURE L=2
PRESSURE
0.00
0.25
0.50
0.75
1.00
1.25
1.50
1.75
2.00
-0.08
0.00
0.08
0.16
0.24
0.32
0.40
AXIAL POSITION

FIGURE 58

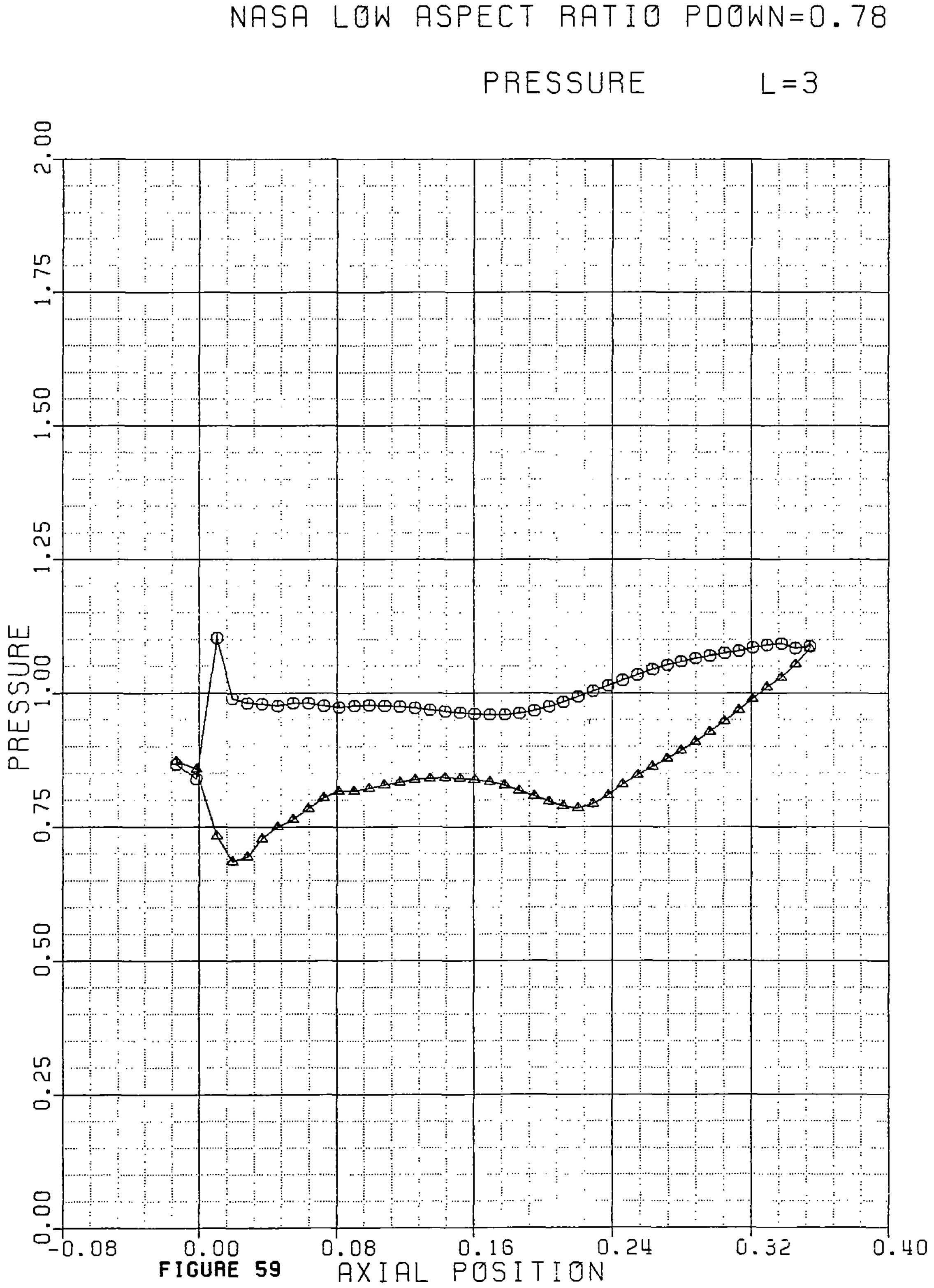
NASA LOW ASPECT RATIO PDOWN=0.78
PRESSURE L=3
PRESSURE
AXIAL POSITION
2.00
1.75
1.50
1.25
1.00
0.75
0.50
0.25
0.00
-0.08
0.00
0.08
0.16
0.24
0.32
0.40

FIGURE 59

NASA LOW ASPECT RATIO PDOWN=0.78

PRESSURE L=4

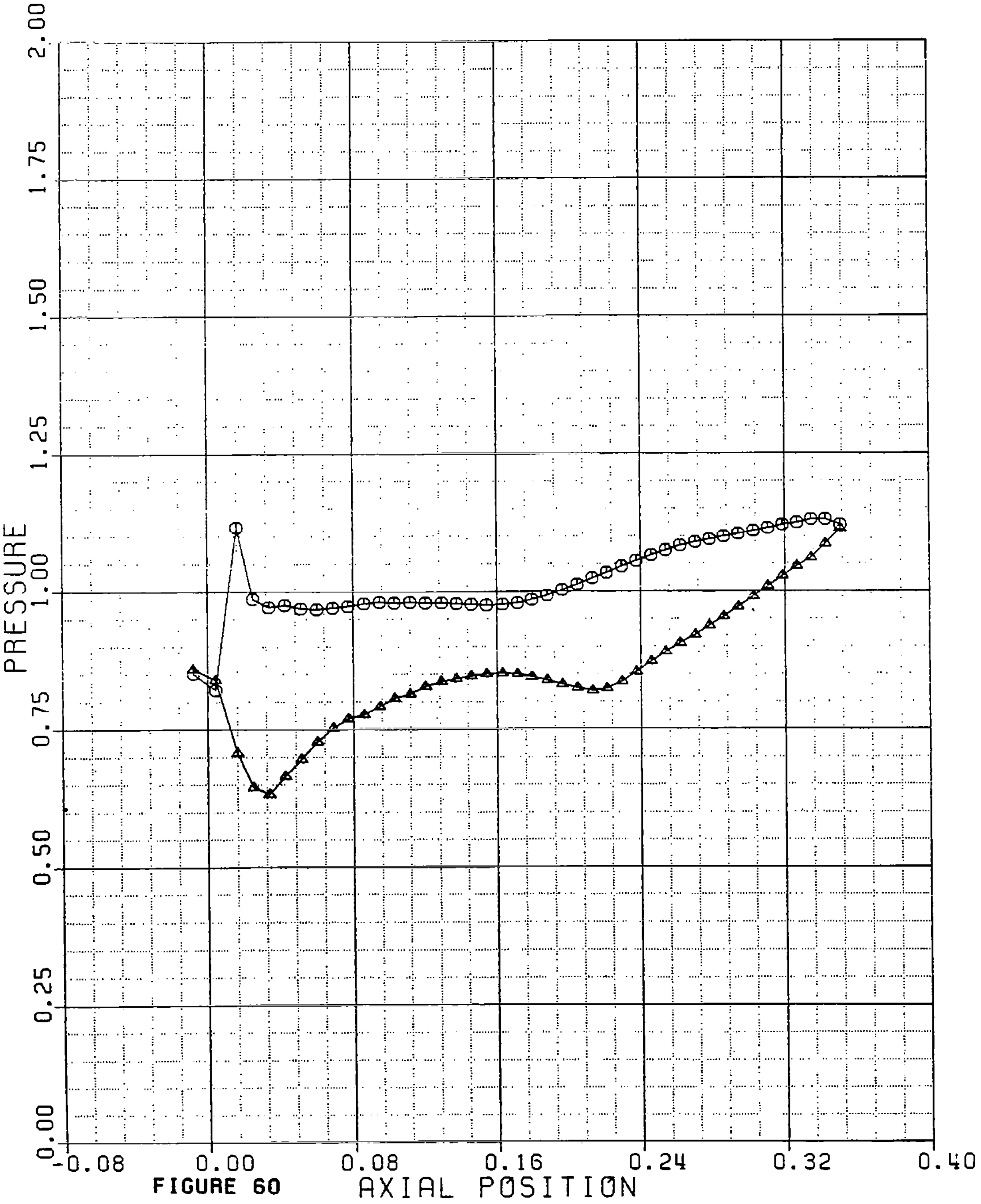

FIGURE 60

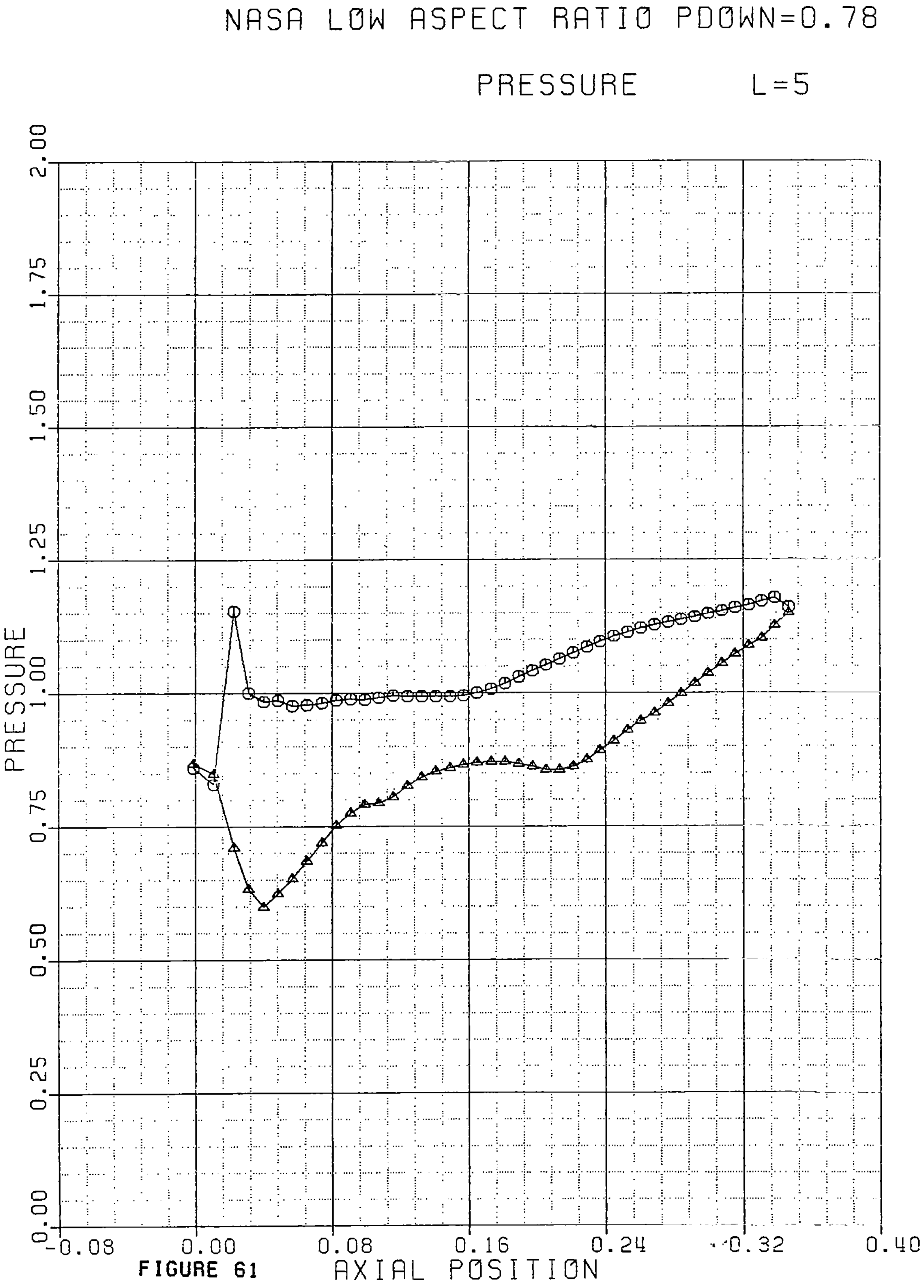
NASA LOW ASPECT RATIO PDOWN=0.78
PRESSURE L=5
PRESSURE
2.00
1.75
1.50
1.25
1.00
0.75
0.50
0.25
0.00
-0.08
0.00
0.08
0.16
0.24
0.32
0.40
AXIAL POSITION

FIGURE 61

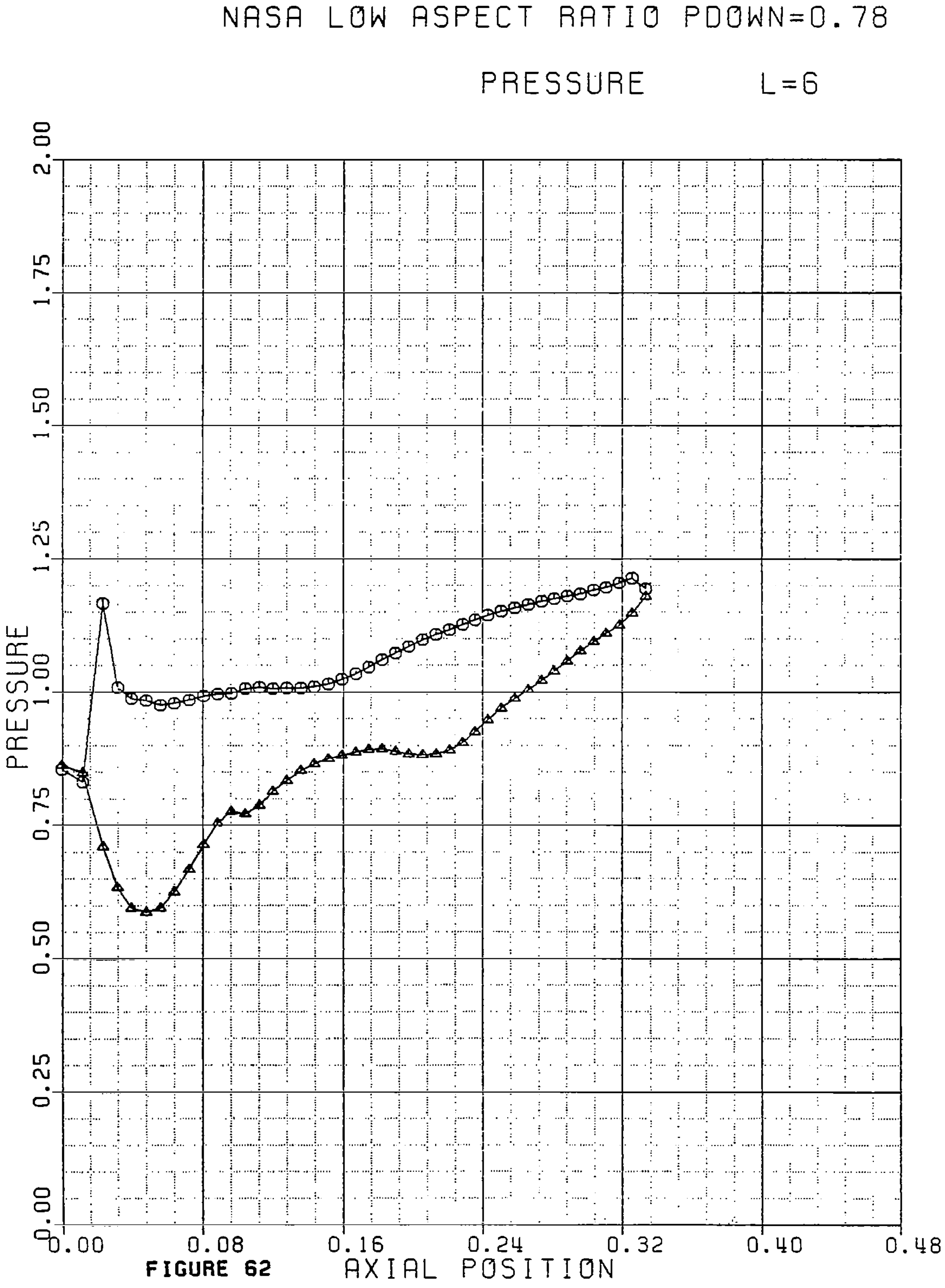
NASA LOW ASPECT RATIO PDOWN=0.78
PRESSURE L=6
PRESSURE
2.00
1.75
1.50
1.25
1.00
0.75
0.50
0.25
0.00
0.00
0.08
0.16
0.24
0.32
0.40
0.48
AXIAL POSITION

FIGURE 62

NASA LOW ASPECT RATIO PDOWN=0.78

PRESSURE L=7

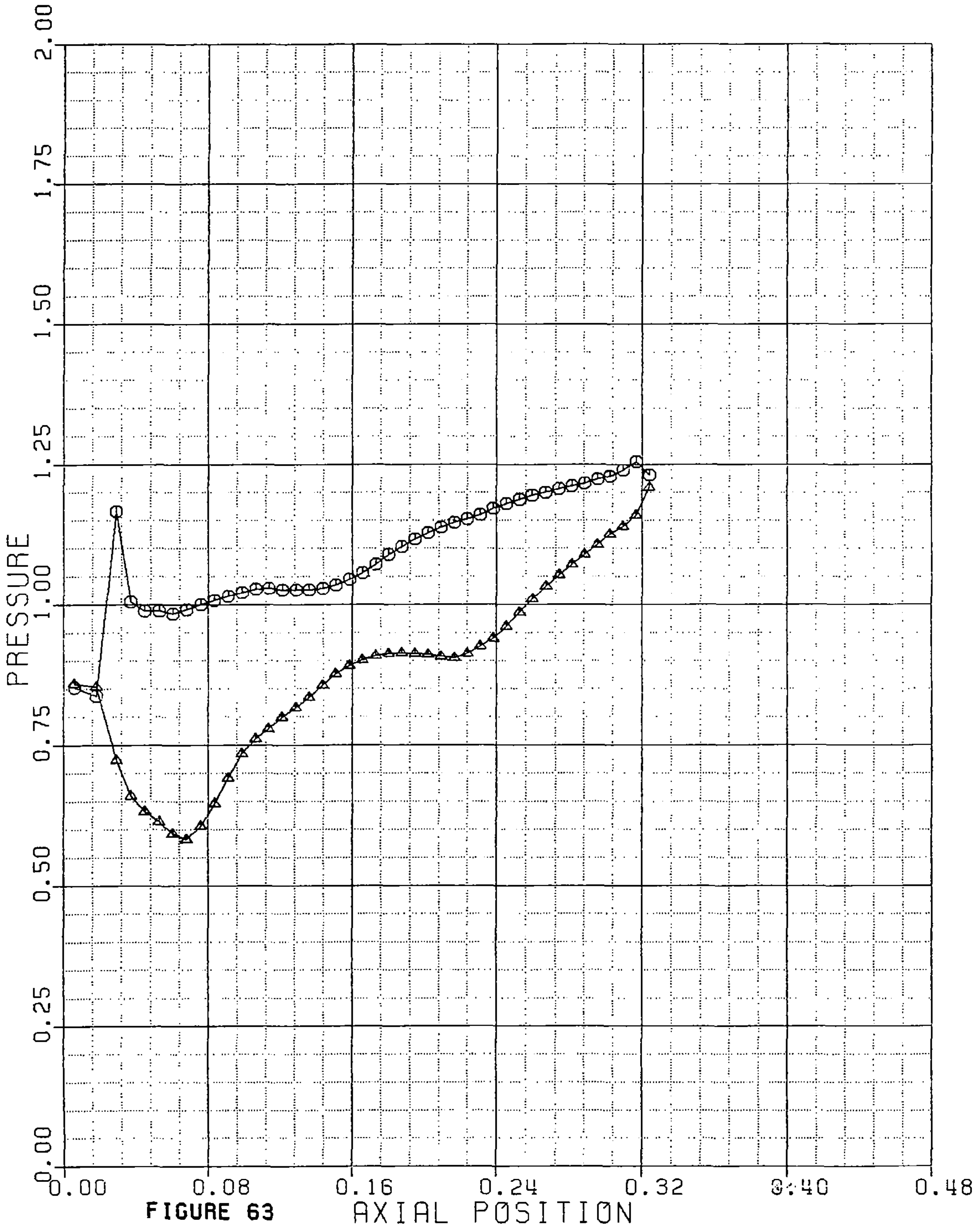

FIGURE 63

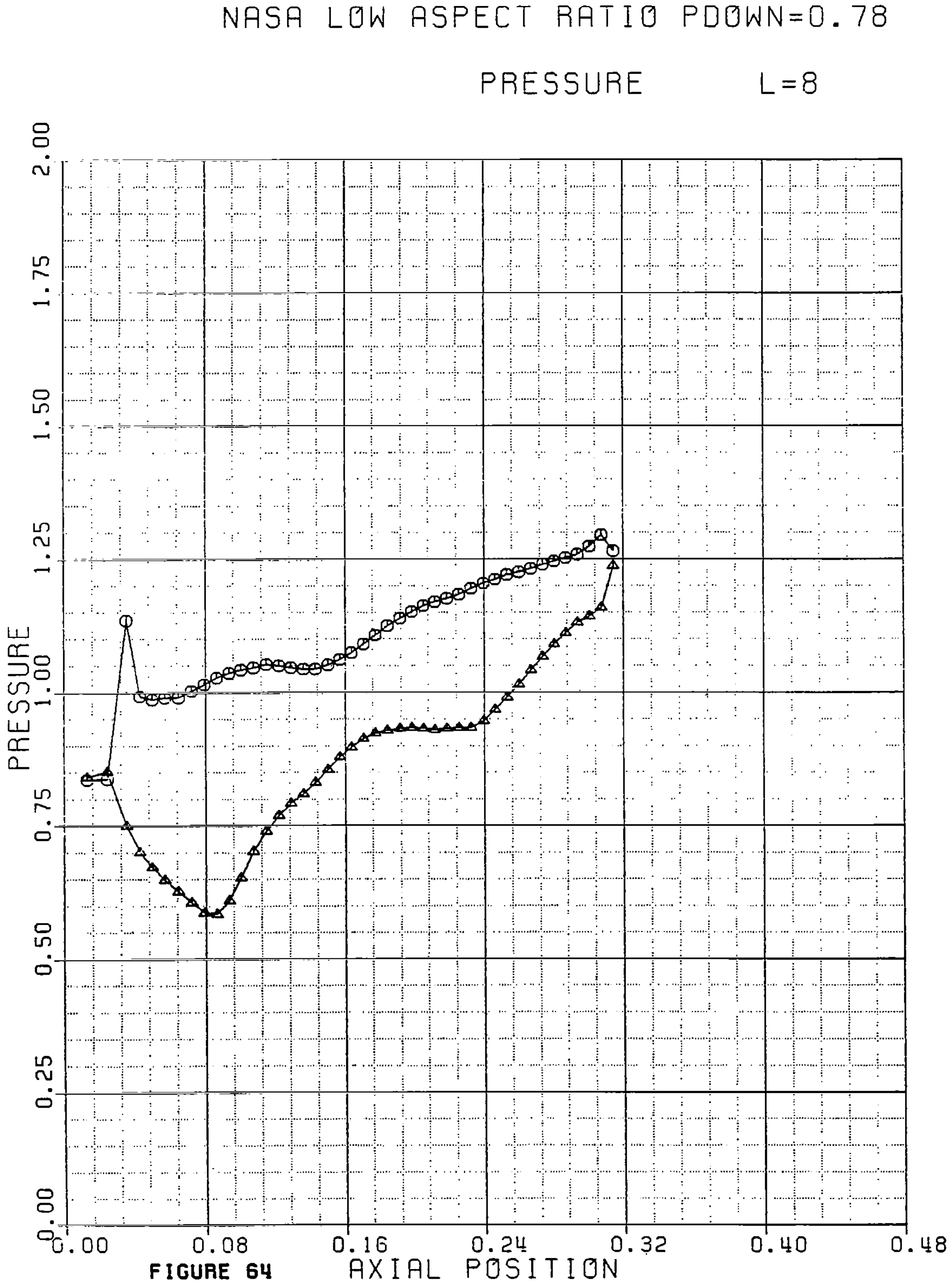
NASA LOW ASPECT RATIO PDOWN=0.78
PRESSURE L=8
PRESSURE
2.00
1.75
1.50
1.25
1.00
0.75
0.50
0.25
0.00
0.00
0.08
0.16
0.24
0.32
0.40
0.48
AXIAL POSITION

FIGURE 64

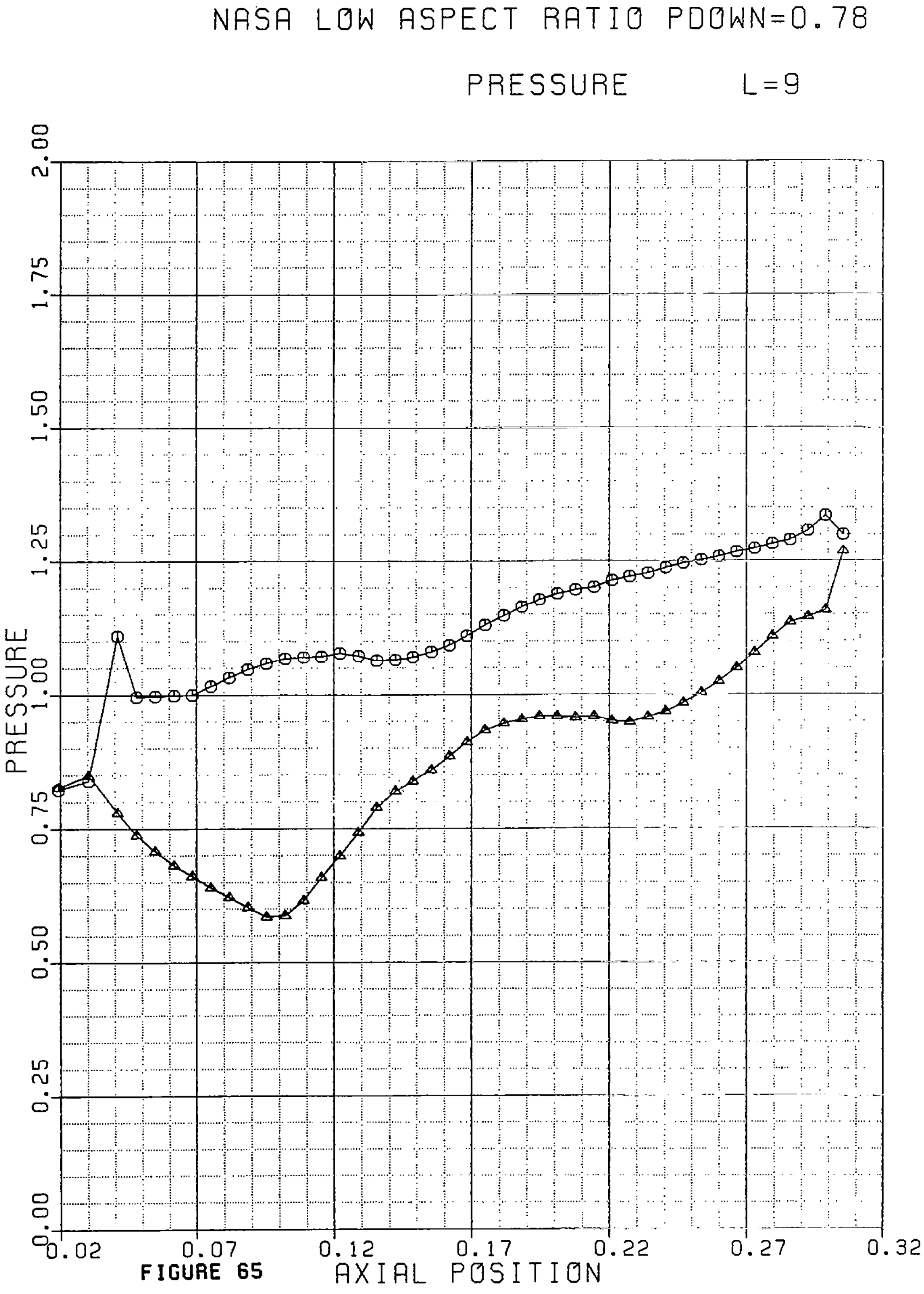
NASA LOW ASPECT RATIO PDOWN=0.78
PRESSURE L=9
PRESSURE
0.00
0.25
0.50
0.75
1.00
1.25
1.50
1.75
2.00
0.02
0.07
0.12
0.17
0.22
0.27
0.32
AXIAL POSITION

FIGURE 65

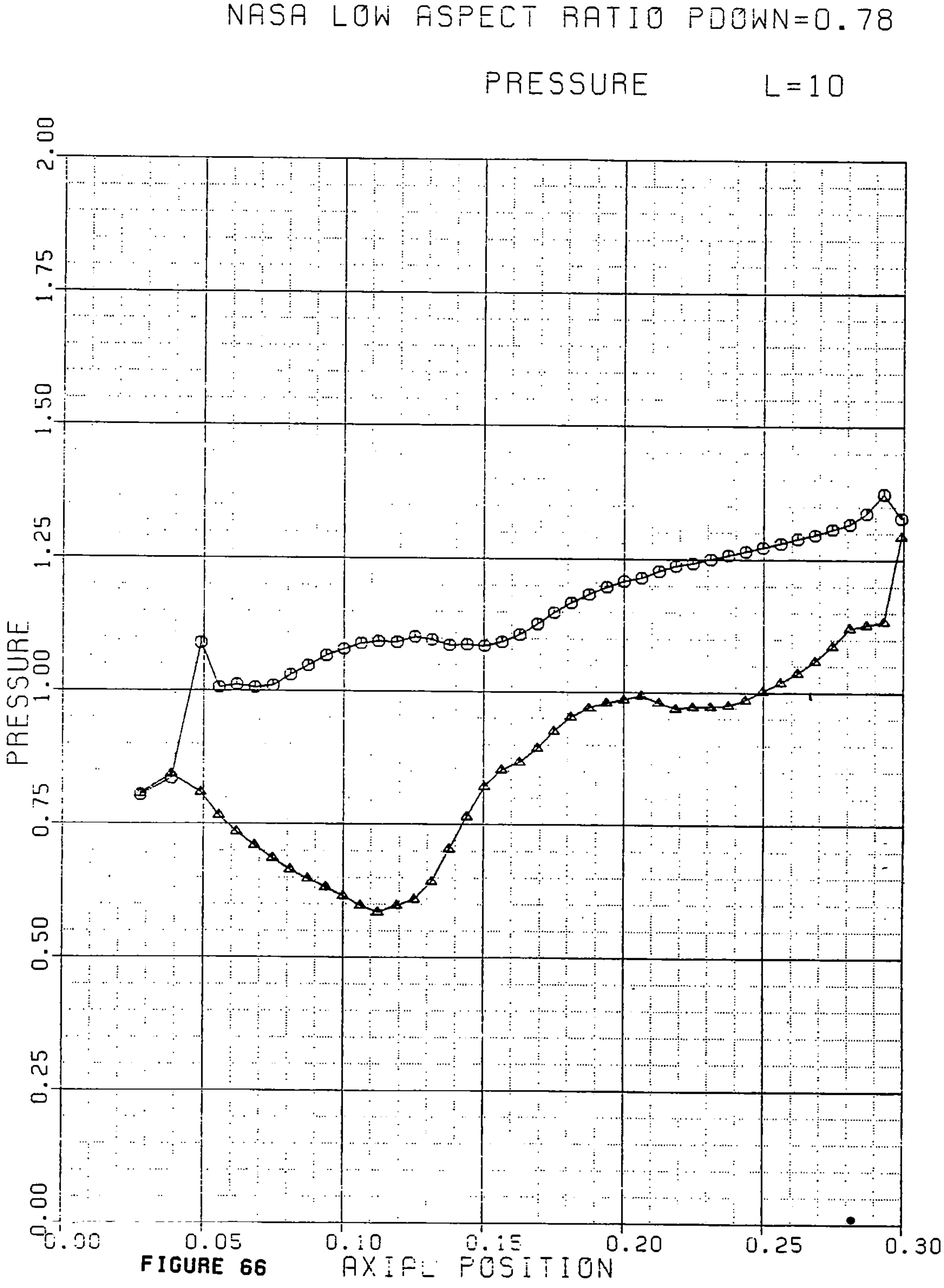
NASA LOW ASPECT RATIO PDOWN=0.78
PRESSURE L=10
PRESSURE
0.00
0.25
0.50
0.75
1.00
1.25
1.50
1.75
2.00
0.00
0.05
0.10
0.15
0.20
0.25
0.30
AXIAL POSITION

FIGURE 66

NASA LOW ASPECT RATIO PDOWN=0.78

PRESSURE L=11

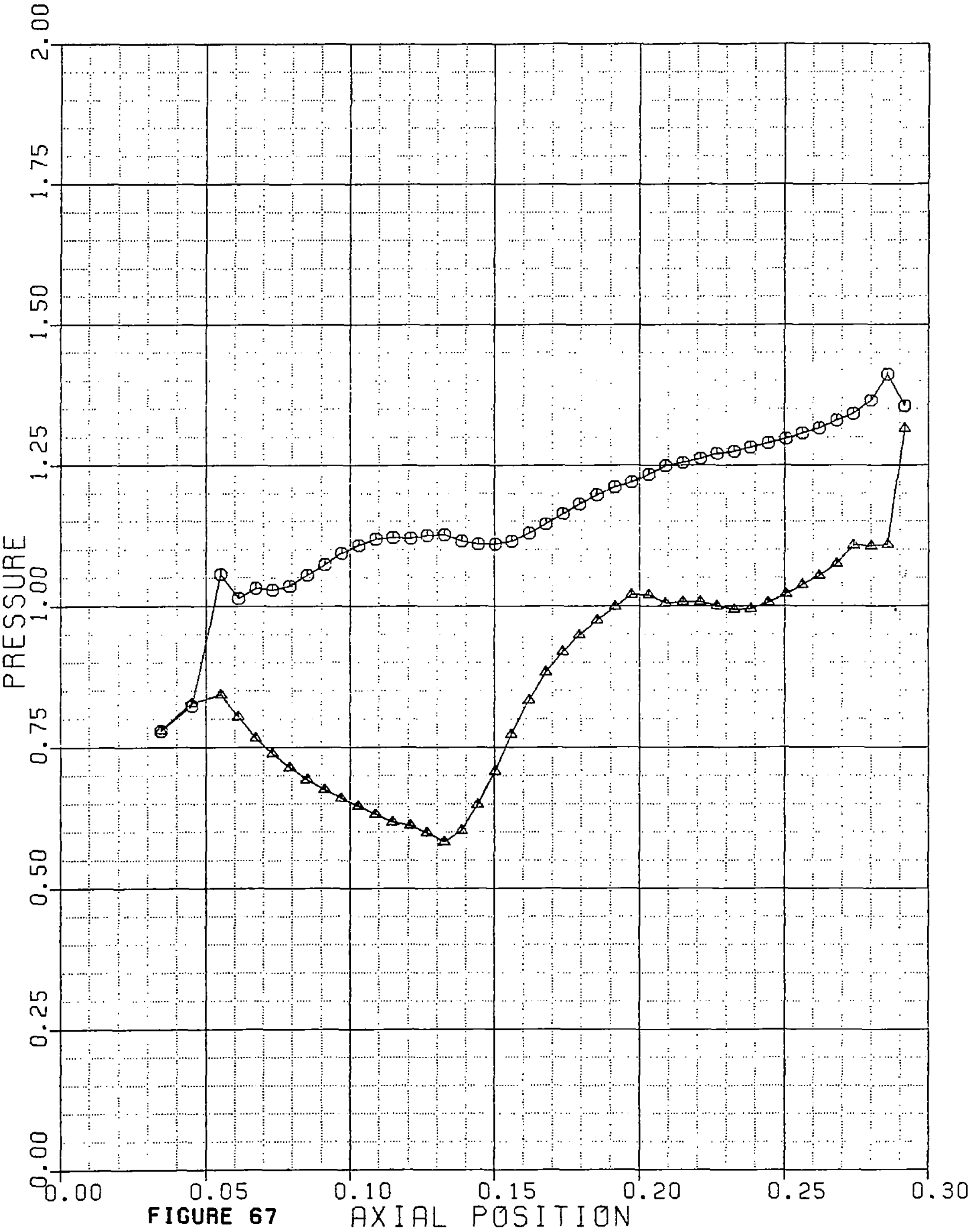

FIGURE 67

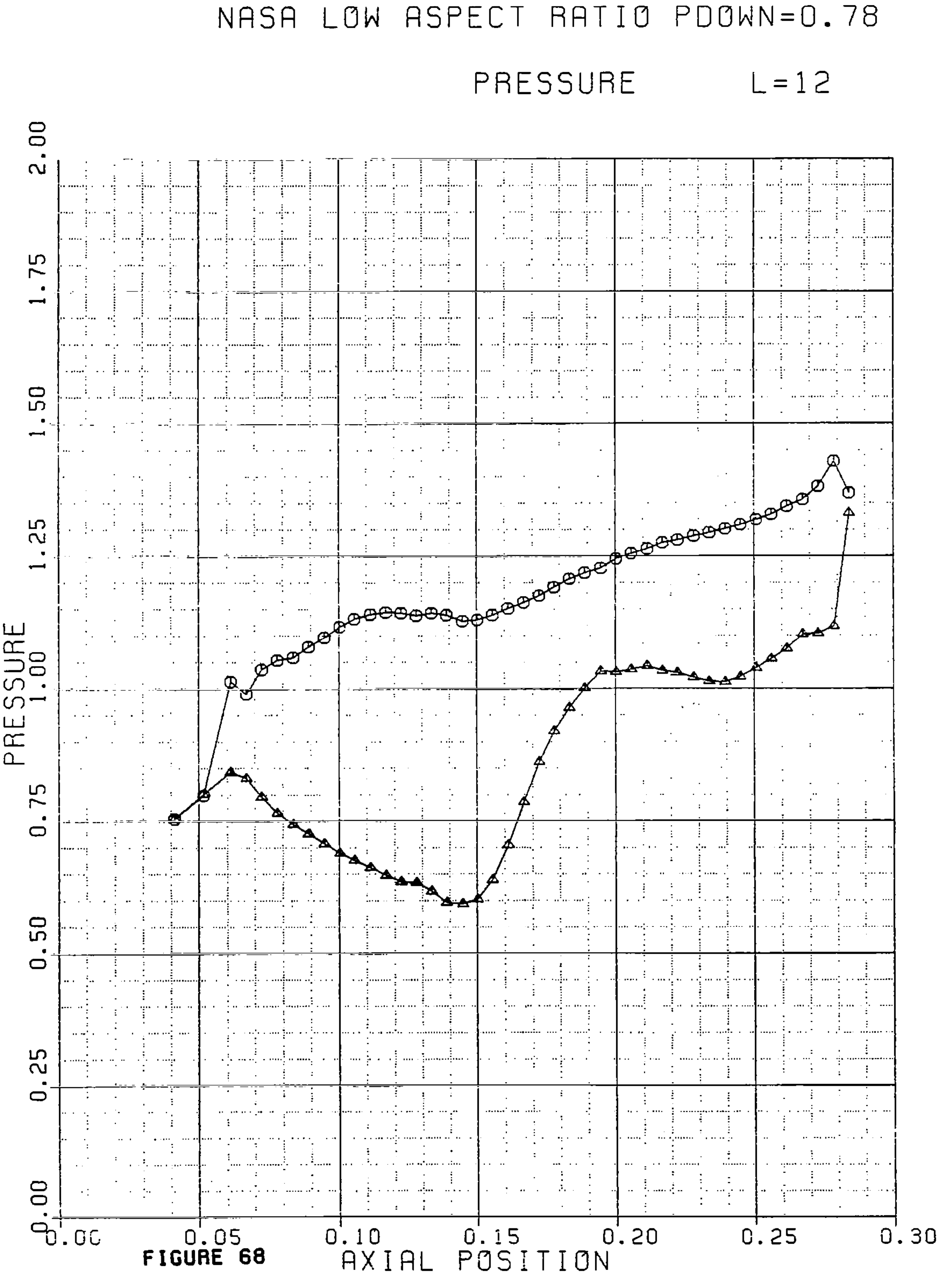
NASA LOW ASPECT RATIO PDOWN=0.78
PRESSURE L=12
PRESSURE
0.00
0.25
0.50
0.75
1.00
1.25
1.50
1.75
2.00
0.00
0.05
0.10
0.15
0.20
0.25
0.30
AXIAL POSITION

FIGURE 68

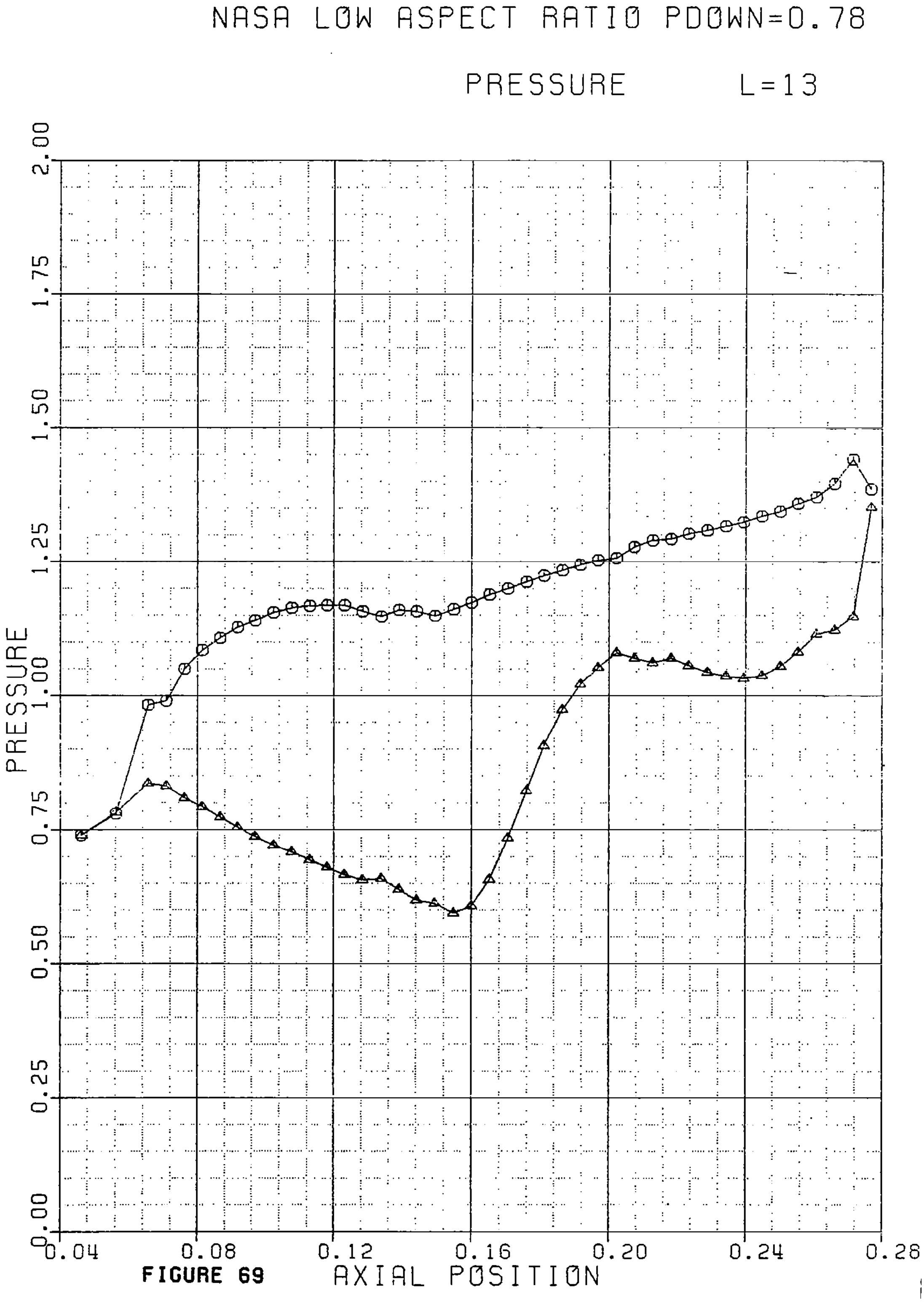
NASA LOW ASPECT RATIO PDOWN=0.78
PRESSURE L=13
PRESSURE
0.00
0.25
0.50
0.75
1.00
1.25
1.50
1.75
2.00
0.04
0.08
0.12
0.16
0.20
0.24
0.28
AXIAL POSITION

FIGURE 69

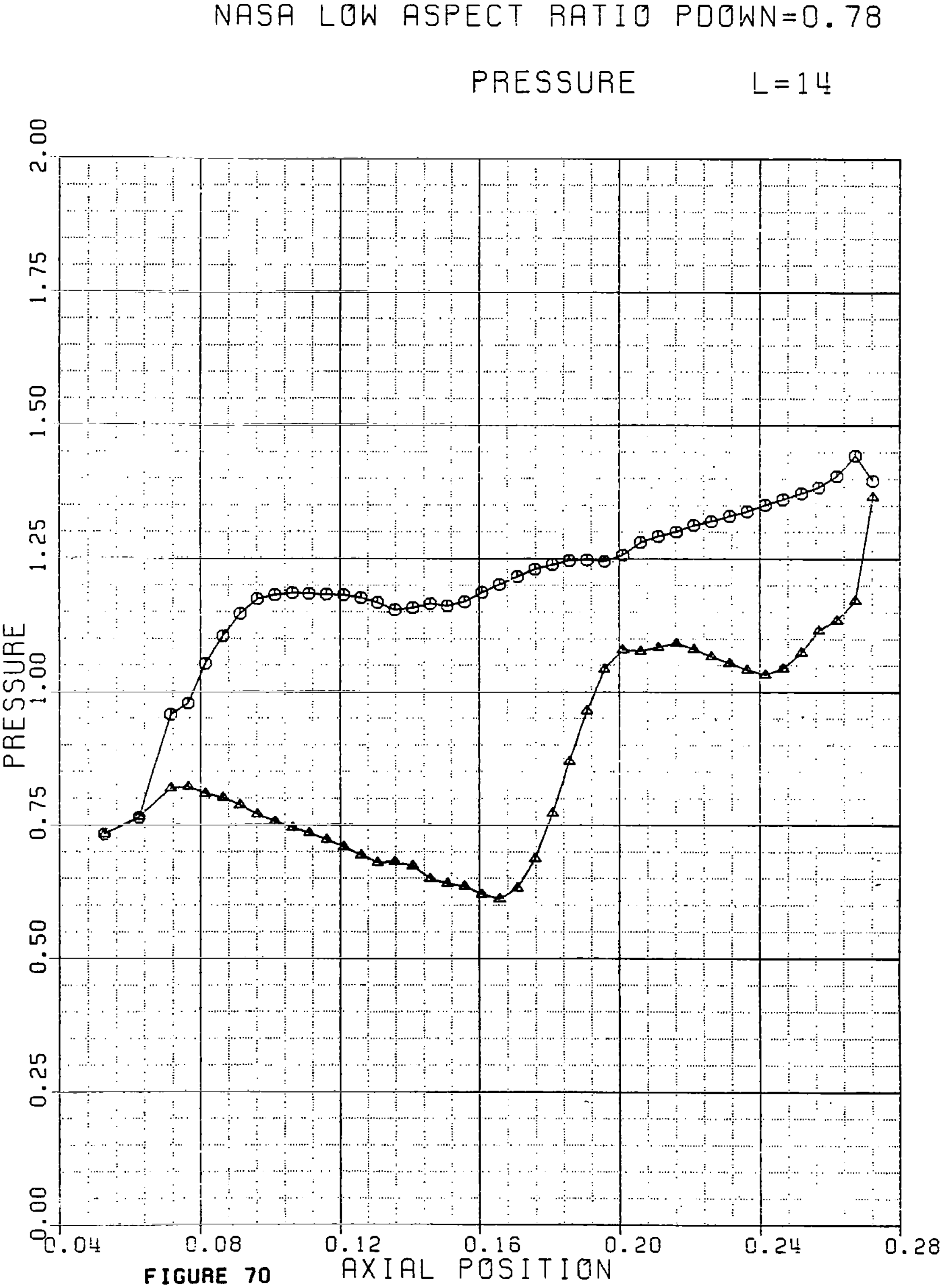
NASA LOW ASPECT RATIO PDOWN=0.78
PRESSURE L=14
PRESSURE
0.00
0.25
0.50
0.75
1.00
1.25
1.50
1.75
2.00
0.04
0.08
0.12
0.16
0.20
0.24
0.28
AXIAL POSITION

FIGURE 70

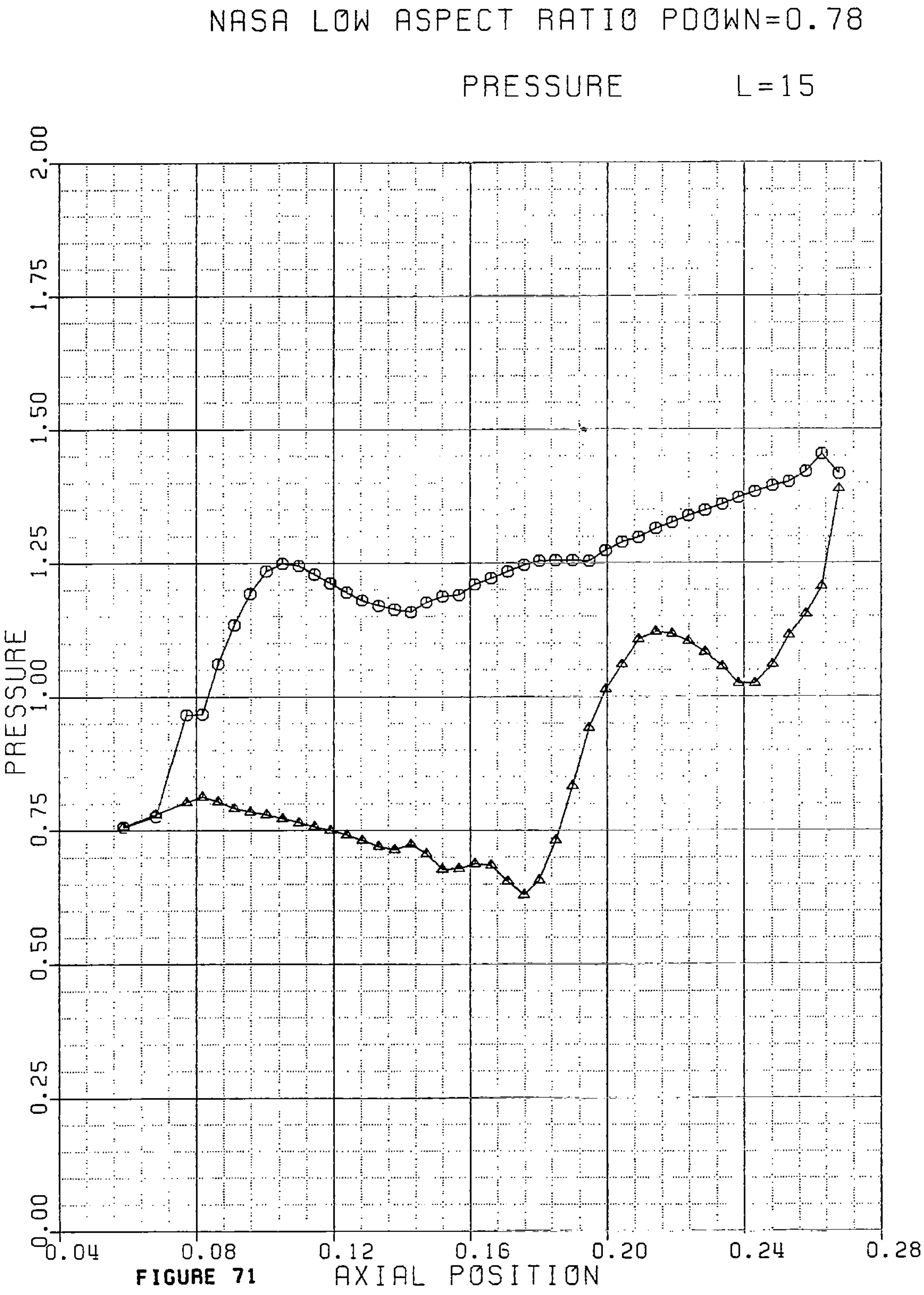
NASA LOW ASPECT RATIO PDOWN=0.78
PRESSURE L=15
PRESSURE
2.00
1.75
1.50
1.25
1.00
0.75
0.50
0.25
0.00
0.04
0.08
0.12
0.16
0.20
0.24
0.28
AXIAL POSITION

FIGURE 71

NASA LOW ASPECT RATIO PDOWN=0.78

PRESSURE L=16

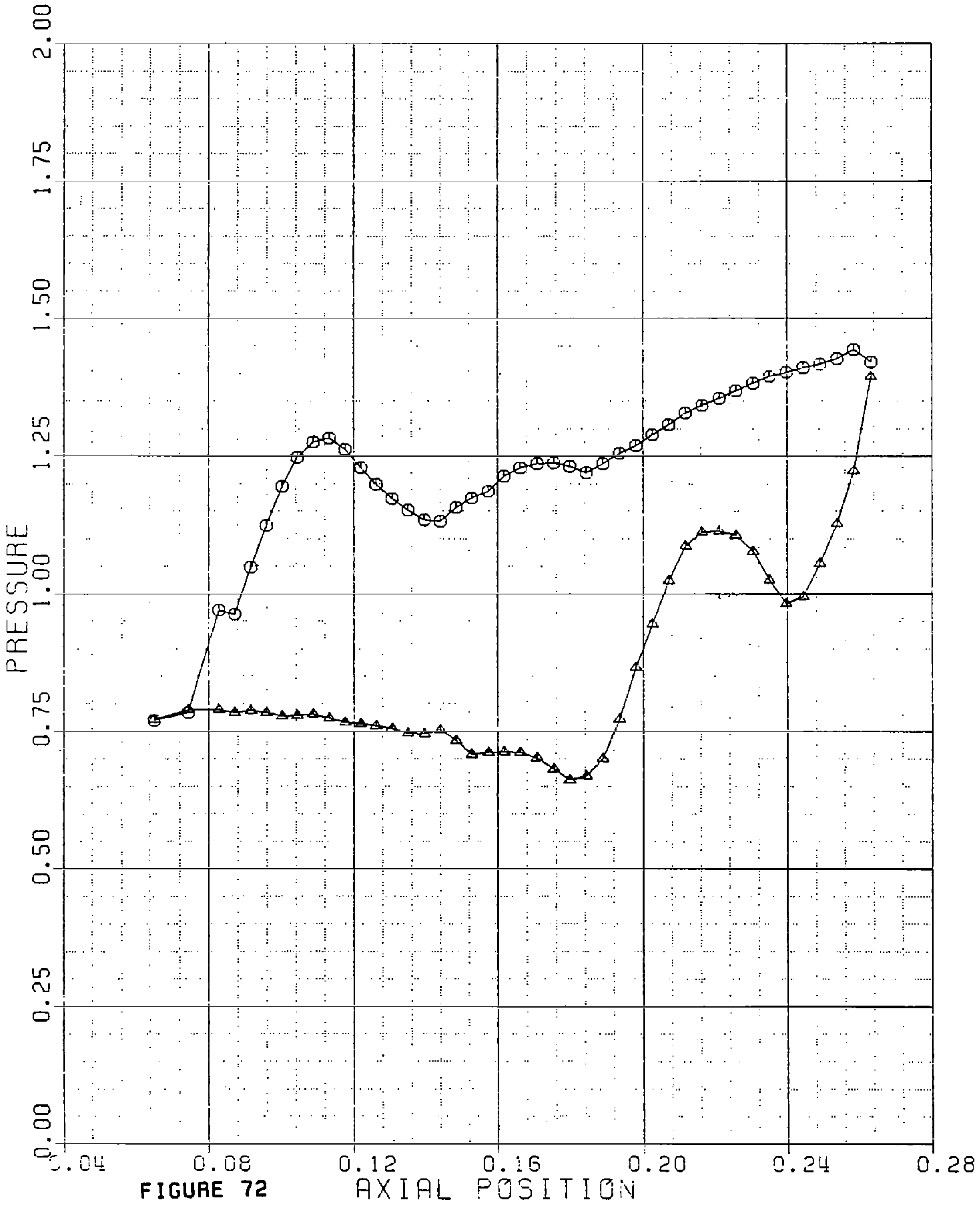

FIGURE 72

NASA LOW ASPECT RATIO PDOWN=0.78

PRESSURE L=17

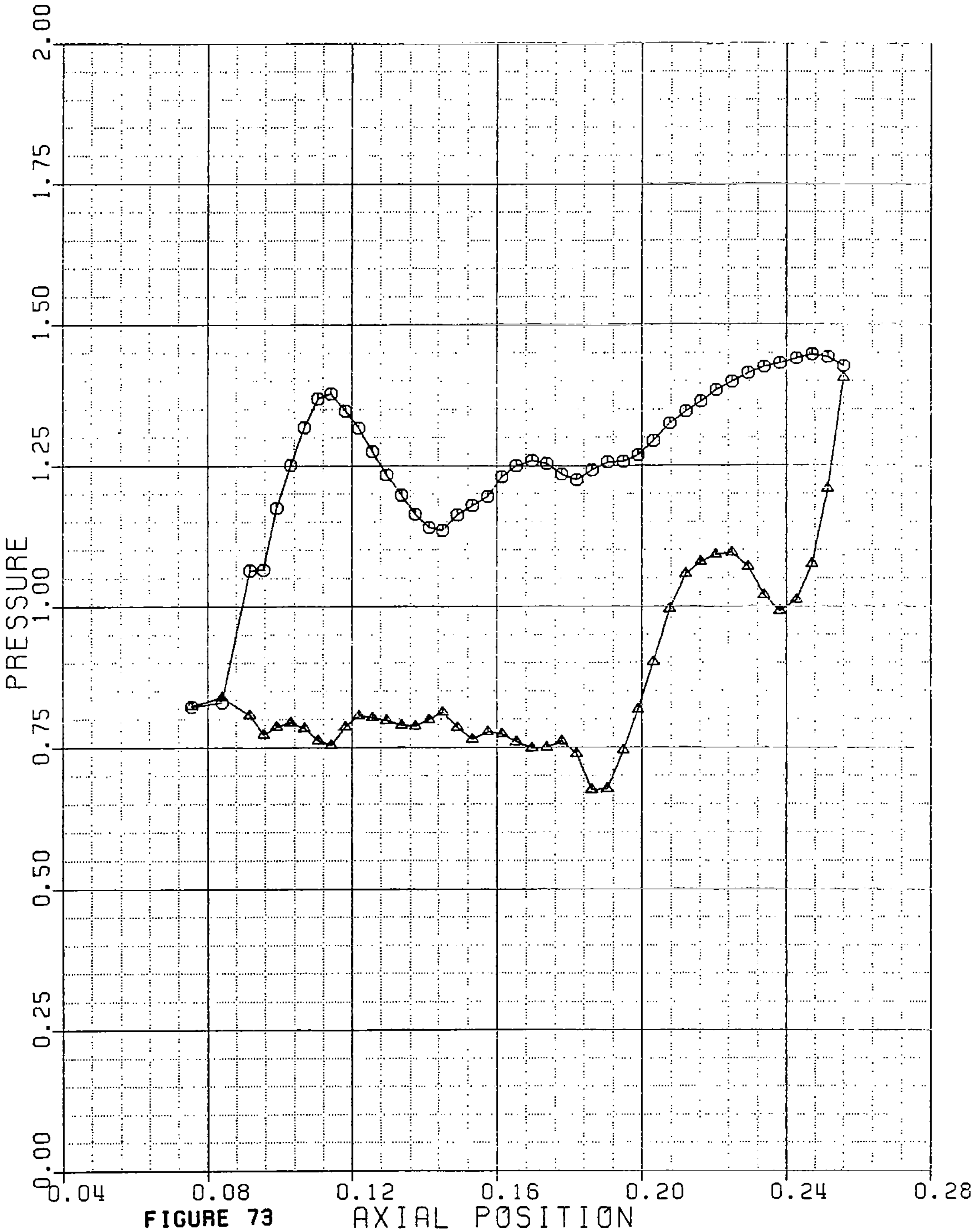

FIGURE 73 AXIAL POSITION

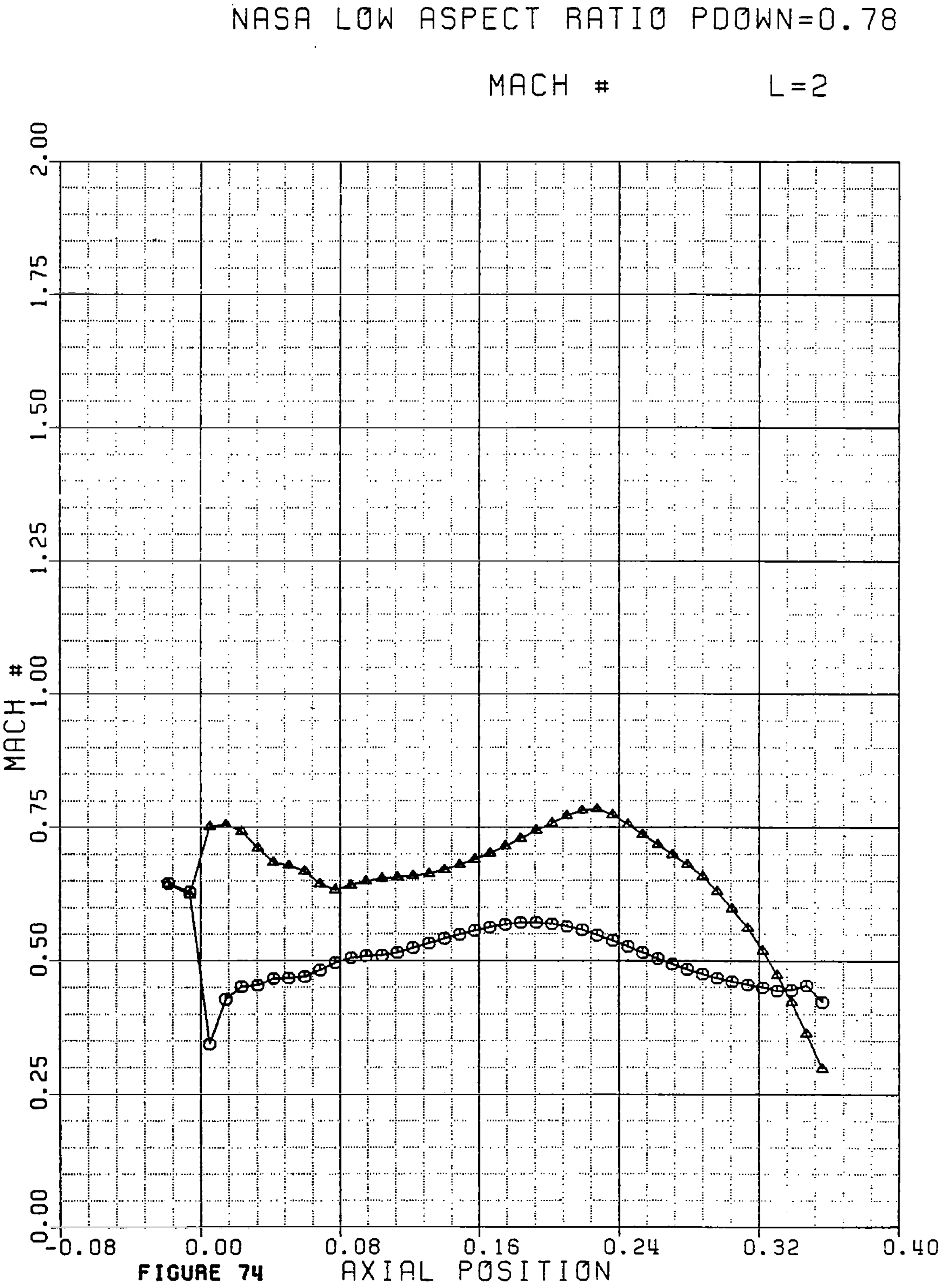
NASA LOW ASPECT RATIO PDOWN=0.78
MACH #
L=2
MACH #
2.00
1.75
1.50
1.25
1.00
0.75
0.50
0.25
0.00
-0.08
0.00
0.08
0.16
0.24
0.32
0.40
AXIAL POSITION

FIGURE 74

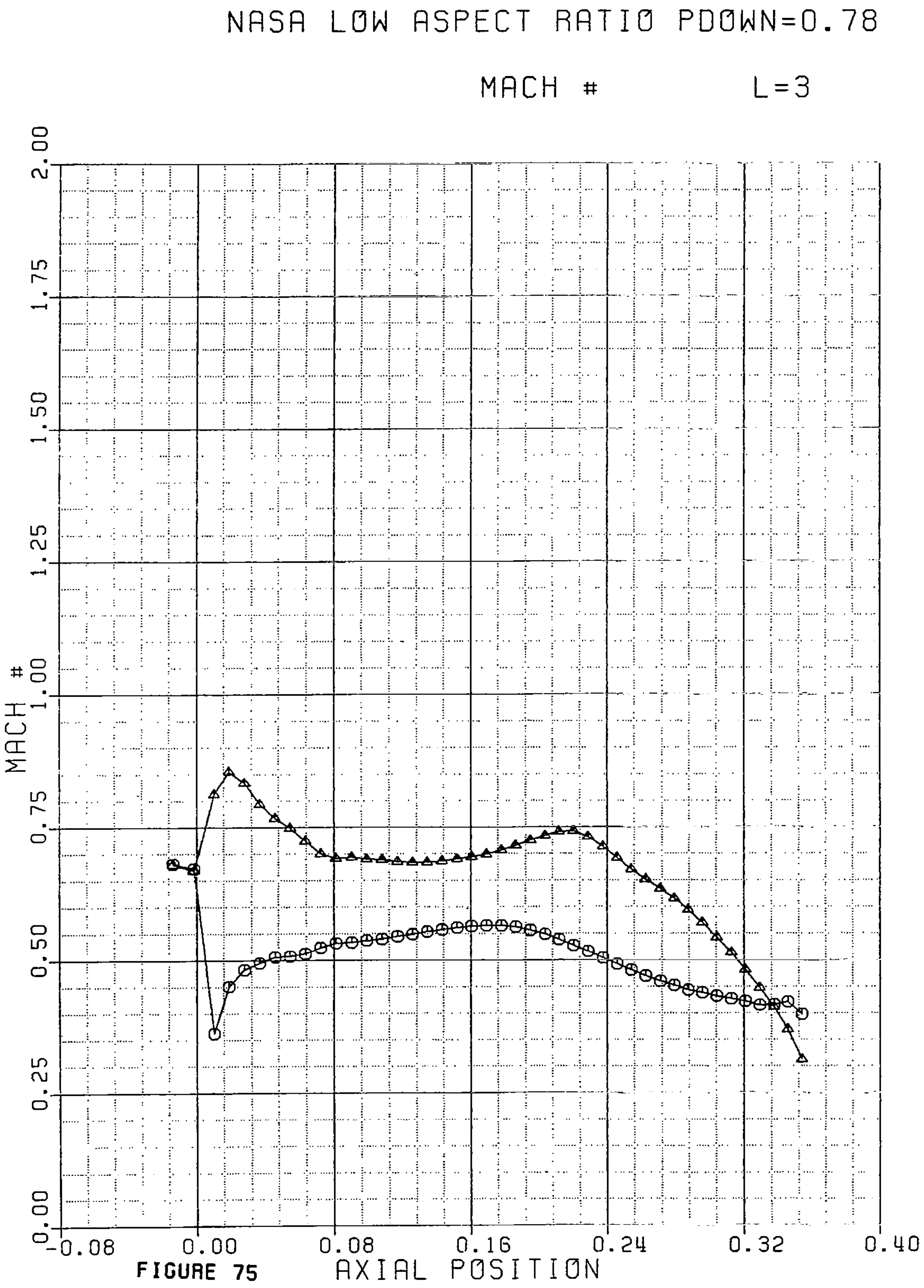
NASA LOW ASPECT RATIO PDOWN=0.78
MACH # L=3
MACH #
2.00
1.75
1.50
1.25
1.00
0.75
0.50
0.25
0.00
-0.08
0.00
0.08
0.16
0.24
0.32
0.40
AXIAL POSITION

FIGURE 75

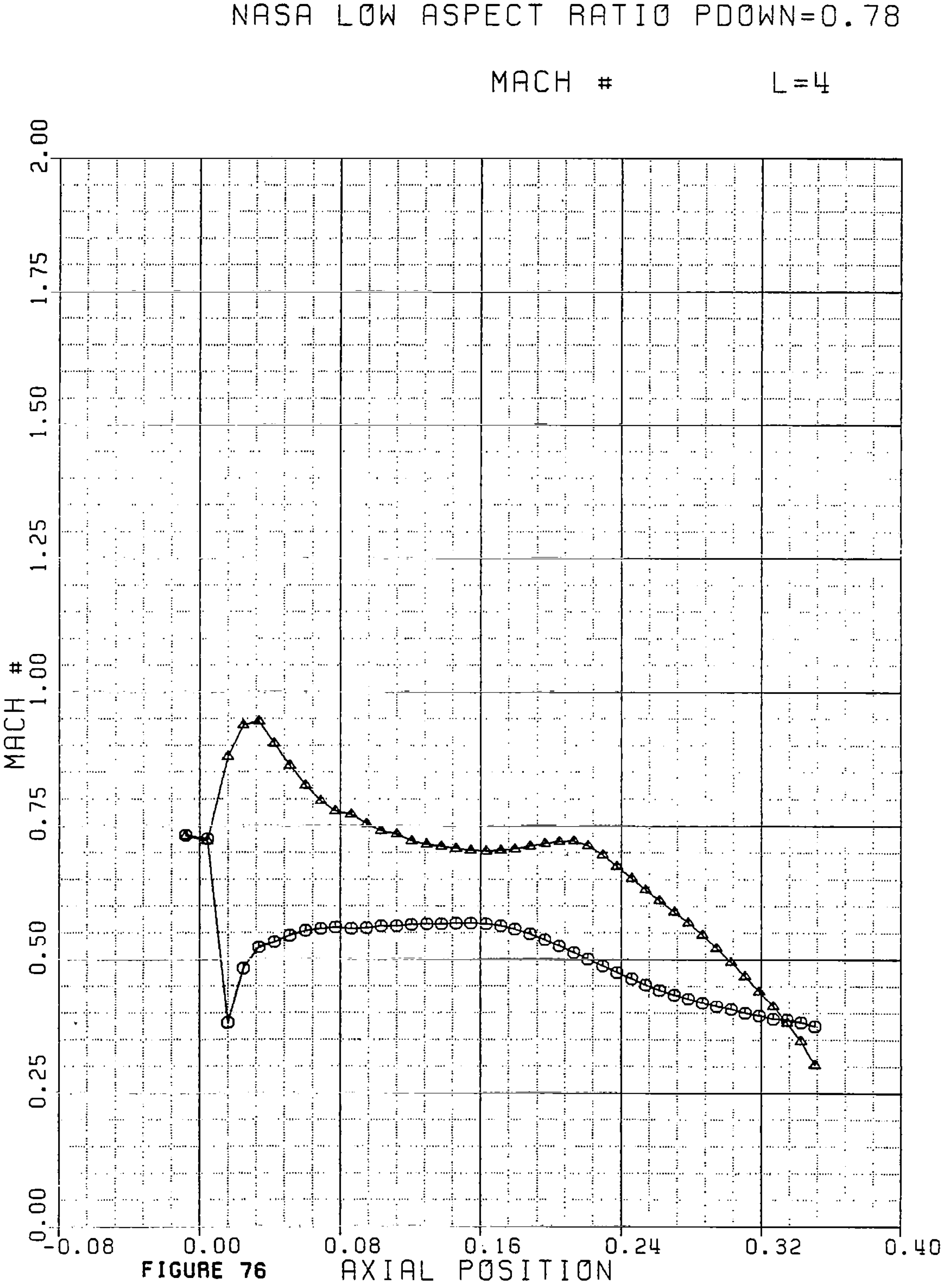
NASA LOW ASPECT RATIO PDOWN=0.78
MACH #
L=4
MACH #
2.00
1.75
1.50
1.25
1.00
0.75
0.50
0.25
0.00
-0.08
0.00
0.08
0.16
0.24
0.32
0.40
AXIAL POSITION

FIGURE 76

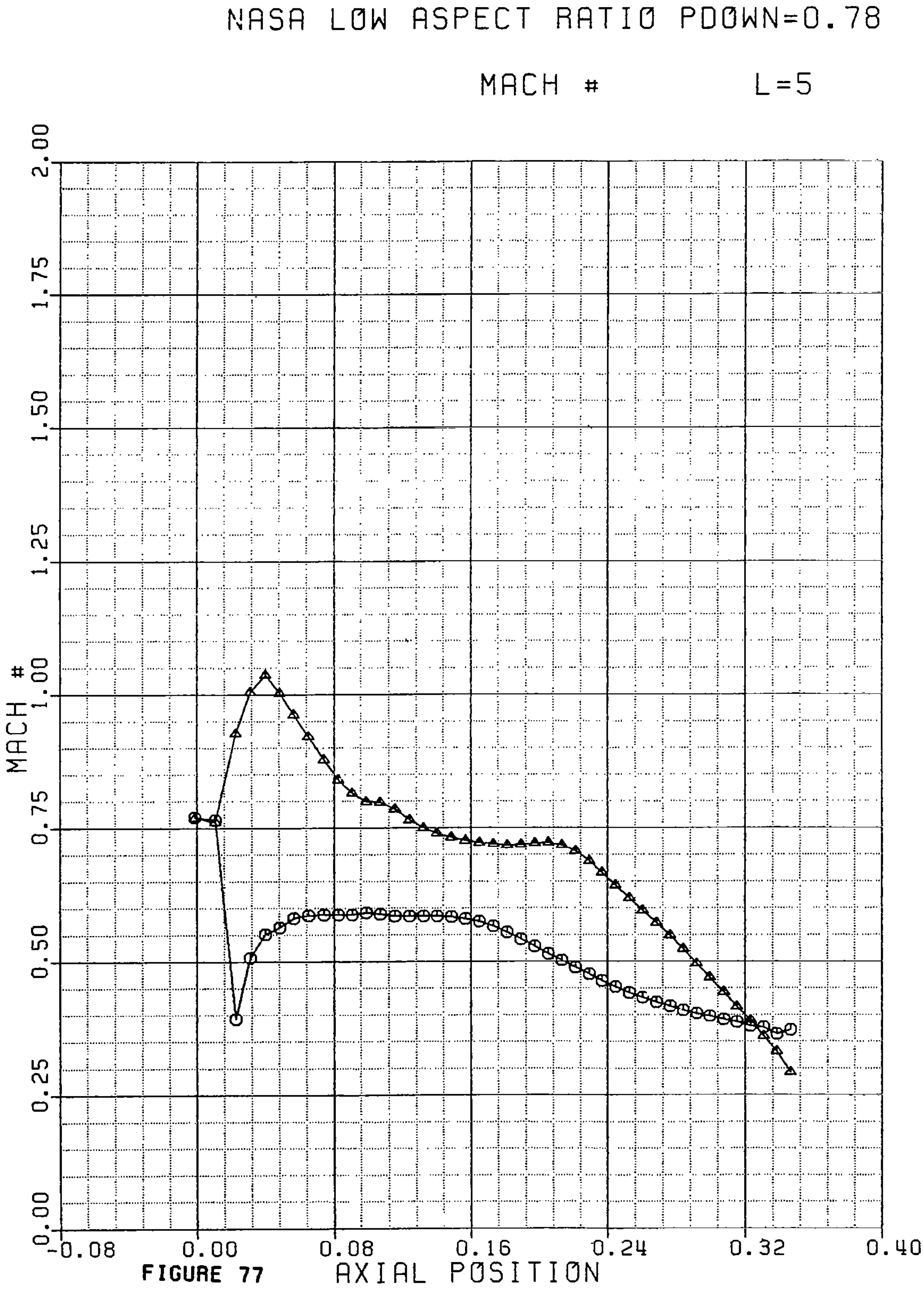
NASA LOW ASPECT RATIO PDOWN=0.78
MACH #
L=5
MACH #
0.00
0.25
0.50
0.75
1.00
1.25
1.50
1.75
2.00
-0.08
0.00
0.08
0.16
0.24
0.32
0.40
AXIAL POSITION

FIGURE 77

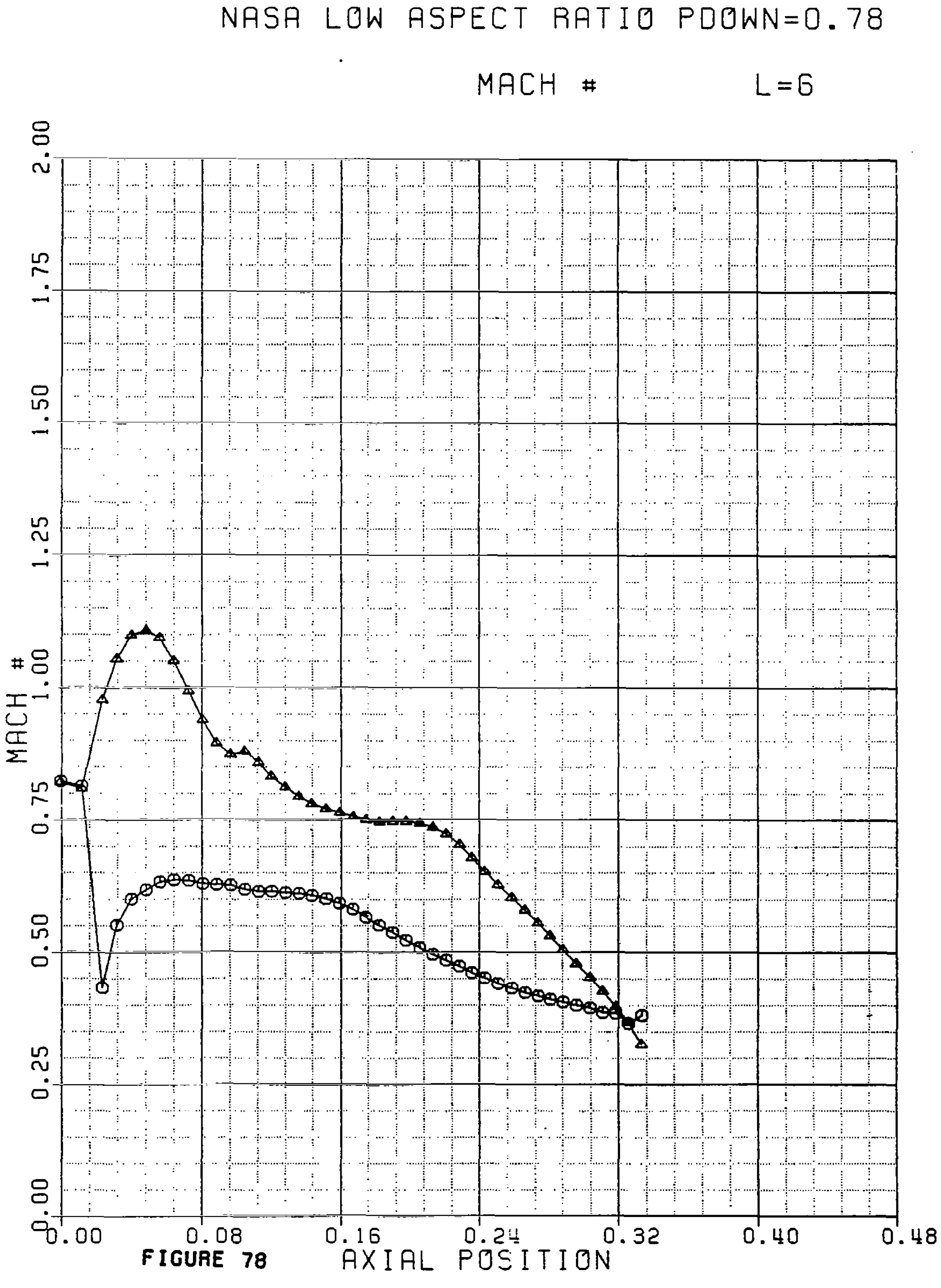
NASA LOW ASPECT RATIO PDOWN=0.78
MACH #
L=6
MACH #
2.00
1.75
1.50
1.25
1.00
0.75
0.50
0.25
0.00
0.00
0.08
0.16
0.24
0.32
0.40
0.48
AXIAL POSITION

FIGURE 78

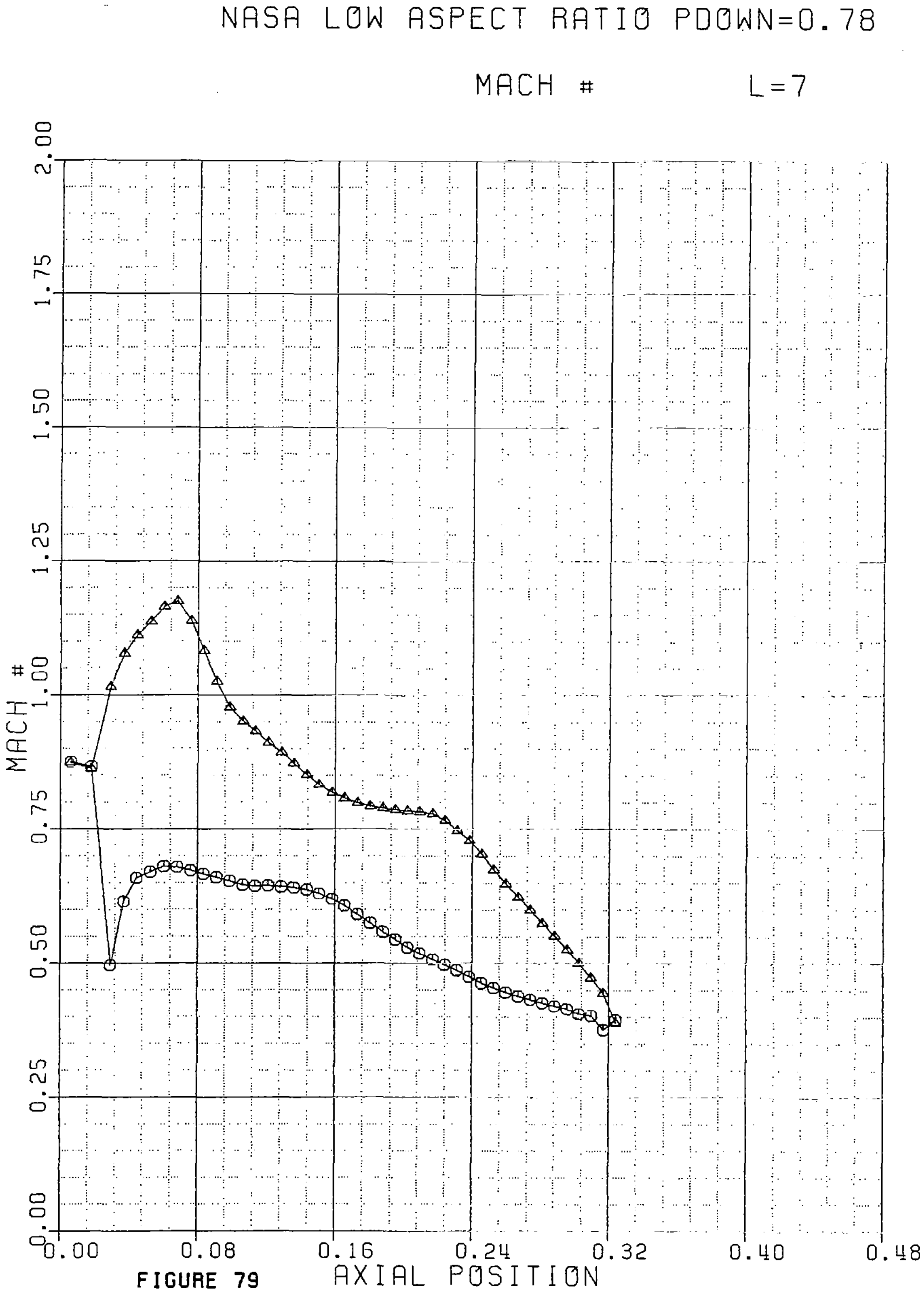
NASA LOW ASPECT RATIO PDOWN=0.78
MACH #
L=7
MACH #
0.00
0.25
0.50
0.75
1.00
1.25
1.50
1.75
2.00
0.00
0.08
0.16
0.24
0.32
0.40
0.48
AXIAL POSITION

FIGURE 79

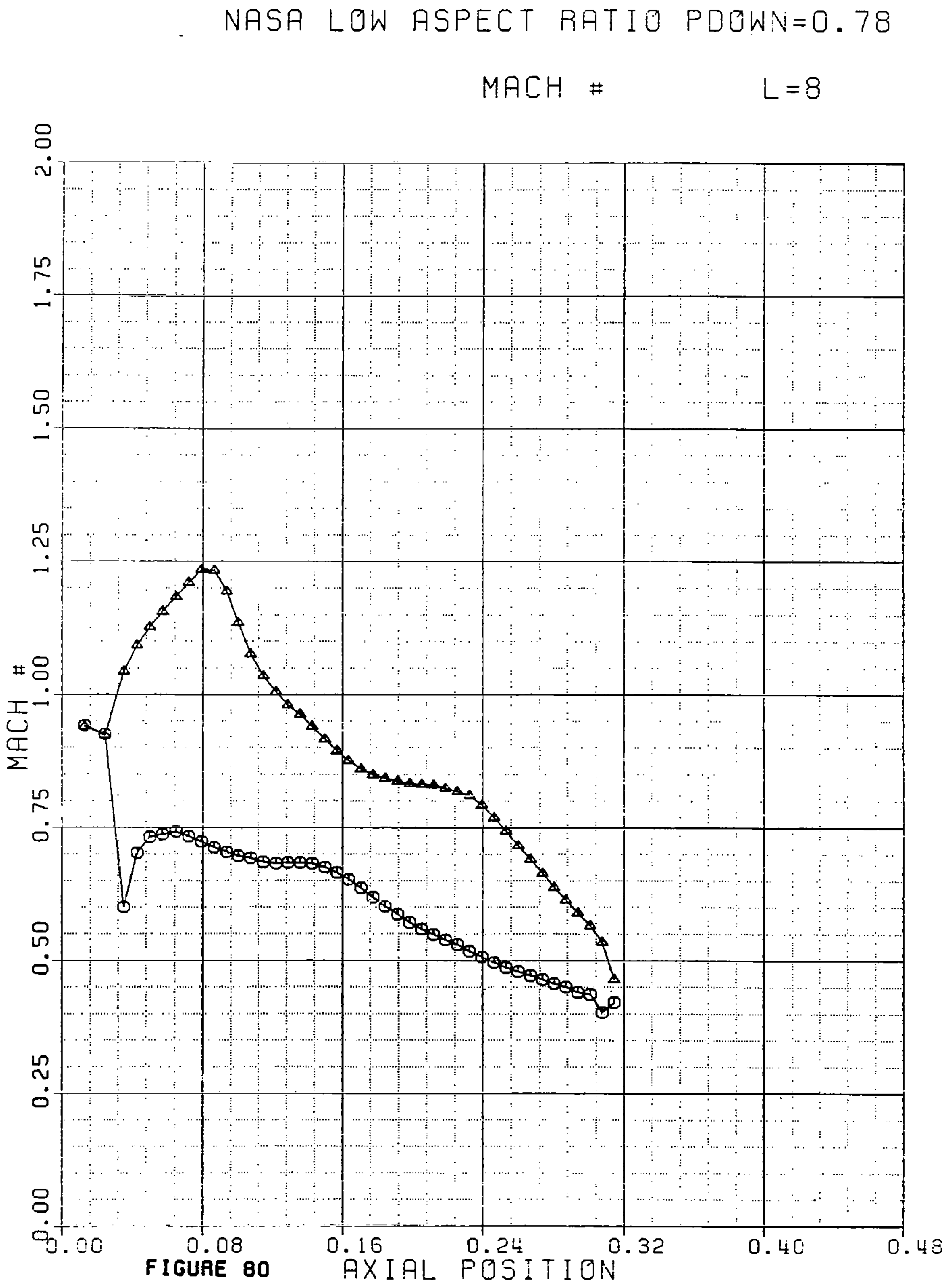
NASA LOW ASPECT RATIO PDOWN=0.78
MACH #
L=8
MACH #
0.00
0.25
0.50
0.75
1.00
1.25
1.50
1.75
2.00
0.00
0.08
0.16
0.24
0.32
0.40
0.48
AXIAL POSITION

FIGURE 80

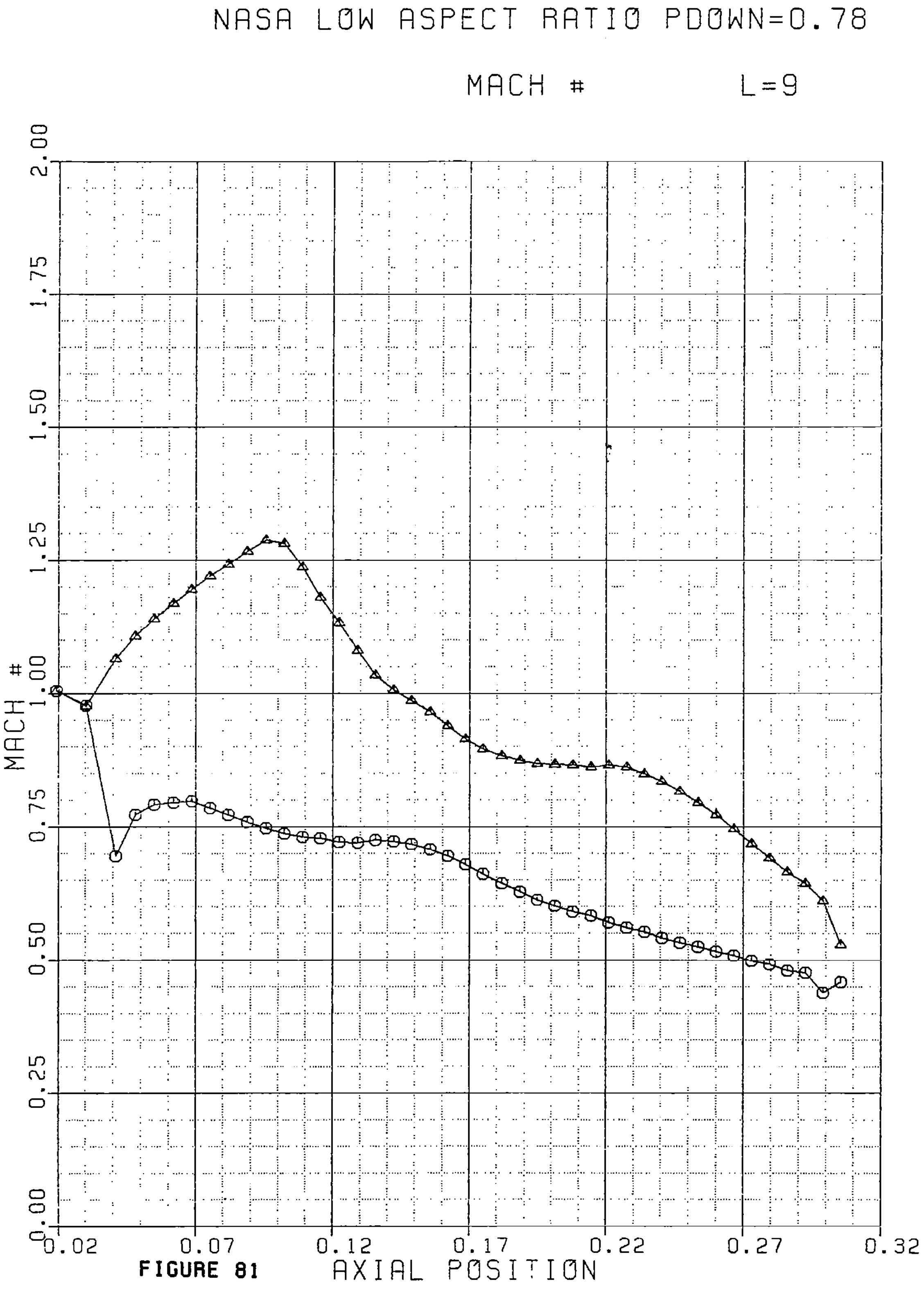
NASA LOW ASPECT RATIO PDOWN=0.78
MACH # L=9
MACH #
0.00
0.25
0.50
0.75
1.00
1.25
1.50
1.75
2.00
0.02
0.07
0.12
0.17
0.22
0.27
0.32
AXIAL POSITION

FIGURE 81

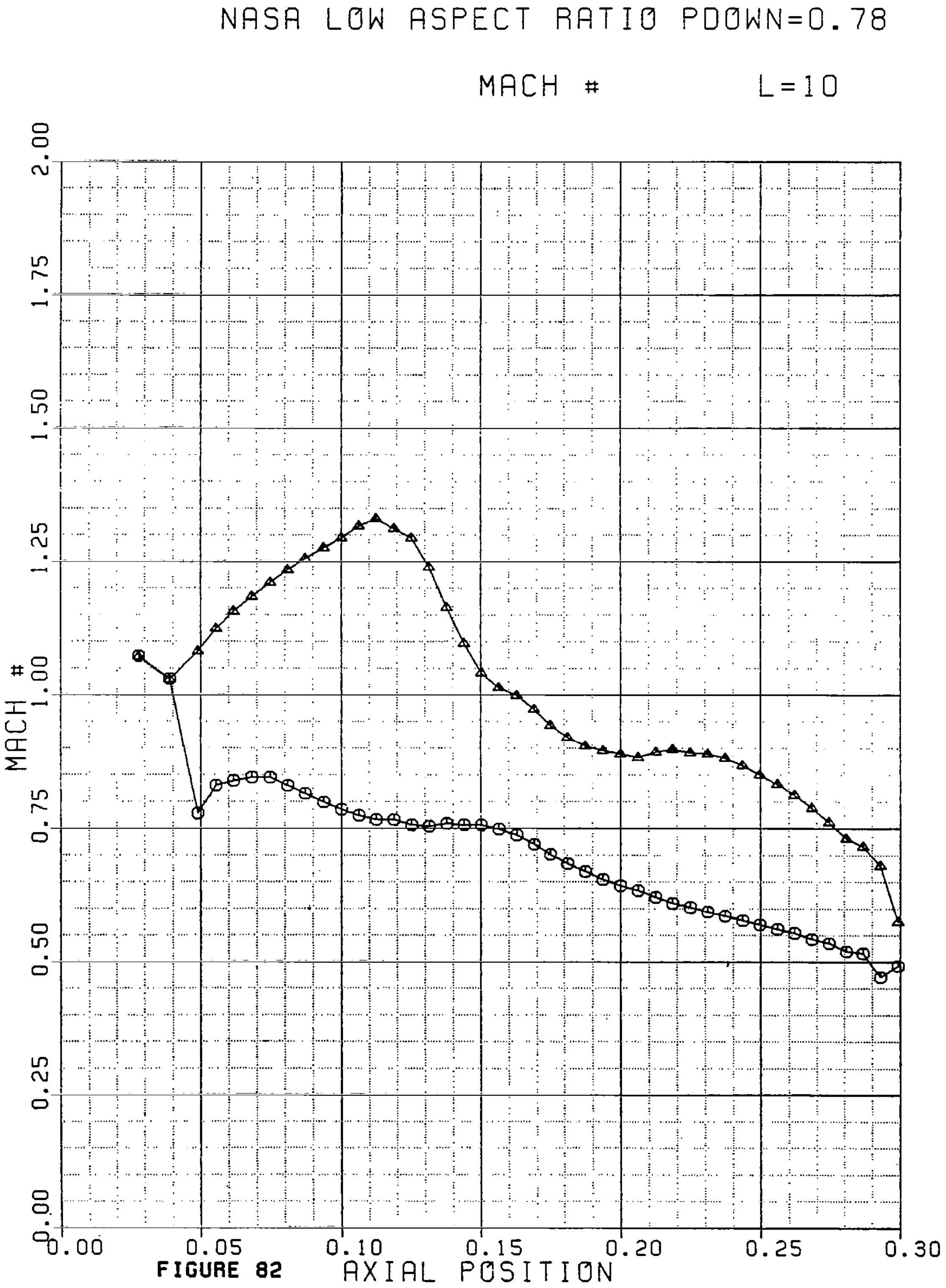
NASA LOW ASPECT RATIO PDOWN=0.78
MACH #
L=10
MACH #
0.00
0.25
0.50
0.75
1.00
1.25
1.50
1.75
2.00
0.00
0.05
0.10
0.15
0.20
0.25
0.30
AXIAL POSITION

FIGURE 82

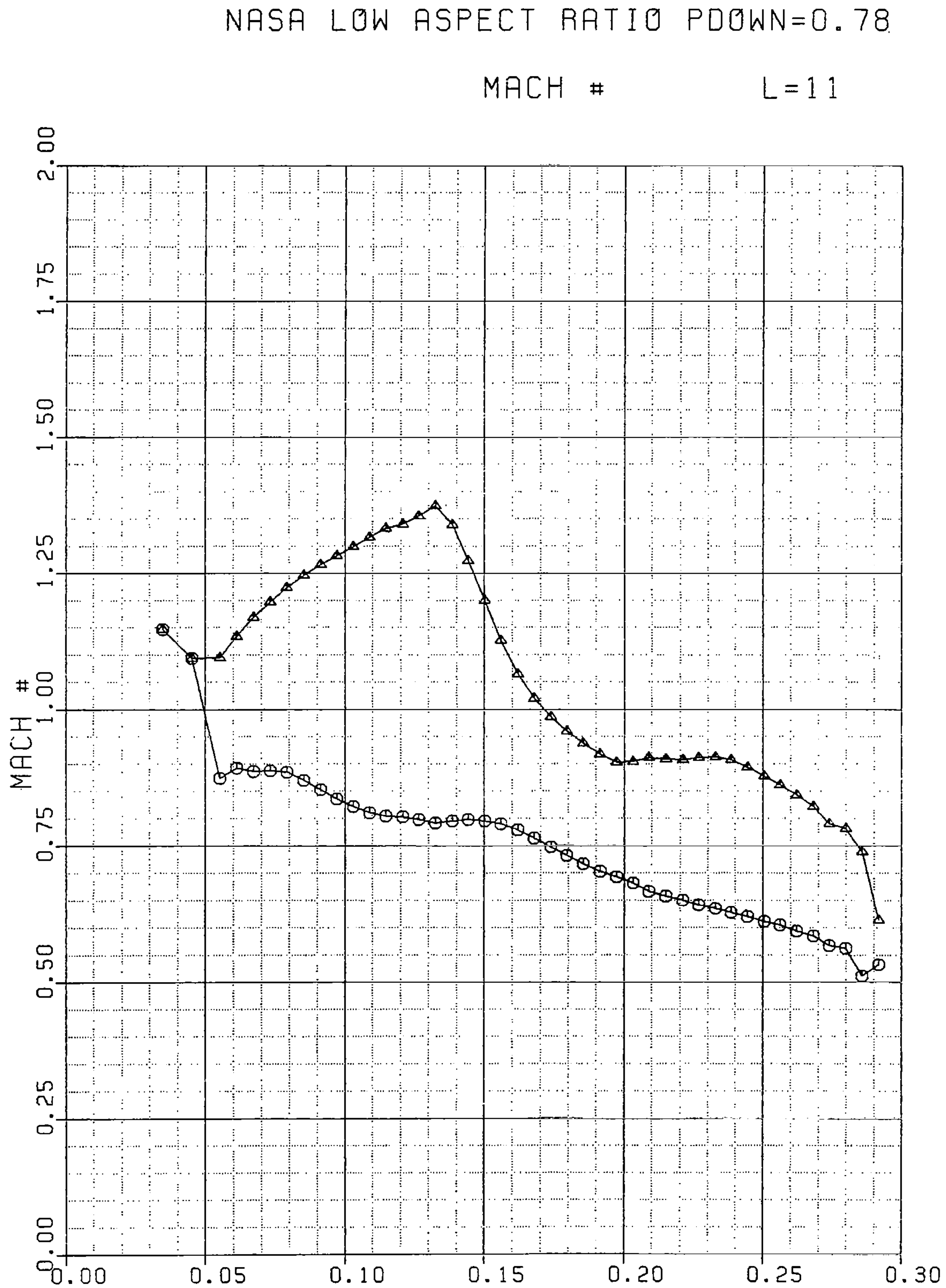
NASA LOW ASPECT RATIO PDOWN=0.78
MACH # L=11
MACH #
0.00
0.25
0.50
0.75
1.00
1.25
1.50
1.75
2.00
0.00
0.05
0.10
0.15
0.20
0.25
0.30
AXIAL POSITION

FIGURE 83

NASA LOW ASPECT RATIO PDOWN=0.78

MACH #   L=12

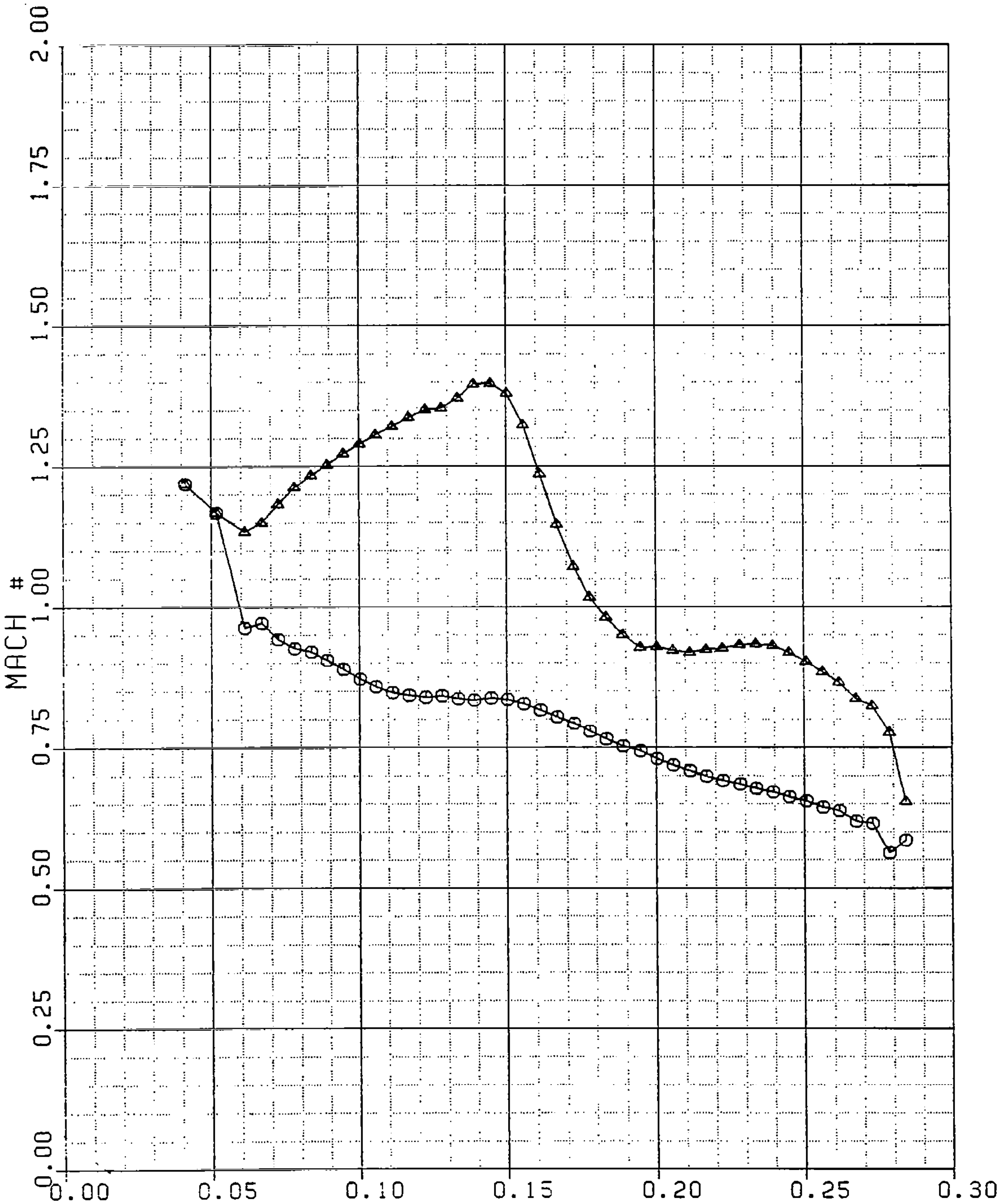

FIGURE 84 AXIAL POSITION

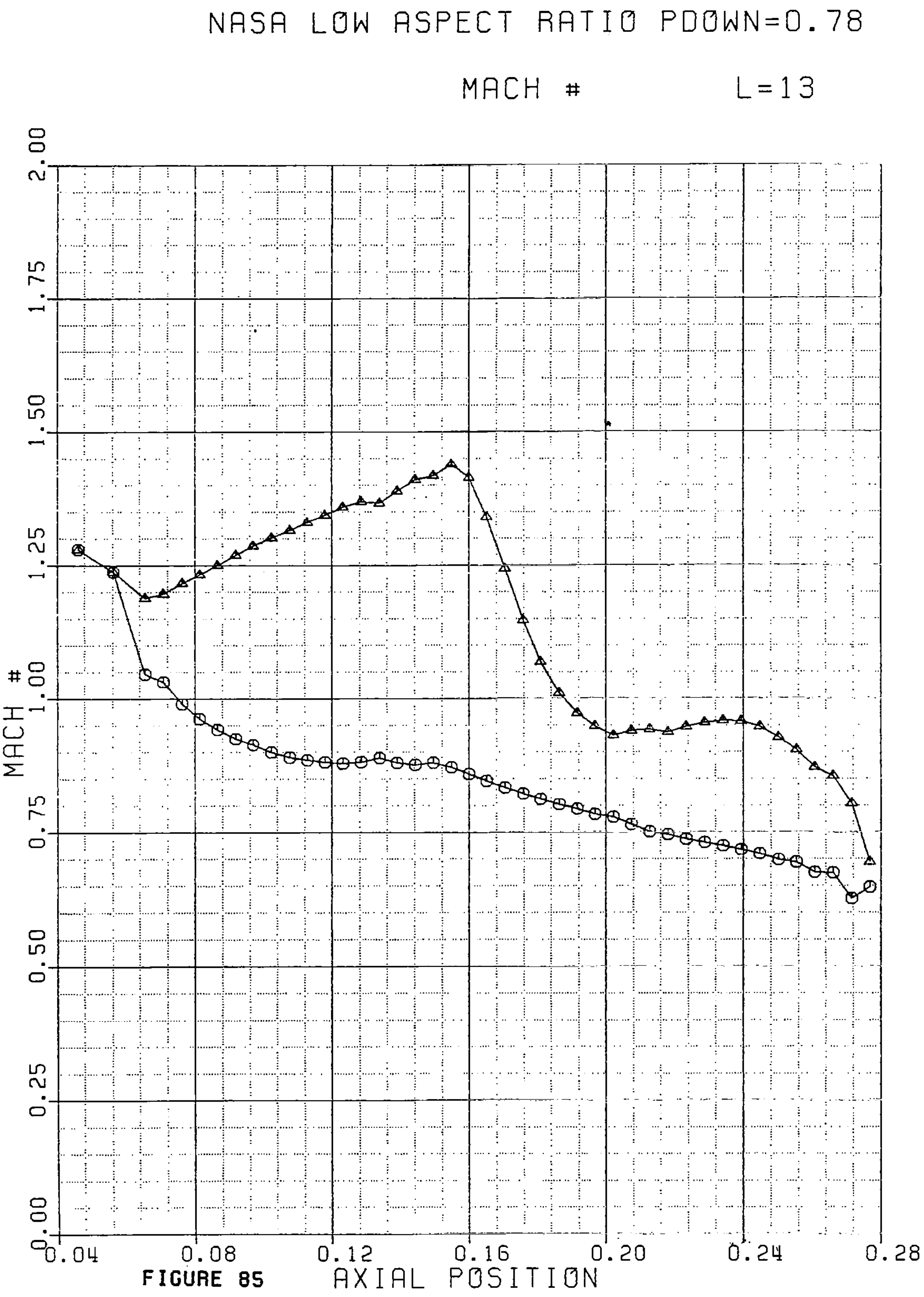
NASA LOW ASPECT RATIO PDOWN=0.78
MACH # L=13
MACH #
AXIAL POSITION
2.00
1.75
1.50
1.25
1.00
0.75
0.50
0.25
0.00
0.04
0.08
0.12
0.16
0.20
0.24
0.28

FIGURE 85

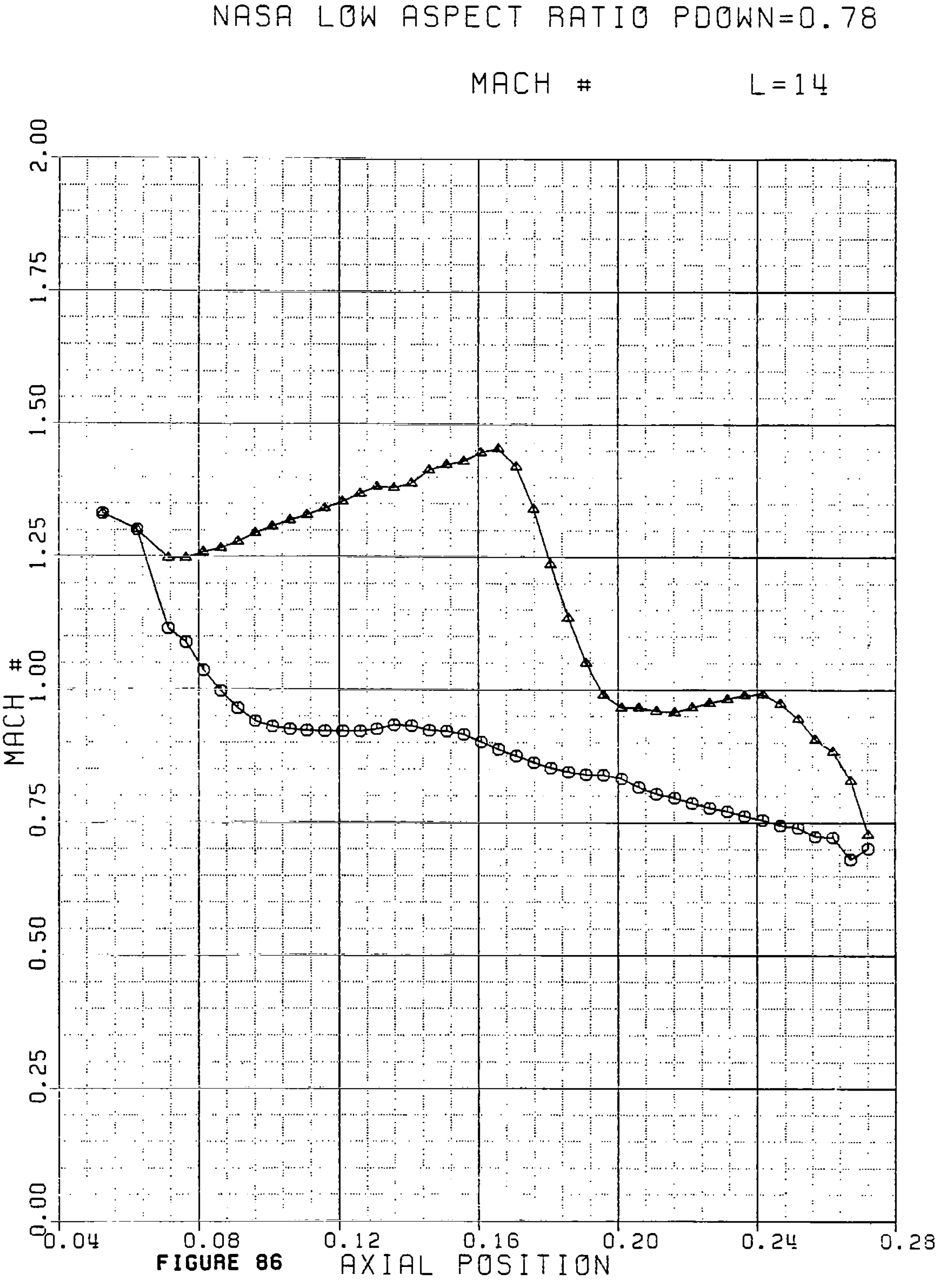
NASA LOW ASPECT RATIO PDOWN=0.78
MACH #
L=14
MACH #
0.00
0.25
0.50
0.75
1.00
1.25
1.50
1.75
2.00
0.04
0.08
0.12
0.16
0.20
0.24
0.28
AXIAL POSITION

FIGURE 86

NASA LOW ASPECT RATIO PDOWN=0.78

MACH #   L=15

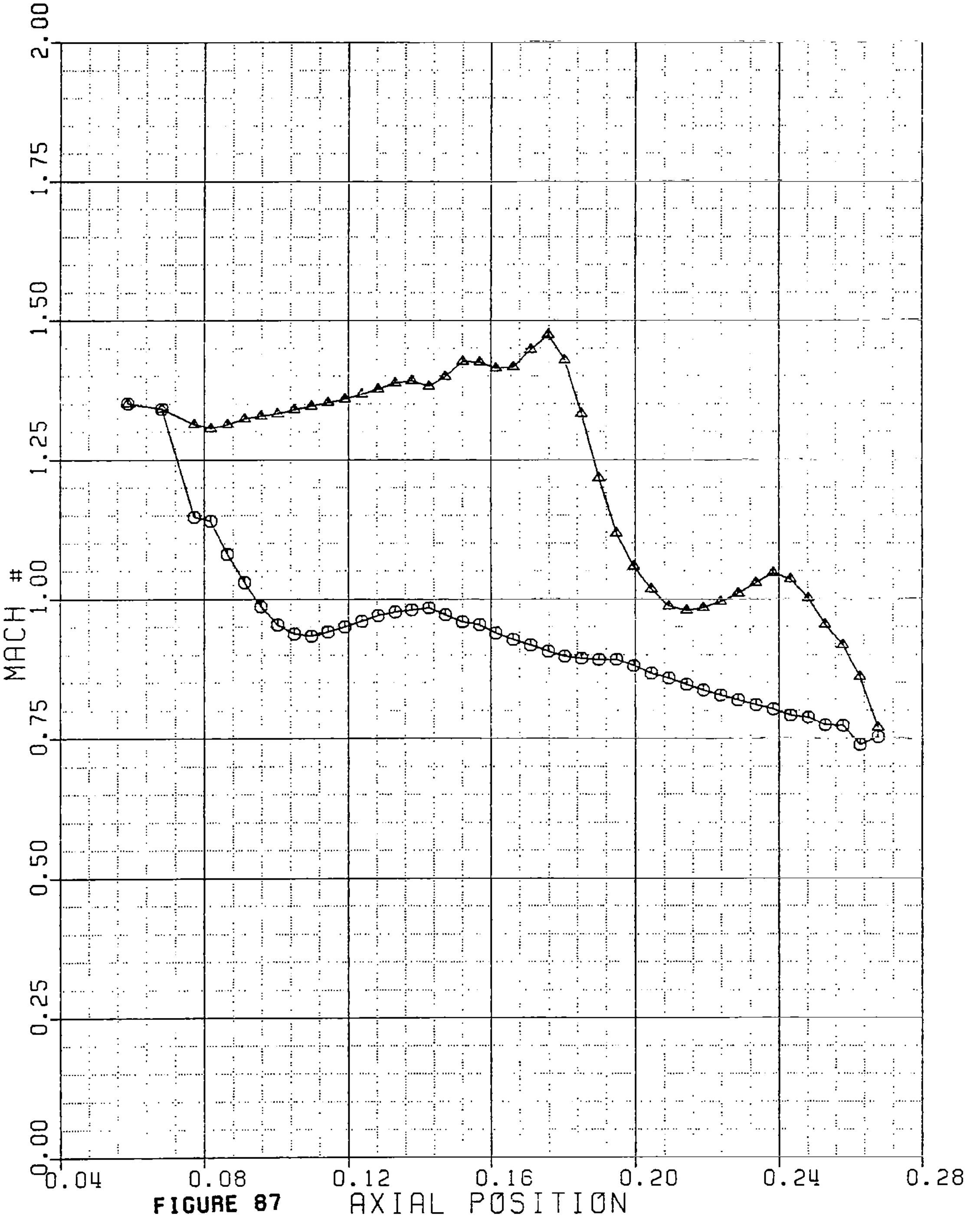

FIGURE 87

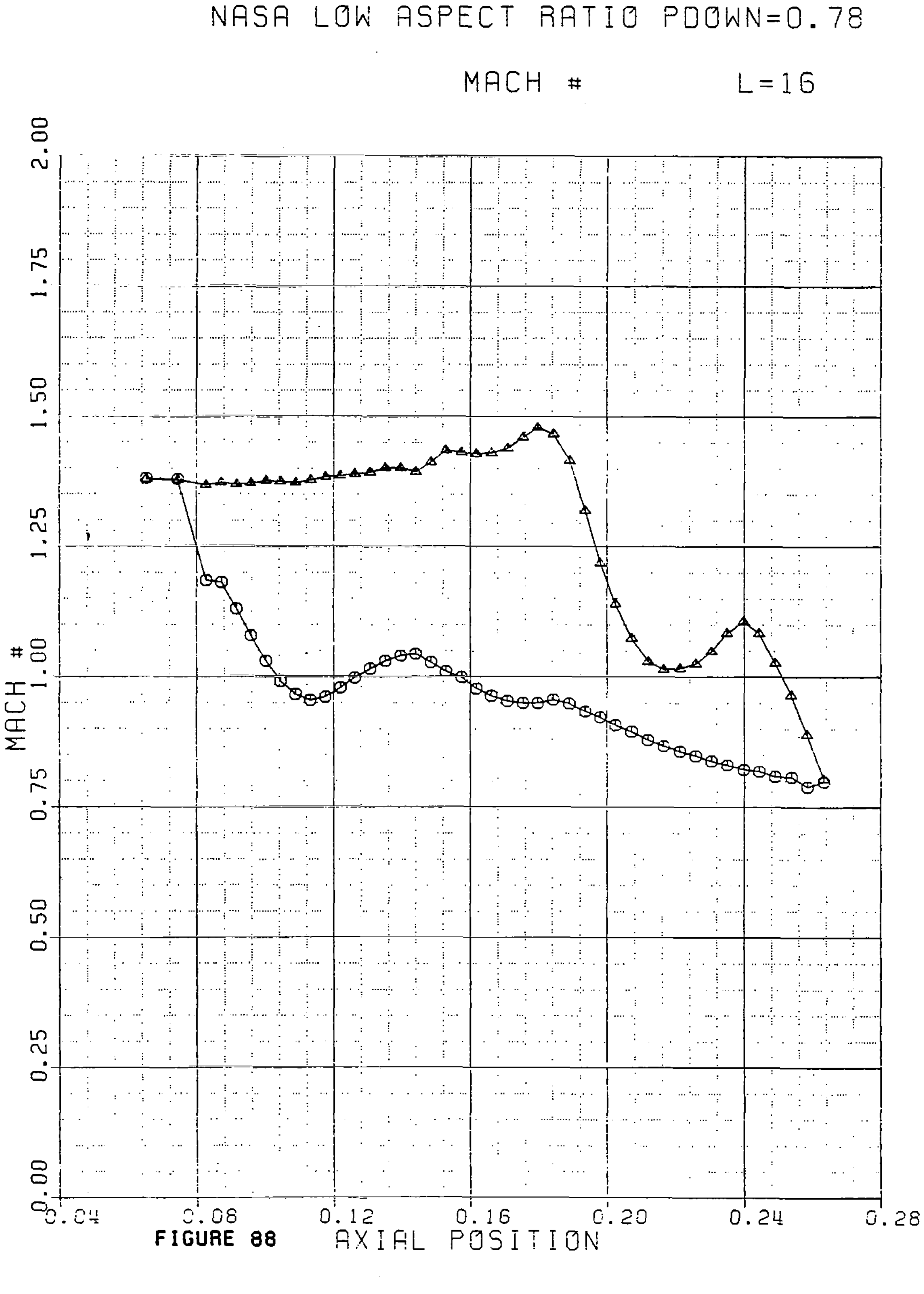
NASA LOW ASPECT RATIO PDOWN=0.78
MACH #
L=16
MACH #
2.00
1.75
1.50
1.25
1.00
0.75
0.50
0.25
0.00
0.04
0.08
0.12
0.16
0.20
0.24
0.28
AXIAL POSITION

FIGURE 88


NASA LOW ASPECT RATIO PDOWN=0.78
MACH # L=17
MACH #
2.00
1.75
1.50
1.25
1.00
0.75
0.50
0.25
0.00
0.04
0.08
0.12
0.16
0.20
0.24
0.28
AXIAL POSITION

FIGURE 89

1. Report No.
NASA CR-3560

2. Government Accession No.

3. Recipient's Catalog No.

4. Title and Subtitle
A FORTRAN PROGRAM FOR CALCULATING THREE-DIMENSIONAL, INVISCID, ROTATIONAL FLOWS WITH SHOCK WAVES IN AXIAL COMPRESSOR BLADE ROWS - USER'S MANUAL

5. Report Date
June 1982

6. Performing Organization Code

7. Author(s)
William T. Thompkins, Jr.

8. Performing Organization Report No.
GT & PDL Report No. 162

10. Work Unit No.

9. Performing Organization Name and Address
Massachusetts Institute of Technology
Gas Turbine and Plasma Dynamics Laboratory
Cambridge, Massachusetts

11. Contract or Grant No.
NSG-3234

13. Type of Report and Period Covered
Contractor Report

12. Sponsoring Agency Name and Address
National Aeronautics and Space Administration
Washington, D.C. 20546

14. Sponsoring Agency Code
505-32-52

15. Supplementary Notes
Final report. Project Managers, Rodrick Chima and William D. McNally, Fluid Mechanics and Acoustics Division, NASA Lewis Research Center, Cleveland, Ohio 44135.

16. Abstract

A FORTRAN-IV computer program has been developed for the calculation of the inviscid transonic/supersonic flow field in a fully three-dimensional blade passage of an axial compressor rotor or stator. Rotors may have dampers (part-span shrouds). MacCormack's explicit time-marching method is used to solve the unsteady Euler equations on a finite difference mesh. This technique captures shocks and smears them over several grid points. Input quantities are blade row geometry, operating conditions and thermodynamic quantities. Output quantities are three velocity components, density and internal energy at each mesh point. Other flow quantities are calculated from these variables. A short graphics package is included with the code, and may be used to display the finite difference grid, blade geometry and static pressure contour plots on blade-to-blade calculation surfaces or blade suction and pressure surfaces. The flow in a low aspect ratio transonic compressor has been analyzed and compared with high response total pressure probe measurements and gas fluorescence static density measurements made in the MIT blowdown wind tunnel. These comparisons show that the computed flow fields accurately model the measured shock wave locations and overall aerodynamic performance.

17. Key Words (Suggested by Author(s))
Turbomachinery; Compressors; Three-dimensional flow; Inviscid flow; Rotational flow; Compressible flow; Euler equations; Computer programs

18. Distribution Statement
Unclassified - unlimited
STAR Category 02

19. Security Classif. (of this report)	20. Security Classif. (of this page)	21. No. of Pages	22. Price*
Unclassified	Unclassified	178	A09

* For sale by the National Technical Information Service, Springfield, Virginia 22161

NASA-Langley, 1982